Universität Bonn

Physikalisches Institut

Reconstruction of neutral pions in hadronic tau lepton decays in the ATLAS detector

Benedict Tobias Winter

An algorithm that reconstructs neutral pions in hadronic tau lepton decays in the ATLAS detector is presented. It subtracts energy deposited by charged hadrons in the electromagnetic calorimeter and identifies neutral pions in the remaining energy distribution. The information provided by the algorithm has a variety of applications in tau physics in ATLAS such as tau polarization studies, the identification of hadronically decaying taus or tau 4-momentum reconstruction.

Physikalisches Institut der
Universität Bonn
Nussallee 12
D-53115 Bonn

BONN-IB-2013-04
Dezember 2013

Universität Bonn

Physikalisches Institut

Reconstruction of neutral pions in hadronic tau lepton decays in the ATLAS detector

Benedict Tobias Winter

Dieser Forschungsbericht wurde als Masterarbeit von der Mathematisch-Naturwissenschaftlichen Fakultät der Universität Bonn angenommen.

Angenommen am:	14.09.2012
1. Gutachter:	Prof. Dr. Jochen Dingfelder
2. Gutachter:	Prof. Dr. Klaus Desch

Contents

Introduction

In 2010 physics data taking for physics analysis has started at the Large Hadron Collider (LHC). The operation of the LHC has been very successful and the amount of data delivered in the first years is far beyond expectation. The LHC enables the four experiments ALICE, ATLAS, CMS and LHCb to study proton-proton and heavy ion collisions in the energy range of several TeV, which has never been reached before in the laboratory. Thanks to the successful operation of the four experiments and the LHC the Standard Model has already now been tested in the new energy range with good precision. Recently a new particle has been observed in the search for the Standard Model Higgs boson, which has been searched for for more than 40 years. Other very interesting results are the observation of particle-antiparticle mixing in the D-meson system and the direct observation of the quark-gluon plasma. A large number of searches for new physics beyond the Standard Model have been performed. To this time no significant discrepancies from the Standard Model have been found, the LHC experiments are, however, still at the beginning of their physics programs. The center-of-mass energy of the proton-proton collisions will be increased to 13 TeV in 2015. The precision of the measurements will further improve with new reconstruction and analysis procedures and with the amount of data collected.

Tau leptons are of particular interest at the LHC. At hadron-hadron colliders analysis of channels with leptons in the final state have the general advantage that they can be more easily distinguished from the overwhelming production of hadronic jets. While the cleanest signatures come from muons or electrons, searches involving taus in the final state can be more sensitive to new particles that couple preferentially to heavy particles, like the Higgs boson. The search for decays of the recently observed particle into two taus ($H \rightarrow \tau\tau$) will be an important test of its couplings to elementary fermions and therefore the compatibility with the Standard Model Higgs boson. Another advantage of taus for physics analysis is that taus are the only leptons whose polarization can be measured at the LHC.

Taus are reconstructed from their decay products, since they decay most of the time already in the beam pipe. Sixty-five percent of all taus decay into hadrons. In most cases these are one, two or three pions, hereby decays into more than one pion mostly happen via intermediate resonances. The reconstruction of the neutral pions in hadronic tau lepton decays is of increasing importance for tau physics in ATLAS. Information on the reconstructed charged decay products is already used to improve the resolution of the 4-momentum of the visible decay products and for tau identification. Both areas could additionally benefit from using information on neutral pions. Physics studies make increasing use of tau polarization. Predicting the number of neutral pions is hereby of particular importance, the same applies for the reconstruction of the individual neutral pion 4-momenta and of the intermediate resonances.

In this thesis an algorithm is proposed that reconstructs the neutral pion substructure of hadronically decaying taus in the ATLAS detector. It is based on the idea to subtract the energy deposited by charged hadrons in the electromagnetic calorimeter and to identify neutral pions in the remaining energy distribution. One of the main advantages of this approach is that neutral pions can be reconstructed whose subshowers are overlapping or merged with charged particle's subshowers. This frequently happens in tau decays at high momenta, as the momentum exchange in the decay is small compared to the boost. The development of the algorithm is documented in this thesis and detailed studies of its performance in Monte Carlo simulation are presented.

The structure of the thesis is as follows:

- In chapter 1 the theoretical background for the study is provided. The Standard Model of particle physics is introduced. A detailed section focuses on the properties of the tau lepton.
- The second chapter contains an introduction of the LHC and the ATLAS detector. The tracking system and especially the calorimeter system are described in more detail, as they are of special importance for this study.
- Chapter 3 gives an overview of the reconstruction and identification of hadronically decaying taus in ATLAS.
- In chapter 4 the neutral pion reconstruction algorithm is presented. The development of the algorithm is documented in detail.
- In chapter 5 the performance of the neutral pion reconstruction is studied.
- In chapter 6 an outlook including prospects of the validation of the algorithm in data and ideas for further improvements is given.
- In chapter 7 the conclusions of this thesis are presented.

Chapter 1

Theoretical introduction

In this chapter the theoretical background for the study is provided. In the first section the Standard Model of particle physics is briefly introduced. Thereafter the decay modes of tau leptons, the decay kinematics and tau polarization are discussed.

1.1 The Standard Model of particle physics

The Standard Model (SM) of particle physics is a Lorentz invariant local quantum field theory that describes the properties of the elementary particles and their interactions, excluding gravity[1]. It was developed around 1970 and to this time describes most experimental data with high precision. All elementary particles predicted by the Standard Model have been discovered, except the Higgs boson. Recently a new particle with a mass of approximately 125 GeV, which is consistent with a SM Higgs boson [1, 2], was observed by the ATLAS and CMS experiments at the LHC.

The particles of the Standard Model (figure 1.1) are defined by a set of quantum numbers. They are divided into fermions, from which matter is made, vector bosons, which mediate forces, and the Higgs boson, which is the quantum of the scalar Higgs field that generates the mass of the elementary particles. Elementary fermions are further divided into quarks, which take part in strong, electromagnetic and weak interactions, and leptons, which do not take part in strong interaction. There are three generations of quarks and leptons. They are identical except for the particle masses. In each generation there is one quark with electric charge $2/3$, one quark with charge $-1/3$, one lepton with charge -1 and one neutrino with charge 0. In addition each particle has an antiparticle that is identical except that all additive quantum numbers are inverted. Quarks and leptons from the second and third generation are produced in high energy collisions and decay in one or more steps into first generation fermions. Apart from neutrino oscillations the number of leptons is conserved for each generation separately, thus in muon or tau decays there is always a muon- or tau neutrino produced (lepton flavor conservation). The quantum field theory describing the electromagnetic force is Quantum Electro Dynamics (QED). The exchange particle is the photon. It is massless and carries no charge. The theory of the strong force is Quantum Chromo Dynamics (QCD). The exchange particle is the gluon, which couples to color charge. It is massless and color charged itself. Color charged particles are always bound in color neutral hadrons (confinement). If they are separated, new color neutral objects are formed ('hadronization'). The weak force is mediated by the Z and W bosons, which couple to weak charge. The $W^{\pm}$ is the only exchange particle that carries electrical charge. No flavor changing neutral currents are observed in nature, so all decays that require a flavor change happen via charged weak interactions. In the Standard Model the electromagnetic and weak forces are unified to the electroweak force. For energies above approximately 100 GeV there is electroweak symmetry. For lower energies this symmetry is spontaneously broken

[1] No quantum field theory of gravity has been developed, yet. Also gravity can be neglected for energies far below the Planck scale ($\sim 10^{19}$ GeV), which are accessible for current experiments.

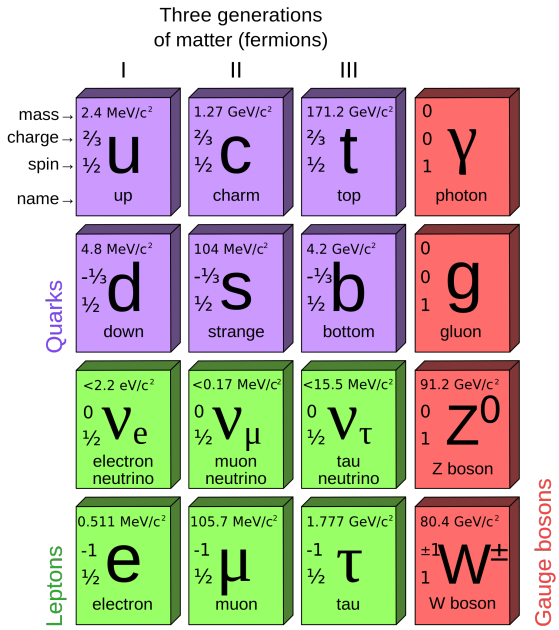

Figure 1.1: The Standard Model elementary particles confirmed so far. The masses of the light quarks (u, d and s) have large theoretical uncertainties, because they can only be calculated in non perturbative QCD and contribute only a small amount to the hadron masses observed. The Higgs boson is not shown. Image credit [3]

by the Higgs mechanism. It requires a doublet of scalar fields. Three of the four degrees of freedom generate the masses of the W^+, W^- and Z. The fourth degree of freedom corresponds to a physical Higgs boson. The SM Higgs mechanism not only generates the masses of the mediators of the electromagnetic and weak interaction but also the quark and lepton masses. For each fermion there is a parameter that describes the coupling of the fermion to the Higgs boson and that is proportional to the mass generated. The Standard Model can not predict the masses.

1.1.1 Shortcomings of the Standard Model

Although the Standard Model up to now is very successful in describing experimental data, there are unsolved issues:

- The SM does not contain a weakly interacting particle that can account for the observed dark matter in the universe.
- The SM does not explain the matter-anti-matter asymmetry in the universe. This would require baryon number violation and stronger CP violation than in the Standard Model.
- The SM does not include gravity.
- The SM has more than 20 free parameters (Weinberg angle, Higgs field vacuum expectation value, fermion masses, CKM matrix elements etc.), which is unsatisfactory for a fundamental theory.
- Fine tuning/hierarchy problem: The Higgs mass can be written as a sum of a 'bare' mass m_{H_0} and a radiative correction m_{corr} caused by loop diagrams. Because of the large difference of the electroweak scale ($O(100\,\text{GeV})$), the GUT scale ($O(10^{15}\,\text{GeV})$) and the Planck scale ($O(10^{19}\,\text{GeV})$)

m_{corr} is expected to be much larger than $O(100\,\text{GeV})$. Thus the Higgs mass would be significantly larger than $O(100\,\text{GeV})$ unless m_{H_0} and the masses determining m_{corr} are tuned very finely.

- The Standard Model is no 'Grand Unified Theory' in which strong force and electroweak force would be unified.

There are a large number of theories beyond the Standard Model that address one or more of these issues, some of which can be tested at the LHC. Examples are searches for further Higgs bosons, Supersymmetry, flavor changing neutral currents, lepton flavor violation, heavy gauge bosons, quark compositeness and extra dimensions in the TeV region. Taus play an important role in searches for new physics as they are promising signatures in many models beyond the Standard Model, e.g. in Supersymmetry models at large values of $\tan(\beta)$[2] or in the search for heavy Higgs Bosons, which preferentially couple to heavy particles.

1.2 Tau leptons

The tau lepton was discovered by Martin Lewis Perl with the LBL detector at SLAC in 1975 [4]. The Nobel Prize in Physics 1995 was awarded to him 'for the discovery of the tau lepton' [5]. Tau leptons have a lifetime of 291 fs and a mass of 1.777 GeV [6]. They are the heaviest leptons known to date.

1.2.1 Tau decay modes

Taus decay via the weak interaction (see figure 1.2). Because tau leptons are charged, there are always an odd number of charged particles in the final state. Hadronic decays are possible, because the tau mass is larger than the mass of light mesons. The most common hadronic final states involve ≤ 3 hadrons, because of the available phase space. Common tau decay modes and their branching fractions are listed in table 1.1. Strangeness production is Cabibbo suppressed, therefore decays into kaons are rare. Decays into more than one pion mostly happen via intermediate resonances, hereby the number of pions is defined by the resonance. Thus it is possible to determine the decay mode and (if there is one) the intermediate resonance by counting the charged hadrons and neutral pions. Charged pions or kaons are considered 'stable', i.e. they do not decay before being measured in the detector. Neutral pions, however, immediately decay via the electromagnetic interaction. The mode $\pi^0 \to \gamma\gamma$ strongly dominates (98.8 %), the only other relevant mode is $\pi^0 \to \text{e}^+\text{e}^-\gamma$ (1.2 %). Therefore the final tau lepton decay products measured in the detector are in most cases one or three charged pions and zero, one or two neutral pions resulting in zero, two or four photons.

1.2.2 Kinematics in hadronic tau decays

Tau decays into a tau neutrino and a charged hadron are two body decays. Thus in the tau rest frame the 3-momenta of the neutrino and the hadron are balanced and the sum of their energies is the tau mass. The neutrino does not interact in the detector, it contributes to the missing energy and momentum of the event. The hadron h or its decay products are therefore called the 'visible tau decay products'. Because the neutrino mass can be safely neglected, the visible energy and momentum in the tau rest frame are

[2] $\tan(\beta)$ is the ratio of the vacuum expectation values of the two Higgs doublets in the Minimal Supersymmetric Standard Model (MSSM).

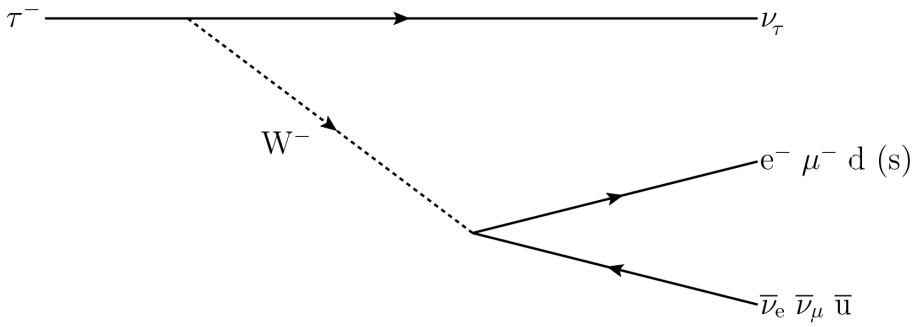

Figure 1.2: Leading order τ^- decay diagram. The decay mode is determined by the decay products of the virtual W-boson ($e^-\overline{\nu}_e$, $\mu^-\overline{\nu}_\mu$, $d\overline{u}$ or $s\overline{u}$). Strangeness production is Cabibbo suppressed.

category	decay mode	branching fraction / %
leptonic	$\tau^- \to e^-\nu_\tau\nu_e$	17.83 ± 0.04
	$\tau^- \to \mu^-\nu_\tau\nu_\mu$	17.41 ± 0.04
hadronic 1-prong	$\tau^- \to$ 1h ≥ 0 neutrals ν_τ	49.47 ± 0.10
	$\tau^- \to \pi^-\nu_\tau$	10.83 ± 0.06
	$\tau^- \to \rho^-(\to \pi^-\pi^0)\nu_\tau$	25.52 ± 0.09
	$\tau^- \to a_1^-(\to \pi^-\pi^0\pi^0)\nu_\tau$	9.30 ± 0.11
hadronic 3-prong	$\tau^- \to$ 3h ≥ 0 neutrals ν_τ	15.20 ± 0.08
	$\tau^- \to \pi^-\pi^-\pi^+\nu_\tau$ (mostly via a_1^-)	9.31 ± 0.06
	$\tau^- \to \pi^-\pi^-\pi^+\pi^0\nu_\tau$	4.62 ± 0.06
hadronic 5-prong	$\tau^- \to$ 5h ≥ 0 neutrals ν_τ	0.102 ± 0.004
hadronic 7-prong	$\tau^- \to$ 7h ≥ 0 neutrals ν_τ	$< 3 \cdot 10^{-5}$

Table 1.1: τ^- decay modes and branching fractions taken from the PDG [6]. The letter h denotes $\pi^\pm$ and $K^\pm$, neutral particles can be π^0, γ and K_L^0. τ^+ modes are charge conjugates of these modes. For hadronic 1-prong and 3-prong decays the first line shows the inclusive branching fraction, the following lines show the dominant decay modes.

given by

$$E_{\text{vis}} = \frac{m_\tau^2 + m_{\text{h}}^2}{2m_\tau} \qquad \text{and} \qquad |p_{\text{vis}}| = \frac{m_\tau^2 - m_{\text{h}}^2}{2m_\tau}.$$

In the laboratory frame, the 4-momenta of the visible tau decay products and the neutrino are boosted by the tau momentum. If h is a charged pion or kaon it is directly measured the in detector. In case h is a hadronic resonance the weak decay of the tau lepton is immediately followed by the strong decay of the resonance. The decay kinematics in the hadron's rest frame depend on the mass of the resonance and the number and the masses of its decay products.

1.2.3 Tau polarization

Taus are the only leptons whose polarization can be measured in ATLAS, because they are the only that decay in the detector. Tau polarization can be used in searches for bosons decaying into two taus. Firstly, the background from other ditau resonances can be suppressed, for example the otherwise irreducible $Z \to \tau\tau$ background in searches for neutral Higgs bosons. Secondly, the spin of a new ditau resonance can be measured once it is found. In the following the impact of tau polarization on the decay kinematics is shown for the principle hadronic τ^- decay modes[3]. Because pions are pseudoscalars the neutrino takes over the tau spin in decays $\tau^- \to \pi^-\nu_\tau$. As neutrinos are lefthanded the pion is preferably emitted along (against) the tau momentum for righthanded (lefthanded) taus. The angular distribution of the pion in the tau rest frame is $\propto (1 + P\cos(\theta^\star))$, where P is the tau polarization and $\theta^\star$ is the Gottfried-Jackson angle (figure 1.3). For decays into vector mesons like $\tau^- \to \rho^-\nu_\tau$ or $\tau^- \to a_1^-\nu_\tau$ angular momentum conservation requires the spin of the meson and the tau to be either perpendicular or aligned (figure 1.4). In case the spins are perpendicular the situation is the same as for the decay $\tau^- \to \pi^-\nu_\tau$, i.e. the neutrino takes over the spin component in direction of the tau spin and the angular distribution of the vector meson is $\propto (1 + P\cos(\theta^\star))$. However, if the spin of the meson and the tau are aligned, the spin direction of the neutrino must be opposite. This causes the angular distributions of the neutrino and the vector meson to flip, the latter now is $\propto (1 - P\cos(\theta^\star))$. The overall angular distribution of the vector meson depends on how often the spin of the meson and the tau are aligned or perpendicular. This in turn depends on the boost of the vector meson in the tau rest frame. Since the mass difference of the τ and the a_1 is relatively small the boost of the a_1 in the decay $\tau \to a_1\nu_\tau$ is small and both cases are almost as frequent. The angular distribution of the a_1 is thus almost independent of the polarization of the tau $((1 - P\cos(\theta^\star)) + (1 + P\cos(\theta^\star)) = 1)$. For $\tau \to \rho\nu_\tau$ decays, however, the boost of the rho in the tau system suppresses the case where the spins of the tau and the rho are aligned. Thus the momentum spectrum of the visible tau decay products contains information on the tau polarization, although the sensitivity is reduced by 50 %[4] [7]. Some information can be recovered by using the subsequent decay $\rho^- \to \pi^-\pi^0$: the pions are more often emitted in the spin direction of the rho, so e.g. the angle of the rho momentum and the charged pion momentum is sensitive to whether the spin of the rho and the tau are perpendicular or aligned. Assuming perfect reconstruction of this angle, sensitivity of $\tau^- \to \rho^-\nu_\tau$ decays would increase to approximately 85 % [7]. In a similar but more complicated and experimentally much more difficult way, it is possible to reach up to ~ 40 % of the sensitivity for $\tau \to a_1\nu_\tau$ decays.

One of the biggest motivations for this study is that tau polarization studies can benefit from the reconstruction of neutral pions. As discussed in section 1.2.1 decay modes can be predicted with large

[3] For τ^+ decays the $\overline{\nu}_\tau$ is always righthanded, otherwise they can be treated analogously.

[4] compared to the sensitivity of the same number of $\tau^- \to \pi^-\nu_\tau$ decays. It needs to be considered that rho decays are approx. 2.5 times as frequent (table 1.1).

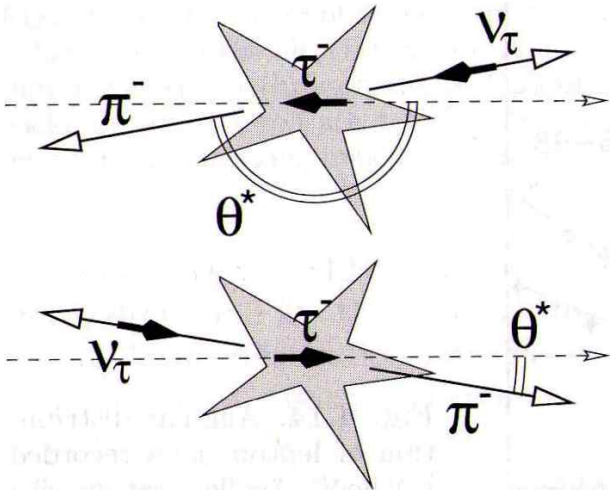

Figure 1.3: The decay $\tau^- \to \pi^- \nu_\tau$ in the rest frame of a lefthanded (upper plot) or righthanded (bottom plot) tau. The solid arrows mark the spins of the particles, the open arrows their momentum. The small open arrows on the right side mark the tau direction in the laboratory frame. $\theta^\star$ is the Gottfried-Jackson angle, i.e. the angle between the tau direction in the lab frame and the visible tau momentum (here pion momentum) in the tau rest frame. Image credit [7]

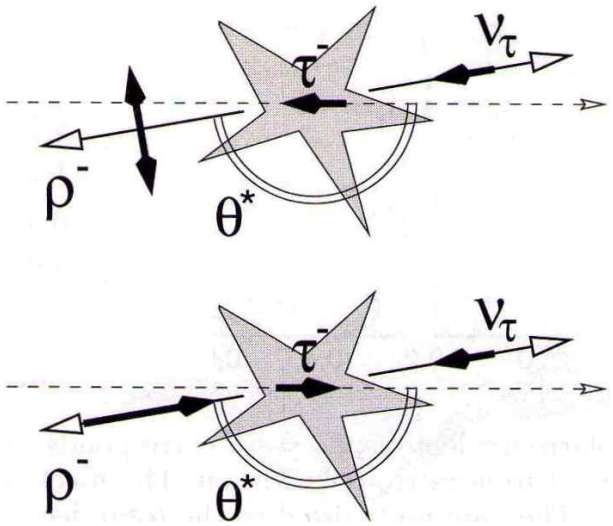

Figure 1.4: The decay $\tau^- \to \rho^- \nu_\tau$ in the tau rest frame. The rho spin can be transverse to the tau spin (upper plot) or aligned with the tau spin (bottom plot). The same possibilities exist for $\tau \to a_1 \nu_\tau$ decays, because ρ and a_1 are vector mesons. Image credit [7]

probability by counting the number of charged particles and neutral pions. Counting neutral pions thus helps to select tau decays that are more sensitive to polarization. Furthermore the sensitivity can be improved by an efficient reconstruction of the individual pion 4-momenta, because they include information on the spin direction of an intermediate resonance.

Chapter 2

The ATLAS Experiment at the Large Hadron Collider

In the first two parts of this chapter an overview of the LHC and the ATLAS detector is given, followed by an introduction to the ATLAS coordinate system and finally a more detailed description of the tracking system and of the calorimeter, which are the most important detector components for tau reconstruction.

2.1 Overview of the LHC

The LHC is a hadron-hadron collider operating at the European Organization for Nuclear Research (CERN) in Geneva. Counter rotating proton or heavy ion beams are accelerated and collided at four interaction regions. The LHC is currently operating at a center of mass energy of 8 TeV being the only particle accelerator to reach this energy range. The collisions are recorded by the general purpose detectors ATLAS and CMS, the LHCb detector, which is specially designed for studies of CP violation and rare B-meson decays, and the ALICE detector, which is specially suited for heavy ion collisions. First proton-proton collisions took place on November 2, 2009 [9]. Before the injection into the LHC ring the protons are accelerated to 450 GeV by an injector chain including the PS and SPS accelerators (figure 2.1). In the LHC the protons are accelerated by two independent RF systems, one per beam, each having eight superconducting cavities [10]. The LHC is 26.7 km long and lies between 45 m and 170 m below the earth's surface in the former LEP (Large Electron-Positron Collider) tunnel. As a p-p collider, it requires two separate rings with opposite magnetic field direction. Both beam pipes are located inside the same magnets. There are 1232 superconducting dipole magnets designed to produce magnetic field strengths up to 8.33 T, which are needed to deflect the proton beams at the design energy of 7 TeV per beam. The interaction regions lie in straight sections, where the beams share one pipe for approximately 130 m. In 2010 and 2011, protons were collided at a center of mass energy of 7 TeV. This year (2012), the energy was increased to 8 TeV. Instantaneous luminosities up to $6.76 \times 10^{33}\,\mathrm{cm}^{-2}\mathrm{s}^{-1}$ (design: $10^{34}\,\mathrm{cm}^{-2}\mathrm{s}^{-1}$) and 1380 bunches per beam (design: 2808) have been reached so far. An average number of interactions per bunch crossing of 31.87 has been achieved, which is already above the design value of 24. After the first long shut down in 2013/14 the LHC will restart physics collisions at 13 TeV in 2015.

2.2 Overview of the ATLAS detector

The ATLAS detector [11] is one of the general purpose detectors at the LHC. It is designed for

- the search for new phenomena at high energies,

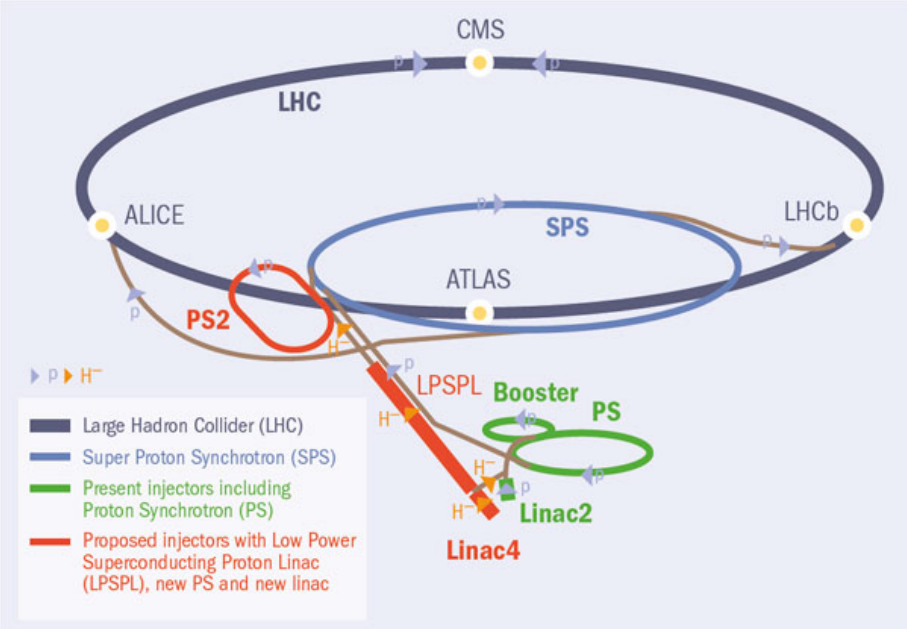

Figure 2.1: Schematic layout of the accelerator complex and the four LHC experiments at CERN. Image credit [8]

- the search for the Higgs boson,
- measurements of SM processes like QCD or electroweak processes, flavor- and top physics.

For these measurements it is necessary to identify and reconstruct the 4-momenta of photons, electrons, muons, taus, jets and the 4-vector of missing transverse energy carried by undetected particles. In most cases expected signal cross sections are small, thus the high luminosity of the LHC is necessary to provide sufficiently large data samples. In turn, however, there are on average 24 inelastic proton-proton scattering processes[1] in the same bunch crossing ('in-time pile up'). The time between two bunch crossings is only 25 ns, therefore the influence of particles produced in former collisions ('out-of-time pile up') on the measurement of the particles produced in in the collision of interest must be minimized.

The detector layout chosen is shown in figure 2.2. The main components are:

- **Tracking system:** Pixel detectors, silicon strip detectors, and transition radiation trackers measure the position of charged particles at several radii for track and vertex reconstruction. The tracking system is immersed in a selenoidial magnetic field of 2 T that deflects charged particles enabling a measurement of their transverse momenta.
- **Calorimeters:** In the liquid argon (LAr) electromagnetic calorimeter the energy of photons and electrons is measured. More material is required to stop hadrons, they also deposit energy in the tile or LAr hadronic calorimeters. The forward region is covered by an additional LAr calorimeter.
- **Muon system:** Apart from particles that do not interact in the detector at all, only muons pass the calorimeters. In the outer part of the detector they are deflected by the large toroidal magnets giving ATLAS its name ('**A** **T**oroidal **L**HC **A**pparatu**S**') and detected by tracking chambers.

[1] Numbers are valid for LHC design parameters (proton beam energy of 7 TeV, luminosity of 10^{34} cm^{-2}s^{-1} and 2808 bunches per beam).

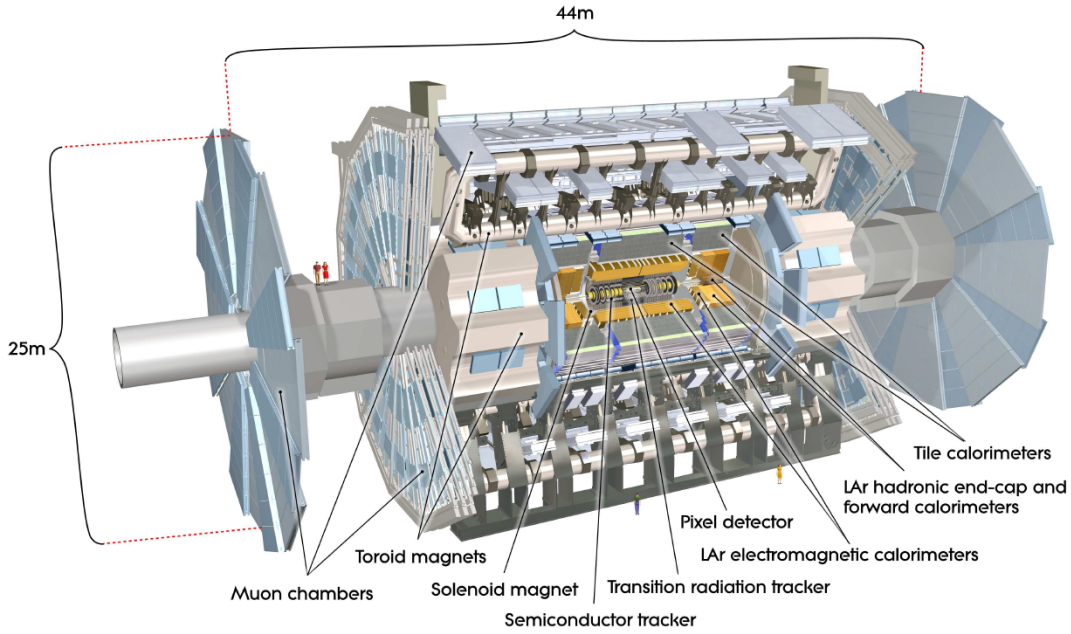

Figure 2.2: Cut-away view of the ATLAS detector. The total weight is approximately 7000 t. Image credit [11]

The high bending power of the magnetic field (up to 7.5 T m) and the large drift space enable measurements of high transverse momenta, the resolution is around 10 % for 1 TeV muons.

- **Trigger:** The trigger system selects the interesting events from the overwhelming number of uninteresting events from QCD processes keeping the amount of data stored acceptable. The ATLAS trigger system has three distinct levels, L1, L2 and event filter. The event rate of 40 MHz is reduced to about 75 kHz by L1 [11]. It uses a subset of the detector information to make a decision in less than 2.5 µs. L2 reduces the rate to about 3.5 kHz using the full information in regions of interest defined by L1. The L2 processing time is approximately 40 ms. The rate of events selected by the event filter to be stored is around 200 Hz with an event size of approx. 1.3 MB. Event filter decisions are based on offline analysis procedures, the processing time is about four seconds.

2.3 The ATLAS coordinate system

The origin of the ATLAS reference frame is defined as the nominal interaction point (IP) in the center of the detector. The x-axis points from the IP to the center of the LHC ring, the y-axis points upwards. The z-axis is parallel to the beam, its orientation is defined by the reference frame being right-handed. Transverse momentum and transverse energy are defined in the transverse (x, y) plane [11]. The azimuthal angle, ϕ, is defined in the transverse plane and it is measured in the range $(-\pi;\pi]$ with $\phi = 0$ in positive x-axis direction and $\phi = \pi/2$ in positive y-axis direction. The polar angle, θ, is the angle from the beam axis, it is defined in the range $[0;\pi]$ with $\theta = 0$ towards the z-axis. Pseudorapidity is defined as $\eta = -\ln(\tan(\theta/2))$, the distance in the pseudorapidity-azimuthal angle space is given by $\Delta R = \sqrt{\Delta\eta^2 + \Delta\phi^2}$.

2.4 The ATLAS tracking system

The tracking system (called the 'inner detector') measures the position of charged particles produced in the collisions at several radii, so their tracks can be reconstructed. To measure the origin of the tracks with high precision the tracking system is required to be as close to the beam pipe as possible. Because of the high particle flux – approximately 1000 particles are produced in each bunch crossing at LHC design parameters – high granularity is required to reconstruct the tracks of individual particles. For the same reason the detector components must be particularly radiation hard. The ATLAS inner detector (figure 2.3) consists of a pixel tracker, a silicon microstrip tracker (SCT) and a transition radiation tracker. It covers the pseudorapidity range of $|\eta| < 2.5$. Transverse momenta of charged particles can be determined by measuring the deflection in the 2 T magnetic field, which is provided by a superconducting solenoid. After the tracks are reconstructed they are extrapolated to the interaction point. Vertices at which two or more tracks meet are searched for by the software. The tracks can also be extrapolated to other layers of the detector, so they can be associated with energy deposits in the calorimeter or tracks in the muon system.

The transverse momentum resolution obtained with the inner detector increases with the transverse momentum of the particle that created the track, because it is less deflected by the magnetic field. Therefore the intrinsic resolution becomes a limiting factor for high transverse momenta and the dependence of the bending on the transverse momentum is smaller for high p_t. For low transverse momenta the resolution is dominated by multiple scattering. The resolution of the inverse transverse momentum of muons obtained with the inner detector can be parameterized as [11]

$$\sigma_{q/p_t} = 0.34\,\mathrm{TeV}^{-1} \cdot \left(1 \oplus \frac{44\,\mathrm{GeV}}{p_t}\right), \tag{2.1}$$

where q is the charge of the particle leaving a track.

2.5 The ATLAS calorimeter system

The ATLAS calorimeter system (figure 2.4) consists of sampling detectors with ϕ symmetry and coverage around the beam axis. It covers the pseudorapidity range of $|\eta| < 4.9$. Electromagnetic showers created by electrons or photons are measured by the liquid argon (LAr) electromagnetic calorimeter. Its thickness is > 22 radiation lengths (X_0) in the barrel and $> 24\,X_0$ in the end-caps[2], so it provides good containment for electromagnetic showers. Hadronic showers are measured in the electromagnetic and hadronic calorimeters, their combined thickness is approximately 9.7 hadronic interaction lengths (λ) in the barrel and $10\,\lambda$ in the end-cap[3]. Good energy resolution for high energy jets is provided, hadronic punch-through into the muon system is reduced below the irreducible level of muons produced in decays or in a collision of a hadron with the detector material. The forward part ($|\eta| > 2.5$) satisfies the requirements for jet reconstruction and measurements of missing transverse momenta. Higher granularity is used in the part covered by the tracking system ($|\eta| < 2.5$) making it suited for precision physics measurements. It is also the region in which hadronically decaying taus can be reconstructed and that therefore is relevant for this thesis.

The LAr electromagnetic calorimeter is the most important detector component for this study, because it measures, among other things, photons produced in tau decays. It is described in the next section. This

[2] X_0 is a material constant describing the energy loss of a particle causing an electromagnetic shower. After passing material with thickness X_0 the energy of the initial particle is on average reduced by a factor of $1/e$.

[3] λ is the thickness of material in which a hadron on average has one collision with a nucleus.

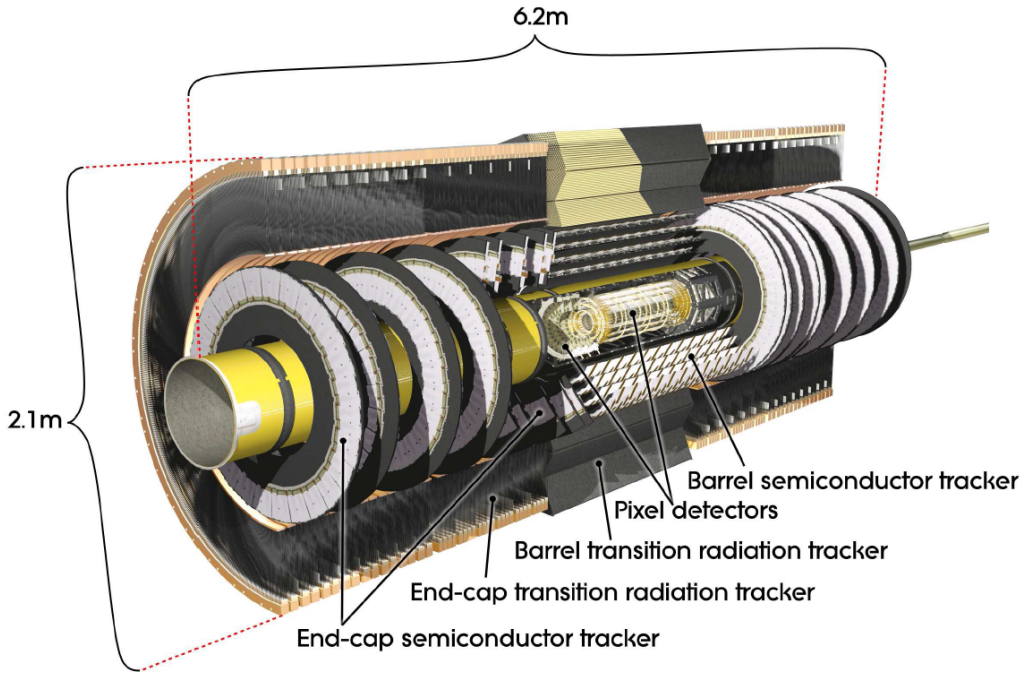

Figure 2.3: Cut-away view of the ATLAS tracking system. Image credit [11]

is followed by a description of the tile calorimeter and the hadronic end-cap measuring hadronic energy in the region devoted for precision physics. The final three sections focus on the calibration procedure, clustering of calorimeter cells and the performance of the calorimeter system. Further details regarding the calorimeter system can be found in Appendix A.

2.5.1 The liquid argon electromagnetic calorimeter

The electromagnetic calorimeter consists of one barrel part covering the pseudorapidity range of $|\eta| < 1.475$ and two end-cap parts covering the range $1.375 < |\eta| < 3.2$ (figure 2.4). The end-cap parts each share one cryostat with the LAr hadronic end-cap and the LAr forward calorimeter (figure 2.5), the barrel part is housed in its own cryostat. The electromagnetic calorimeter is a sampling calorimeter with lead as an absorber material and liquid argon as a sampling material. Electromagnetic showering is initiated in the lead absorbers. The particles produced in the shower ionize the argon atoms and the freed electrons are accelerated by a high voltage towards electrodes. Liquid argon has been chosen for its intrinsic linear behavior, stability of response over time and radiation hardness. The lead absorbers have an accordion geometry, which provides ϕ symmetry without uninstrumented gaps and allows for a longitudinal segmentation. The thickness of the lead plates in the barrel is 1.53 mm for $|\eta| < 0.8$ (central barrel) and 1.13 mm for $|\eta| > 0.8$ (extended barrel). This limits the increase of the amount of sampling material traversed by a particle for higher η. In the end-cap the lead plates are 1.7 mm thick for $|\eta| < 2.5$ and 2.2 mm for $|\eta| > 2.5$. A sketch of an electromagnetic calorimeter barrel module at $\eta = 0$ is shown in figure 2.6. The first of the three layers has a fine granularity in $|\eta|$ providing good spacial resolution for electromagnetic showers and early hadronic showers, i.e. showers starting before or in the first layer. It is often called the 'strip layer'. The second layer is approximately 16 radiation lengths thick and contains most of the energy of electrons and photons. The cells have a square shape in η and ϕ, the segmentation in ϕ is finer than in the strip layer. In most cases electromagnetic showers are contained

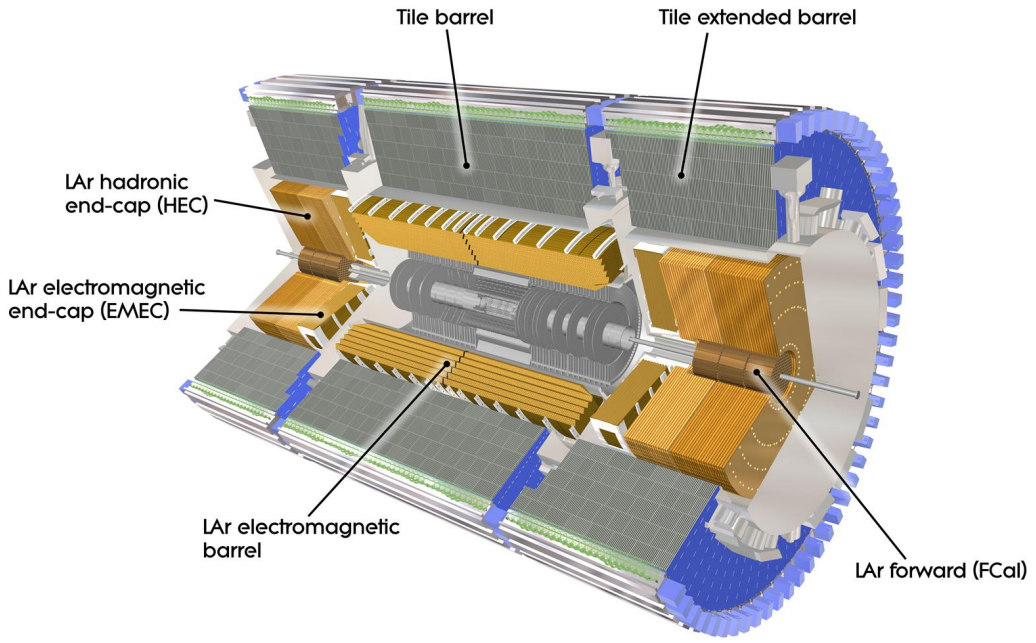

Figure 2.4: Cut-away view of the ATLAS calorimeter system. The cryostats, which surround the LAr calorimeters, are visible. The tracking system can be seen as well. Image credit [11]

within the first two layers, the last layer only contains hadronic energy and tails of long electromagnetic showers. In the pseudorapidity range $|\eta| < 1.8$ one additional layer, the presampler, is placed before the main electromagnetic calorimeter accordion. It is a separated 11 mm thin LAr calorimeter, its purpose is to measure showers initiated in front of the electromagnetic calorimeter.

2.5.2 The tile hadronic calorimeter

The tile hadronic calorimeter is divided into one central barrel part and two extended barrel parts (figure 2.4). They are situated outside the barrel- and end-cap cryostats, respectively, together they cover the pseudorapidity range of $|\eta| < 1.7$. Scintillator tiles are used as a sampling medium and steel as an absorber material. The particles produced in the collision of a hadron with a nucleus excite atoms in the scintillator. The absorbed energy is remitted in form of light, which is detected by photomultipliers after being transfered by a wave length shifting fiber. The mechanical assembly of the scintillator tiles, absorber material and the components of the optical readout system are shown in figure 2.7. The layout has been chosen such that costs are minimized for the required instrumented detector material. The tile calorimeter alone has a thickness of approximately 7.4 interaction length.

2.5.3 The liquid argon hadronic end-cap calorimeter

The LAr hadronic end-cap calorimeter is located in the end-cap cryostat behind the electromagnetic end-cap calorimeter (figure 2.5). It consist of two wheels, one front wheel and one rear wheel. Each wheel has two longitudinal layers. The sampling material is liquid argon, the absorbers are flat copper plates. The layout of the readout electrodes has been optimized to reduce space-charge effects due to the large particle flux in the forward region.

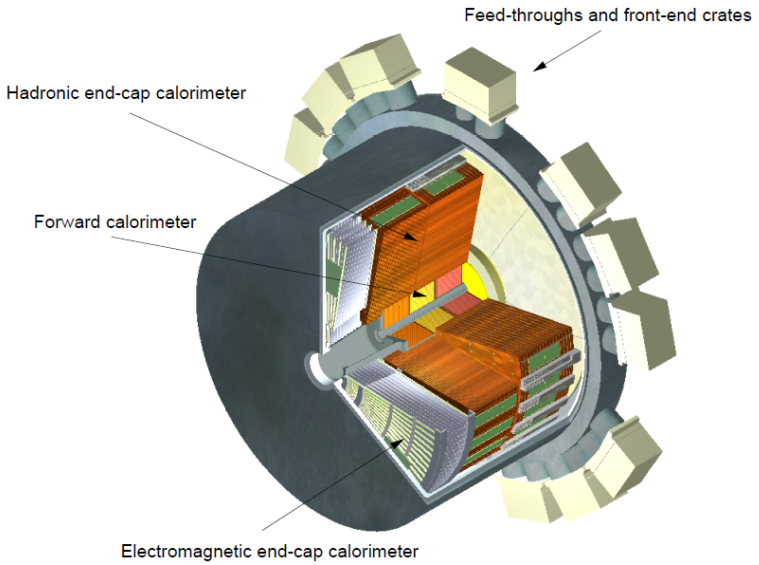

Figure 2.5: Cut-away view of one of the end-cap cryostats. The position of the electromagnetic end-cap calorimeter, the LAr hadronic end-cap calorimeter and the forward calorimeter can be seen. All these components are LAr sampling detectors. The electromagnetic calorimeter is on the inner side facing the tracking system. Image credit [11]

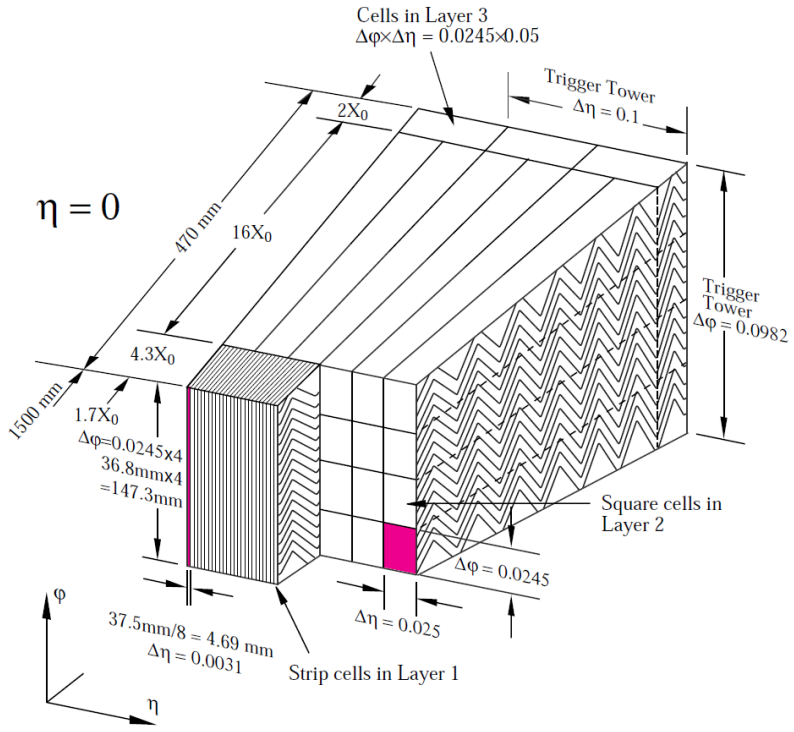

Figure 2.6: Sketch of an electromagnetic calorimeter barrel module. The three layers and the granularity in η and ϕ are shown. The accordion shape of the lead absorbers is visible. Image credit [11]

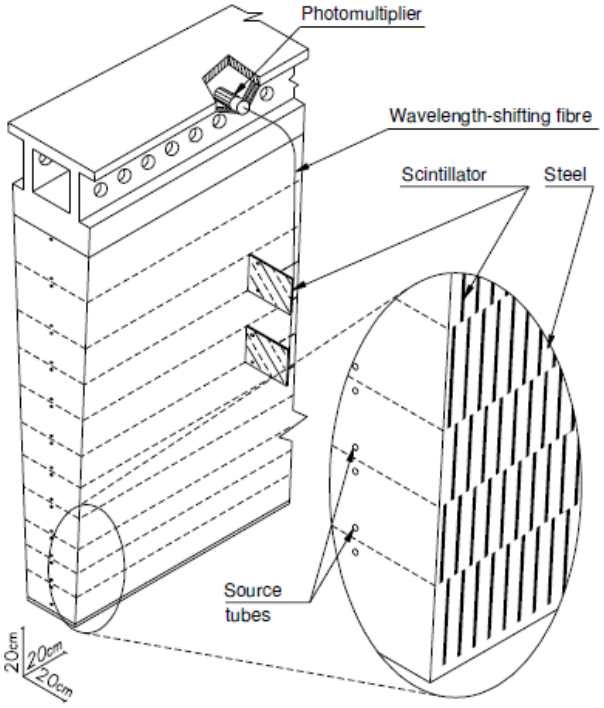

Figure 2.7: Schematic view of the mechanical assembly of the hadronic tile calorimeter. The ratio by volume of steel and scintillator tiles is approx. 4.7 : 1. The components of the optical readout, wave length shifting fibers and photomultipliers, are shown. Image credit [11]

2.5.4 Calibration of the calorimeter system

Since all the components of the calorimeter system are sampling calorimeters not all of the energy is deposited in the sensor material. Different absorber materials, sampling materials, sampling fractions and readout systems are used, so the energy response is different for the calorimeter components. The response is also dependent on the position of the cell, as e.g. the cell geometry is η dependent, and it is worse for hadronic showers than for electromagnetic showers. The calibration technique used in ATLAS [12] is based on a technique developed by the H1 experiment [13]. In this thesis the so called 'local hadron calibration' is used. Hereby the calibration weight of a cell depends on the calorimeter component, the position of the cell and the energy measured. The cell energy is used to recognize hadronic showers, which have lower energy densities.

2.5.5 Clustering

Calorimeter cells are grouped together in three-dimensional clusters based on their energy deposits. Noise is suppressed by requiring that the energy must be above a certain 'noise threshold'. In this thesis the so called topological clustering algorithm is used, which is the standard clustering algorithm for calorimeter cells in ATLAS. It is described in detail in [14]. After finding areas in the calorimeter where significant amounts of energy were deposited, local maxima are searched for to try and distinguish overlapping showers.

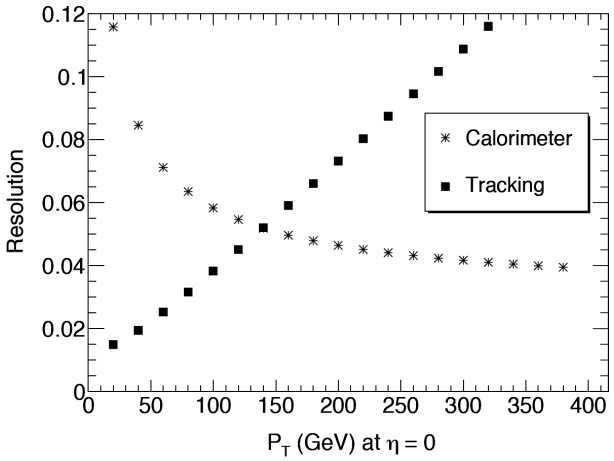

Figure 2.8: Energy (or transverse momentum resolution) of single charged pions at $\eta = 0$ in the ATLAS calorimeter and tracking systems. Image credit [15]

Subsystem	$a/\% \sqrt{\text{GeV}}$	$b/\%$	$\frac{\sigma}{E}\big\vert_{E=20\,\text{GeV}}/\%$	$\frac{\sigma}{E}\big\vert_{E=100\,\text{GeV}}/\%$
Electromagnetic calorimeter	10.1	0.17	2.3	1.0
Tile calorimeters	56.4	5.5	13.8	7.9
LAr hadronic end-cap	70.6	5.8	16.8	9.1

Table 2.1: Fit parameters for equation 2.2 [11]. As an example the relative resolutions for energy deposits of 20 GeV and 100 GeV are given.

2.5.6 Performance

The energy resolution of the calorimeter subsystems can be parameterized as

$$\frac{\sigma}{E} = \frac{a}{\sqrt{E/\text{GeV}}} \oplus b, \tag{2.2}$$

where E is the Energy deposited in the subsystem, a is a stochastic term and b is a constant term describing local non-uniformities of the calorimeter response. The resolution of the electromagnetic calorimeter has been tested using an electron test beam. Charged pions were used to test the performance of the tile hadronic calorimeter and the LAr hadronic end-cap. The energy resolution has been parameterized using equation 2.2, the fit parameters are shown in table 2.1. The relative resolution improves with energy, because the statistical fluctuations dominating the resolution for low energies become less important. Figure 2.8 shows the relative energy resolution of the calorimeter and the relative transverse momentum resolution for charged pions at $\eta = 0$, where $p_\text{t} = p = E$. The last equality sign holds, because the pion mass can be safely neglected. The calorimeter and the inner detector show complementary behavior: Below $\sim$ 150 GeV the tracking resolution is better than the calorimeter resolution, the opposite is the case for $p_\text{t} \gtrsim 150\,\text{GeV}$.

Chapter 3

Hadronically decaying taus in ATLAS

In this chapter the information on reconstruction and identification of hadronically decaying taus in ATLAS is provided that is required for the study. The first part focuses on the signature of hadronically decaying taus. In the second part the reconstruction procedure is discussed.

3.1 Signature of hadronic tau lepton decays

The detector signature of hadronically decaying taus (τ_{had}) is the composition of the signatures of the visible decay products. Because of the boost of the tau lepton the decay products are collimated, similar to the particles in a quark- or gluon-initiated jet. In addition there is missing transverse momentum, which is carried by the neutrino from the tau decay. In most cases the visible decay products are one or three charged pions and zero, two or four photons, which are daughters of neutral pions (compare section 1.2.1). The signature expected of a charged pion (or kaon) is a track in the tracking system and an energy deposit in the electromagnetic and/or hadronic calorimeter. The signature of a photon depends on whether it converts into an e^+e^--pair. In case it does not convert the photon creates an electromagnetic shower in the electromagnetic calorimeter. Otherwise the electron and positron each create an electromagnetic shower. These showers, however, are merged, unless the momentum of the photon is so small that they are significantly deflected by the magnetic field. Thus the signature in the calorimeter is usually similar to that of an unconverted photon. However, the energy of converted photons cannot be measured as for unconverted photons (figure 3.1). If conversion takes place in the beam pipe or the inner part of the tracking system there can be conversion tracks. They can be identified, because they do not come from the interaction point. As the momentum exchange in a neutral pion decay is small the two photons are very close to each other in the detector unless their momentum is small (left plot in figure 3.2). Thus the showers created by the photons are usually merged. The distance of charged and neutral pions is typically larger (right plot in figure 3.2). However, if a charged pion starts showering in the electromagnetic calorimeter its shower can overlap or merge with a neutral pion shower, especially at high momenta (figure 3.3). In this case the electromagnetic and hadronic showers can be assigned to the same cluster (figure 3.4).

3.2 Reconstruction and identification of hadronic tau lepton decays

The signature of hadronically decaying taus can be distinguished from that of electrons, muons and quark- or gluon-initiated jets. Therefore dedicated reconstruction and identification algorithms are required. The main goals are:

- efficient tau identification combined with high background rejection,
- good resolution of the 4-momentum,

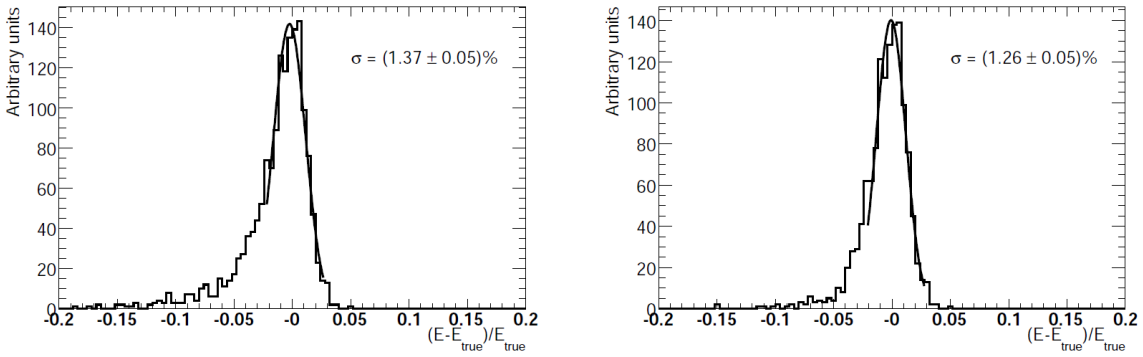

Figure 3.1: Energy resolution for Monte Carlo generated photons with an energy of 100 GeV at $|\eta| = 1.075$. The difference between measured and true energy divided by the true energy is shown for all photons (left) and all photons that did not convert in the inner detector (right). A Gaussian function is fitted to the central part of the distribution. The widths of the Gaussian functions are given. Image credit [11]

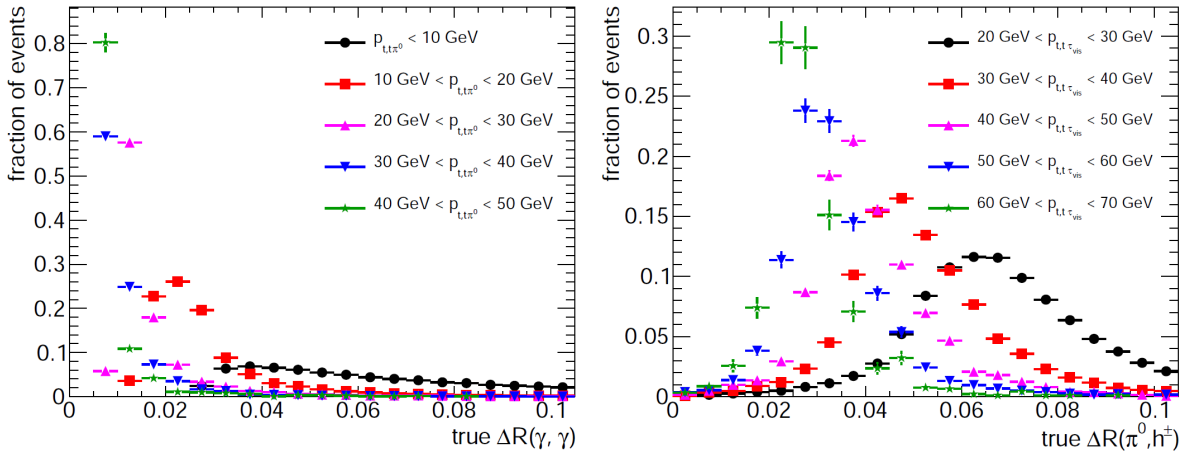

Figure 3.2: Distribution of the distance $\Delta R = \sqrt{\Delta\eta^2 + \Delta\phi^2}$ of decay the products in hadronic tau lepton decays. The left plot shows the true distance of the photons produced in subsequent neutral pion decays in bins of the true transverse momentum of the π^0. On the right the true distance of the π^0 and the true charged hadron in decays $\tau^{\pm} \to h^{\pm}\pi^0\nu_\tau$ is shown in bins of the true p_t of the visible tau. The distances decrease with p_t, because the decay products are more boosted. The data was obtained with $Z \to \tau\tau$ Monte Carlo simulation. The distributions are normalized to unity.

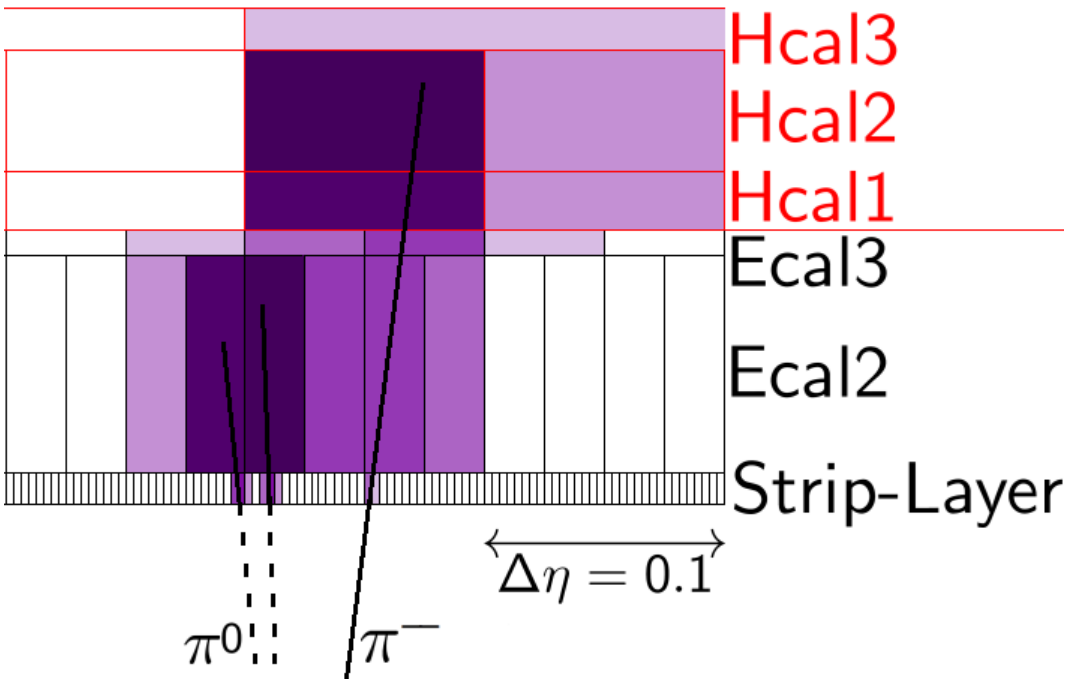

Figure 3.3: Schematic view of the signature of a $\tau^- \to \rho^- \nu_\tau$ decay in the ATLAS calorimeter (η projection). In the case shown the showers of the charged and neutral pion only have a slight overlap in the calorimeter. The three layers of the electromagnetic calorimeter accordion (Ecal) and the hadronic calorimeter (Hcal) are indicated. The darkness of the color indicates the amount of energy deposited in a cell. The granularities shown are valid around $\eta = 0$, however the figure is not true to scale.

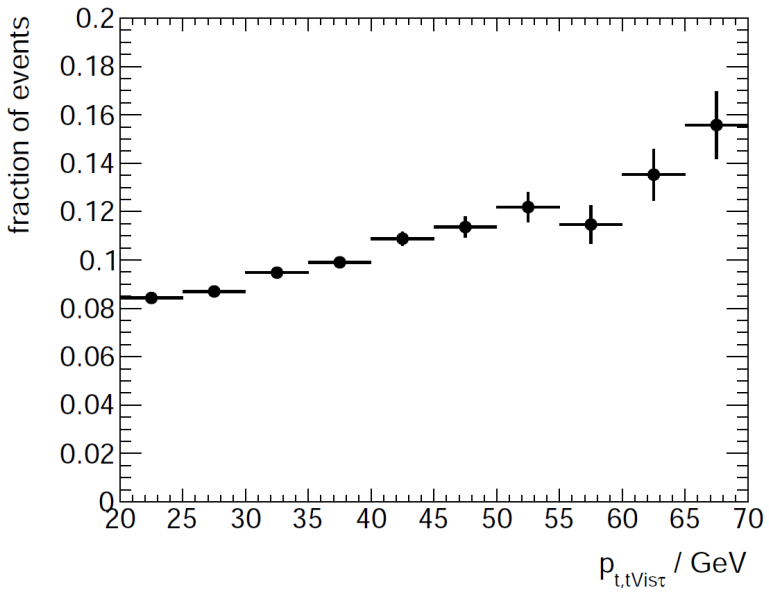

Figure 3.4: Fraction of cases, in which a true $\tau^\pm \to h^\pm \pi^0 \nu_\tau$ decay has one calorimeter cluster as a function of the true transverse momentum of the visible tau decay products. Clusters within the cone of $\Delta R < 0.2$ around the reconstructed tau candidate are counted. The fraction increases with p_t, as the electromagnetic and hadronic showers are more often merged for high momenta. For low momenta the decay products are not always contained in the cone. The data was obtained with $Z \to \tau\tau$ Monte Carlo simulation without pile up.

- reliable and efficient reconstruction of the substructure of the shower produced by the tau decay products, referred to as 'tau substructure' in the following,
- robustness against pile up,
- precise determination of identification efficiency, background rejection, energy resolution and substructure reconstruction efficiency.

The following description of the reconstruction and identification procedure for hadronically decaying taus in ATLAS is based on [16]. The starting point of the reconstruction are jets in the calorimeter. The jets are reconstructed using an anti-k_t algorithm [16] with a distance parameter of 0.4. Calorimeter jets automatically seed a τ_{had} candidate if they are in the acceptance range of the ATLAS tracking system ($|\eta| < 2.5$) and have a transverse momentum of $p_t > 10\,\text{GeV}$[1]. Tracks within the cone $\Delta R(\text{track}, \tau_{had}) < 0.2$ are associated with a tau candidate if they pass the following requirements:

- $p_t > 1\,\text{GeV}$,
- ≥ 2 hits in the pixel detector and ≥ 7 hits in pixel detector and SCT combined,
- $|d_0| < 1\,\text{mm}$ and $|z_0 \sin\theta| < 1.5\,\text{mm}$.

Hereby d_0 is the distance of closest approach to the reconstructed vertex in the transverse plane and z_0 is the longitudinal distance of closest approach. The vertex requirements and the p_t threshold provide rejection of pile up tracks, the hit requirements suppress noise and combinatorial background. In some cases 'real' tracks fail the requirements or cannot be reconstructed, e.g. because two tracks have been merged. Thus, while a τ_{had} candidate usually has one or three associated tracks it is possible that two or even zero tracks are reconstructed. 0-track candidates are typically discarded in analysis. The energy of the candidate is calculated using calorimeter clusters within the cone of $\Delta R < 0.2$. In addition to the calibration of the calorimeter cells discussed in section 2.5.4, calibration factors specific to hadronic tau decays are applied, which depend on the detector region, the transverse momentum of the candidate and on whether it has one associated track ('1-prong') or more tracks ('multi-prong'). The systematic uncertainties on the tau energy scale are in the order of 3–7% for most of the kinematic regions.

The primary background of hadronically decaying taus at the LHC are quark- or gluon-initiated jets (referred to as 'jets'). The main reason is that there is an overwhelming number of jets produced at hadron-hadron colliders. Additionally both jets and hadronically decaying taus contain charged hadrons and photons from neutral pions, so the detector signatures are similar. There are however two principle differences that are used to distinguish them:

- Jets are usually wider than hadronically decaying taus. The reason is that the underlying process is different: In case of τ_{had} there are one or more decays, in case of jets the underlying process is hadronization.
- The number of particles produced in a hadronic tau decay is typically smaller than in jets. Especially most hadronically decaying taus have one or three charged hadrons in the final state, while jets have a higher particle multiplicity.

Thus variables that are sensitive to the width of the shower and the particle multiplicity are derived for τ_{had} identification to suppress jets. These are used as input for two identification methods based on

[1] Most analysis, however, use only hadronically decaying taus with $p_t > 20\,\text{GeV}$.

a projected likelihood discrimination and a Boosted Decision Trees (BDT) discrimination. For each discriminant there are three working points defined, which correspond to target signal efficiencies of approximately 60 % ('loose'), 45 % ('medium') and 30 % ('tight'). The BDT identification provides the best background rejection and can archive rejection factors up to 300 for the tight working point. A second background for taus are electrons, which can mimic 1-prong τ_{had}. They can be distinguished by their compact signature in the calorimeter. The pure electromagnetic shower caused by an electron is typically shorter and less wide than the mixed or hadronic shower caused by a τ_{had}. In addition electrons usually ionize more atoms in the transition radiation tracker causing so-called 'high threshold hits'. Discrimination of electrons is performed using BDTs.

3.2.1 Reconstruction of the substructure of hadronically decaying taus

The reconstruction of the substructure of a τ_{had} candidate is part of the overall reconstruction process. The goal is to determine the decay mode, i.e. the number and particle identity of the visible decay products and their individual 4-momenta. The number of charged particles is determined from the tracking system. As charged kaons are rarely produced in τ_{had} decays (compare section 1.2.1) all charged decay products are assumed to be charged pions. Unless its transverse momentum is larger than 100 GeV the 4-momentum of a charged pion can be determined from the transverse momentum of the track. As there is more often a track lost due to the track selection than there is a mis-reconstructed ('fake') track, candidates with two tracks are assumed to be 3-prong candidates. For the reconstruction of the neutral pions it is required to separate the energy deposits in the calorimeter caused by the charged and neutral pions. In general those overlap or may even be merged. Additionally energy deposits from pile up and noise must be suppressed. The currently default reconstruction of neutral pions is done using a simple algorithm, which removes all the energy deposited close to tracks and identifies neutral pions in the remaining energy distribution of the electromagnetic calorimeter. It is outdated and going to be replaced. Two algorithms are proposed to run within the standard tau reconstruction software in ATLAS. One is calorimeter cluster based, the second is the algorithm proposed in this thesis, which is calorimeter cell based. A third method is part of an alternative tau reconstruction algorithm ('PanTau'), which is based on energy flow objects [15]. Until now the three approaches have been developed and tested separately. A detailed comparison of the performances is planned in the near future.

Chapter 4

Cell based reconstruction of neutral pions in hadronic tau decays

The goal of the algorithm proposed in this thesis is to determine the number of neutral pions produced in hadronic tau decays and to reconstruct their individual 4-momenta. The algorithm has so far been developed for 1-prong candidates only. As discussed in section 1.2.1 the most common tau decay modes involving neutral pions are $\tau^{\pm} \rightarrow \rho^{\pm}(\rightarrow \pi^{\pm}\pi^{0})\nu_{\tau}$ and $\tau^{\pm} \rightarrow a_1^{\pm}(\rightarrow \pi^{\pm}\pi^{0}\pi^{0})\nu_{\tau}$. They together correspond to 55 % of the hadronic branching fraction. Decays into more than one charged hadron and at least one neutral pion amount to about 8 % of the hadronic branching fraction. The algorithm developed in this thesis is the evolution of an algorithm that has been developed in a diploma thesis at the University of Heidelberg in 2009 [17]. For this thesis the algorithm has been completely redesigned. The most significant improvements are mentioned in the following sections. Currently the algorithm is being implemented into the official ATLAS reconstruction software. It is divided into two parts. Firstly, the subshower caused by the charged hadron is removed from the electromagnetic calorimeter on cell level. For this, averaged hadronic shower profiles estimated from Monte Carlo simulation are used. The remaining energy distribution in the electromagnetic calorimeter is re-clustered with the ATLAS topoclustering algorithm. In the second part of the algorithm neutral pion clusters are selected from the clusters found during re-clustering. This is done by using Boosted Decision Trees that use cluster shape variables to discriminate neutral pion clusters from background. One of the main motivation for this ansatz is that by removing the charged hadron's subshower neutral pions can be reconstructed even when the showers of the charged and neutral pion are merged into one cluster.

The first section discusses data samples used to develop and test the algorithm. Thereafter the two parts of the algorithm are described and discussed. The performance of the neutral pion reconstruction in Monte Carlo is discussed in chapter 5.

4.1 Simulated data samples

4.1.1 Single charged pion sample

A very pure sample of isolated charged hadrons with high statistics up to transverse momenta of ~100 GeV is required for studies of hadronic shower shapes. The available statistics in 'real' data is too small, as single charged hadrons are comparably rarely produced in QCD processes and have no dedicated trigger. Selecting $\tau \rightarrow \pi^{\pm}\nu$ decays in data is not possible without applying cuts that bias the shower shapes, since decays involving neutral pions must be suppressed. The data collected during the so-called 'Combined Test Beam' [18] is not available in the current reconstruction software release. Therefore hadronic shower shapes are studied in a sample of simulated single charged pions.

The sample used for this thesis contains two million of each positively and negatively charged pions. The selection of the charged pion candidates is summarized in table 4.1. Charged pions are recon-

Variable	Requirement
$\Delta R(\text{jet}, \pi^{\pm}_{\text{true}})$	< 0.2
$\lvert\eta_{\text{track}}\rvert$	< 2.5
Number of tracks	$= 1$
Number of calorimeter clusters	> 0

Table 4.1: Summary of the selection applied to the charged pions in the single pion samples.

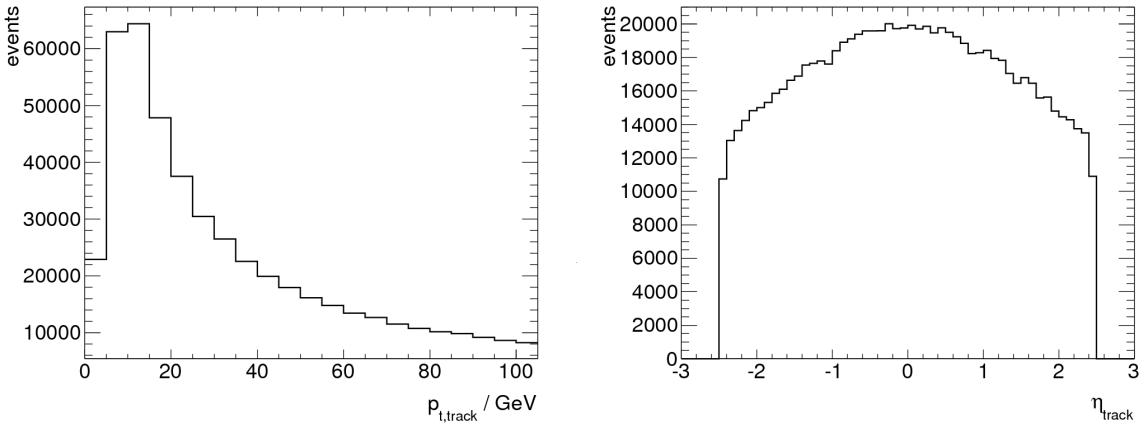

Figure 4.1: Transverse momentum and pseudorapidity spectra of the charged pions in the single pion samples.

structed as jets. The jets are required to be geometrically matched to generator level charged pions ($\Delta R(\text{jet}, \pi^{\pm}_{true}) < 0.2$). This way misidentified candidates are suppressed, which can be caused by noise. Only pions within the range of $|\eta| < 2.5$ are of interest, as taus are not reconstructed outside this region. The tracks from the charged pions are of importance for the analysis. Therefore candidates with no track or more than one track are rejected. For noise suppression only calorimeter cells within clusters are taken into account. Thus events without calorimeter clusters are rejected. Approximately 850 000 events (21 %) pass the selection. Half of the events fail the pseudorapidity requirement. Most of the other pions that fail the selection have no associated cluster. This happens if the energy of the charged pion is not sufficient to cause a significant energy deposit. Figure 4.1 shows the transverse momentum and pseudorapidity spectra after the selection.

4.1.2 $Z \rightarrow \tau\tau$ sample

The selection of neutral pion clusters for the training of the BDTs and the performance of the algorithm are studied in Monte Carlo simulated $Z \rightarrow \tau\tau$ events. The reason to use simulated events is that truth information on the particle identity and the 4-momenta is required in both cases.

Three samples of $Z \rightarrow \tau\tau$ events are used in this study. They mainly differ in the average number of reconstructed vertices as they were simulated with different pile up conditions and the center of mass energy of the collisions $\sqrt{s}$ (table 4.2). The first two samples were generated and processed with similar software versions as the sample of simulated single charged pions. Therefore they are the principle samples for the analysis. The 8 TeV sample is more recent, so the compatibility with the other samples is limited. It gives however an impression of the performance of the algorithm in a scenario with more pile up.

The event selection is summarized in table 4.3. τ_{had} candidates are geometrically matched to gen-

Sample	nVertex	$\sqrt{s}$/TeV	events	taus after selection	efficiency / %
$\sqrt{s}$ = 7 TeV no pile up	1.0	7	499999	255731	26
$\sqrt{s}$ = 7 TeV with pile up	6.3	7	301000	150990	25
$\sqrt{s}$ = 8 TeV with pile up	14.0	8	1500495	715354	24

Table 4.2: Compilation of the samples of simulated $Z \rightarrow \tau\tau$ events used in this study. The selection is defined in table 4.3.

Requirement	efficiency / %
Hadronic tau decay (truth level)	65
1-prong decay (truth level)	77
$\lvert\eta_{\tau_{\text{true}}}\rvert < 2.8$	82
$\Delta R(\tau_{\text{cand}}, \tau_{\text{true}}) < 0.2$ (incl. $\lvert\eta_{\tau_{\text{cand}}}\rvert < 2.5$)	82
One reconstructed track	74

Table 4.3: Summary of the selection applied to the charged pions in the single pion samples. The efficiencies are given for the 7 TeV sample with pile up.

erator level hadronically decaying taus. The algorithm operates on one-prong candidates. Thus reconstructed candidates without exactly one track or candidates that are matched to true multi-prong decays are rejected. The efficiency of the last selection criterion decreases slightly with pile up, because tracks caused by particles produced in a separate collision are sometimes associated with the tau candidate. Figure 4.2 shows the true transverse momentum spectra of the taus passing the selection for $\sqrt{s}$ = 7 TeV and 8 TeV. The number of taus passing the selection increases strongly around true transverse momenta of 10 GeV, since only jets with more than 10 GeV are seeds for tau candidates. Due to the higher boost of the Z bosons produced at $\sqrt{s}$ = 8 TeV the p_{t} spectrum is slightly shifted towards higher values. In figure 4.3 the transverse momentum and the pseudorapidity spectra of the tracks associated with the tau candidates are shown. Most tracks have transverse momenta below 40 GeV but the tail of the distribution reaches up to $\sim$ 100 GeV. In the pseudorapidity spectrum a small number of tracks with $|\eta| > 2.5$ can be observed. They are associated with tau candidates that are barely within the pseudorapidity boundary.

4.2 Removal of the charged hadron subshower

The goal of the first part of the algorithm is to remove the energy deposited by the charged hadron from the electromagnetic calorimeter so that – apart from noise and pile up contamination – only the energy deposited by neutral pions remains. No information on the energy distribution in the electromagnetic calorimeter is used in this part of the algorithm. Therefore it operates independently on whether neutral pion subshowers are present.

In the following the tile hadronic calorimeter, the LAr hadronic end-cap and the third layer of the LAr electromagnetic calorimeter are assigned to the 'hadronic calorimeter' (Hcal). The third layer of the electromagnetic calorimeter is counted as part of the hadronic calorimeter, because it contains mostly hadronic energy (compare section 2.5.1). Neutral pions are reconstructed in the remaining part of the electromagnetic calorimeter, which will still be referred to as 'electromagnetic calorimeter' (Ecal). The energy subtracted in each Ecal cell is calculated in three steps:

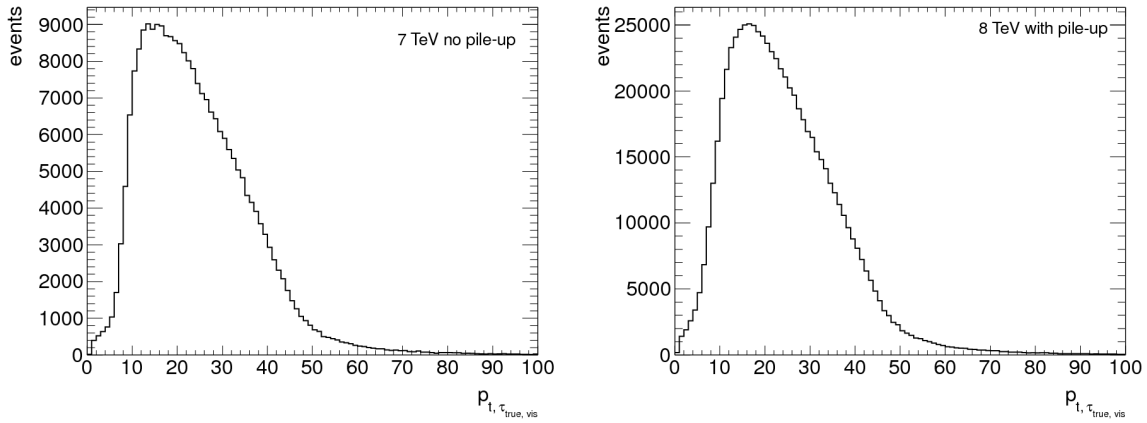

Figure 4.2: True visible transverse momentum spectra of taus in $Z \rightarrow \tau\tau$ events for $\sqrt{s} = 7$ (left) and 8 TeV (right).

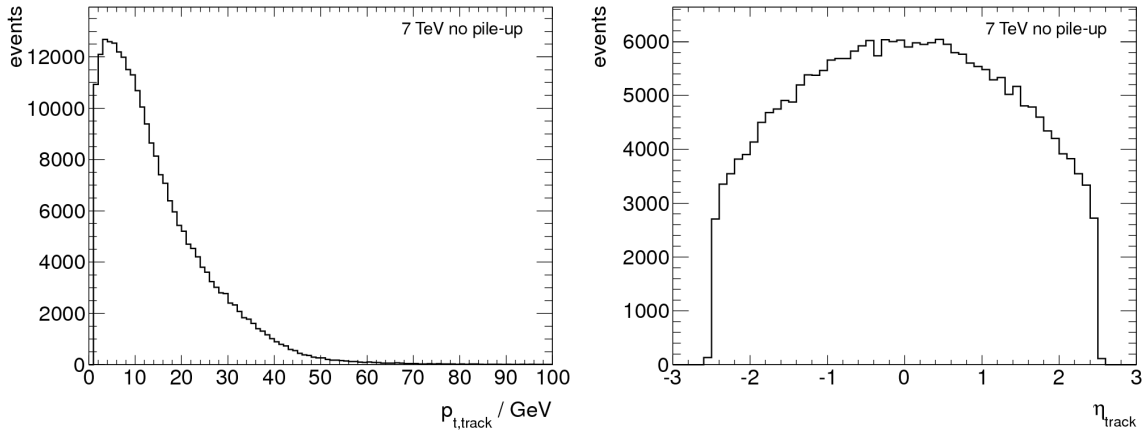

Figure 4.3: Transverse momentum (left) and pseudorapidity (right) spectra of the tracks in simulated $Z \rightarrow \tau\tau$ events.

1. the *total* amount of hadronic energy deposited in the electromagnetic calorimeter is estimated,
2. the hadronic energy deposited in each *layer* of the electromagnetic calorimeter is estimated,
3. the hadronic energy deposited in each *cell* of the layers of the electromagnetic calorimeter is estimated.

In the second and third step averaged hadronic shower shapes are used. They are obtained from the sample of simulated single charged pions. The subtraction procedure has been developed on candidates whose tau cone[1] is fully contained in the range of the electromagnetic barrel calorimeter ('barrel candidates'). In order to prepare the algorithm for the ongoing implementation into the official ATLAS reconstruction software a preliminary extension has been added, which enables the algorithm to run also in the end-cap and transition regions between barrel and end-caps. It now runs on all 1-prong candidates. In the following the subtraction method for barrel candidates is explained. Thereafter the extension to the end-cap and transition regions and the re-clustering are described. Finally the performance of the hadronic subshower removal is studied.

4.2.1 Estimation of the total hadronic energy in the electromagnetic calorimeter

The total amount of energy deposited by the charged hadron in the Ecal is determined from the track momentum p_{trk} and the energy E_{Hcal} deposited in the hadronic calorimeter:

$$E_{\text{Ecal}}^{\text{est}} \equiv p_{\text{trk}} - E_{\text{Hcal}}. \tag{4.1}$$

Hereby the energy of the charged hadron has been replaced by the track momentum. This can be done, because the pion mass is negligible for sufficiently large momenta as in the case of these studies[2]. The energy is calculated within the tau cone. The local hadron calibration is applied for the cell energies (cf. section 2.5.4). For noise suppression only cells are taken into account that are part of clusters. In the range of the tile hadronic barrel calorimeter, the hadronic energy is corrected in order to compensate for energy losses in the barrel cryostat, which is located between the electromagnetic barrel calorimeter and the tile hadronic calorimeter (see figure 2.4):

$$E_{\text{cryo}}^{\text{corr}} \equiv c_{\text{cryo}} \sqrt{E_{\text{Ecal3}} \cdot E_{\text{Tile0}}},$$

where E_{Ecal3} denotes the energy measured in the third layer of the electromagnetic calorimeter, E_{Tile0} is the energy measured in the first layer of the tile hadronic barrel calorimeter and c_{cryo} is the calibration factor of the correction [12]. Hereby the energy in the layers is calculated analogous to the energy in the hadronic calorimeter, i.e. using the cluster cells within the tau cone. The combined formula for the estimated hadronic energy in the electromagnetic calorimeter is

$$E_{\text{Ecal}}^{\text{est}} \equiv p_{\text{trk}} - \left(\sum_{i \in I_{\text{Hcal}}} (c_i E_i) + c_{\text{cryo}} \sqrt{E_{\text{Ecal3}} \cdot E_{\text{Tile0}}} \right), \tag{4.2}$$

where I_{Hcal} is the set of cells in the hadronic calorimeter with $\Delta R(\text{cell}, \tau_{\text{had}}) < 0.2$ that are part of clusters, E_i is the raw energy measured in cell i and c_i is the cell calibration weight. Due to the finite

[1] The 'tau cone' is the cone in which tracks and energy deposits are associated with the tau candidate: ΔR(tau candidate, object) < 0.2 (cf. section 3.2).

[2] Slight deviations occur for kaons with momenta $\lesssim 2$ GeV. These, however, are rare. In addition low energy charged hadrons are separated from potential other decay products by the magnetic field, so the quality of subtraction is not critical.

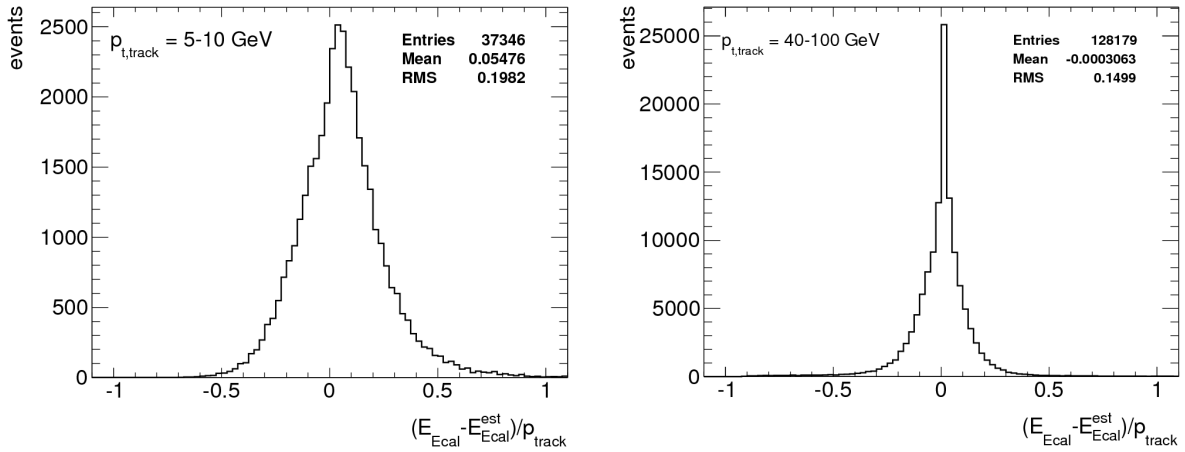

Figure 4.4: Resolution of $E^{\text{est}}_{\text{Ecal}}$ normalized to the track momentum for $p_{\text{t, track}} = 5-10\,\text{GeV}$ (left) and $p_{\text{t, track}} = 40-100\,\text{GeV}$ (right).

resolution of the hadronic calorimeter and the tracking system, E_{Hcal} can exceed the measured track momentum, if the charged hadron deposits most of its energy in the hadronic calorimeter. In this case $E^{\text{est}}_{\text{Ecal}}$ is set to zero, i.e. no energy is subtracted in the electromagnetic calorimeter.

The accuracy of the estimation is validated using the samples of simulated single charged pions. For this sample, $E^{\text{est}}_{\text{Ecal}}$ should equal the energy measured in the electromagnetic calorimeter (E_{Ecal}). Figure 4.4 shows the resolution of $E^{\text{est}}_{\text{Ecal}}$ normalized to the track momentum in two transverse momentum bins. The RMS of the distribution is in the range of 15 – 20 %. The slight bias in the plot for low transverse momenta is due to the event selection: Candidates without clusters have been rejected, because only cells within clusters are used for the study of the hadronic shower shapes. Charged and neutral pion showers are more likely to overlap for high transverse momenta: Firstly, charged particles with low momenta are separated from other decay products by the magnetic field. Secondly, pions with high energy are produced in high momentum decays, in which the decay products are more collimated. A useful feature is that the estimation becomes more precise in this case, because the calorimeter resolution improves. This applies until the transverse momentum of the track exceeds approximately 140 GeV and the tracking resolution becomes dominant (cf. figure 2.8 of section 2.5.6).

A possible extension of the algorithm for multi-prong candidates is discussed in section 6.2.1. This would allow the algorithm to run on all τ_{had} candidates.

4.2.2 Estimation of hadronic energy in each layer of the barrel electromagnetic calorimeter

As the next step $E^{\text{est}}_{\text{Ecal}}$ is distributed to the three layers of the electromagnetic calorimeter. For this, weights for the presampler (PS), the strip layer (Ecal1) and the second layer of the electromagnetic calorimeter (Ecal2) are determined. These weights are referred to as 'longitudinal weights' in the following, since they are related to the longitudinal shower shape. The tracks associated with the charged pion are extrapolated to the layers of the calorimeter. Cells that are closer than $\Delta R = 0.2$ to the extrapolated track position are taken into account for the calculation of the longitudinal weights. For noise suppression only cells within clusters are used. The longitudinal weight of a layer $\ell \in \{\text{PS}, \text{Ecal1}, \text{Ecal2}\}$

Variable	bin 0	bin 1	bin 2	bin 3	bin 4
$p_{\mathrm{t,\,track}}$	1–5 GeV	5–10 GeV	10–40 GeV	40–100 GeV	> 100 GeV
$\lvert\eta_{\mathrm{track}}\rvert$	0.0–0.6	0.6–1.3	1.3–1.6	>1.6	
hadF	0.0–0.6	0.6–1.0			

Table 4.4: Definition of the binning for studies of hadronic shower shapes. The $|\eta|$ bins shown in gray correspond to the transition- and end-cap regions of the electromagnetic calorimeter. Charged hadrons with transverse momenta above 100 GeV occur very rarely in $Z \to \tau\tau$ decays and are thus of less importance for this study.

is defined as:

$$w_\ell \equiv \frac{\sum\limits_{\text{pions}} \left(\sum\limits_{i \in I_\ell} (c_i E_i) \right)}{\sum\limits_{\text{pions}} (E_{\text{Ecal}})}. \tag{4.3}$$

Hereby I_ℓ is the set of cells within clusters in layer ℓ. One of the main goals of this study is to reduce inaccuracies of the hadronic subshower removal due to variations of the hadronic shower shapes on a shower-by-shower basis. For this a binning of the hadronic shower shapes has been introduced in the algorithm developed in this thesis. Information on the shape in the electromagnetic calorimeter cannot be used for binning, as it may be affected by neutral pion subshowers. On the other hand the information on the track and the energy distribution in the hadronic calorimeter are unaffected and can be used. The following variables are found to be useful for a binning of the hadronic shower shapes:

- the transverse momentum of the track $p_{\mathrm{t,\,track}}$,
- the absolute value of the pseudorapidity of the track $|\eta_{\mathrm{track}}|$,
- the 'hadronic fraction' hadF $\equiv E_{\mathrm{Hcal}}/p_{\mathrm{track}}$,

The binning is defined in table 4.4. The longitudinal weights are separately calculated for each three-dimensional bin using equation 4.3. Figure 4.5 shows the longitudinal weights for the barrel region. Of the binning variables the transverse momentum of the track has the largest correlation to the hadronic shower shape in the electromagnetic calorimeter. Showers of particles with high transverse momenta are longer, which means that more energy is deposited in Ecal2. This difference is most pronounced for low transverse momenta, therefore a finer binning is chosen in this region. The longitudinal weights for Ecal2 are larger for the high hadronic fraction bin. The reason is that showers have larger hadronic fractions if they start later. The differences between central barrel ($|\eta| < 0.8$) and extended barrel ($0.8 < |\eta| < 1.3$) are caused by the variations of the amount of material in and in front of the layers of the electromagnetic calorimeter (cf. figure A.1 of Appendix A). For example the longitudinal weights of the presampler are slightly larger for the extended barrel, since there is more material in front of it.

In figure 4.6 the fluctuation of the fraction of hadronic energy deposited in Ecal1 is shown for both hadronic fraction bins for the central barrel and transverse momenta of 10 – 40 GeV. Fluctuations in each bin are significantly reduced by the binning, e.g. the smaller longitudinal weight for Ecal1 obtained for candidates with high hadronic fraction is usually closer to the energy fraction deposited in Ecal1 by candidates with high hadronic fraction. For the low hadronic fraction bin a separation into candidates that deposit $\sim$ 25 – 30 % of the energy in Ecal1 and candidates that deposit very little energy in Ecal1 can be seen. This corresponds to candidates for which showering is initiated in or before Ecal1 and candidates that start showering in Ecal2. In the future it may be possible to distinguish these candidates by using the fine granularity of Ecal1 (see section 6.2.1).

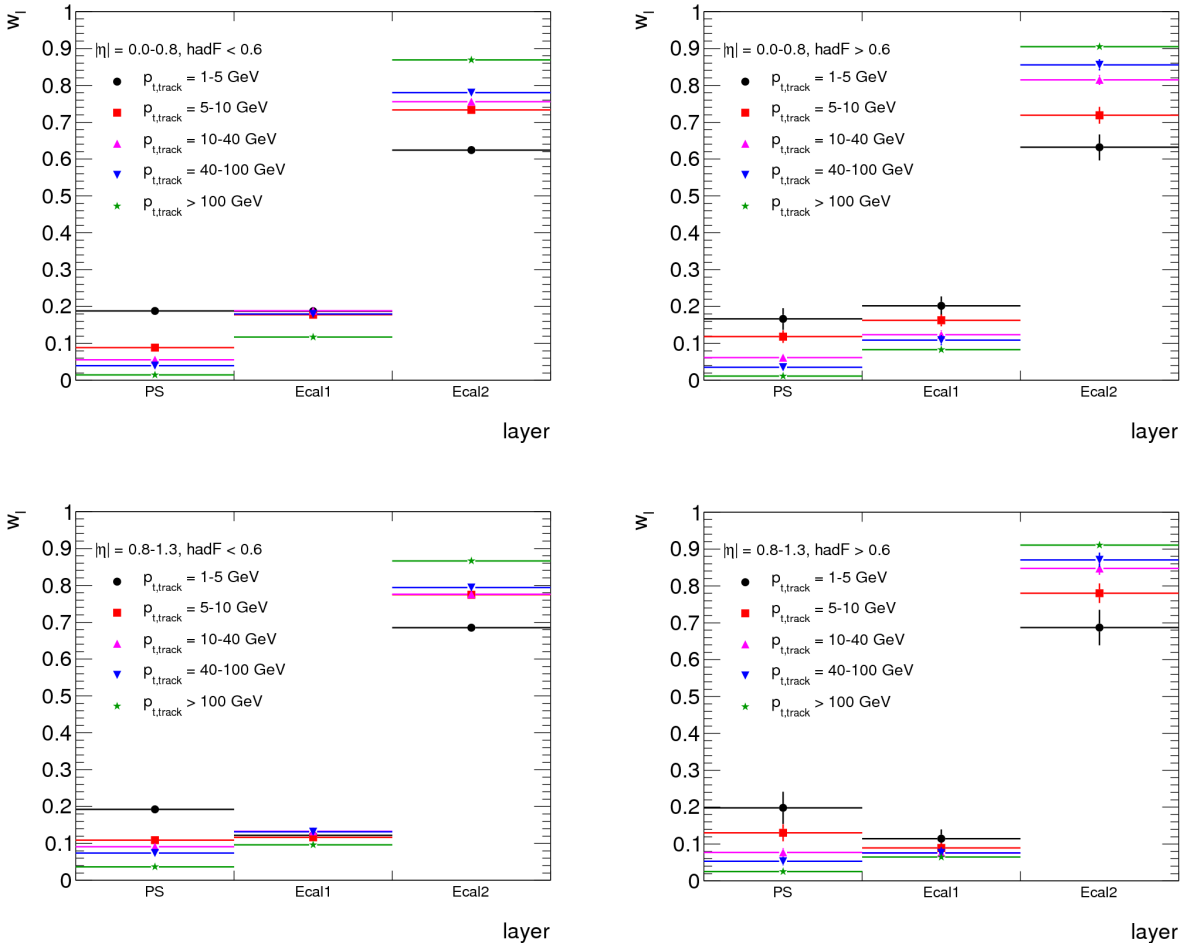

Figure 4.5: Longitudinal weights for hadronic shower subtraction in the electromagnetic calorimeter. The weights are shown in two hadronic fraction bins (left/right), two eta bins in the barrel region (top/bottom) and five transverse momentum bins (colors). The statistical errors on the longitudinal weights are shown. Less total energy is deposited in the Ecal for the high hadronic fraction bin and for the low transverse momentum bins, which increases the statistical uncertainty of the longitudinal weights in these bins.

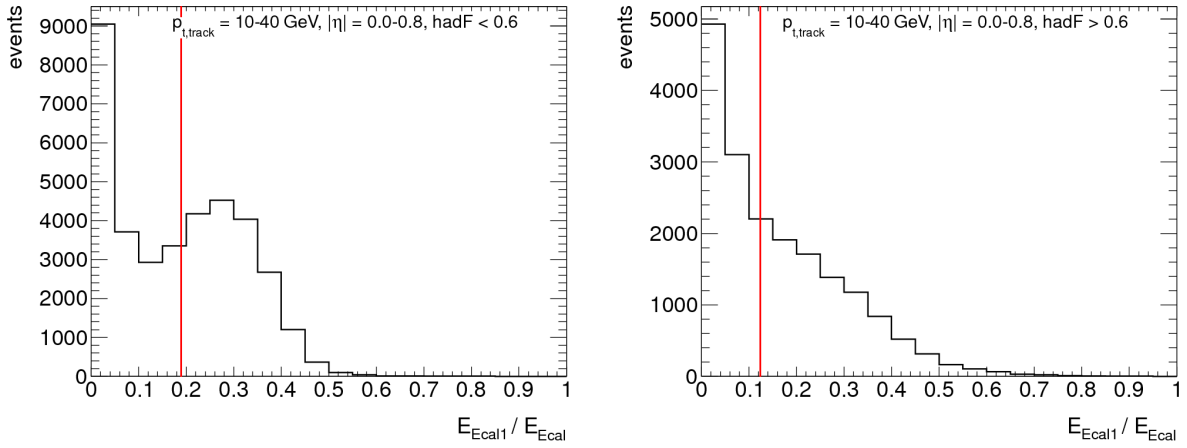

Figure 4.6: Fluctuation of the fraction of hadronic energy in Ecal1 over the total energy in the Ecal. The red line indicates the averaged lateral weight for the low hadronic fraction bin (left) and the high hadronic fraction bin (right).

4.2.3 Estimation of hadronic energy in each cell of a layer of the barrel electromagnetic calorimeter

Finally, the energy estimated in each layer is distributed to the cells within that layer. For this, averaged lateral shower shapes are determined for the three layers of the electromagnetic calorimeter separately. The same events and the same three-dimensional binning are used as for the calculation of the longitudinal weights. The distribution of the energy deposited in a layer is calculated in (lateral) bins of the distance in pseudorapidity $\Delta\eta$ and azimuthal angle $\Delta\phi$ of a cell to the extrapolated track position:

$$E_{\text{bin}} = \sum_{\text{pions}} \sum_{i \in I_{\text{bin}}} (c_i E_i). \tag{4.4}$$

Hereby I_{bin} is the set of cells in the $\Delta\eta - \Delta\phi$ bin. The binning is defined in table 4.5. Figure 4.7 shows the energy distributions in the central barrel part of Ecal2 for low hadronic fraction (hadF < 0.6) and two transverse momentum bins. The energy distributions obtained are normalized and then parameterized using the sum of three exponential functions:

$$\sum_{i=1}^{3} a_i \cdot \exp\left(-\sqrt{b_i \Delta\eta^2 + c_i \Delta\phi^2}\right), \tag{4.5}$$

a_i, b_i, c_i are parameters. The lateral binning is chosen in order to minimize the combined effect of two mechanisms that artificially widen the energy distribution:

- Energy is always assigned to the center of a cell. If the cell is too large this is usually further away from the track than the energy deposition. This is especially relevant for pions that hit a cell close to its edge and deposit part of their energy in the neighboring cell. The energy is assigned to the center of the neighboring cell, i.e. to more than half the cell width away from the track.

- To reduce this effect, the bin width can be set to a smaller value than the cell size. Then, however, there are always events, in which no cell is within the middle bin. These enlarge the energy fraction outside the middle bin, which widens the fit function that is extracted.

Layer	$\Delta\eta$	$\Delta\phi$
Presampler	0.0125	0.05
Ecal1	0.025/8	0.05
Ecal2	0.025	0.025

Table 4.5: Lateral binning for the calculation of the lateral hadronic shower shapes for barrel candidates.

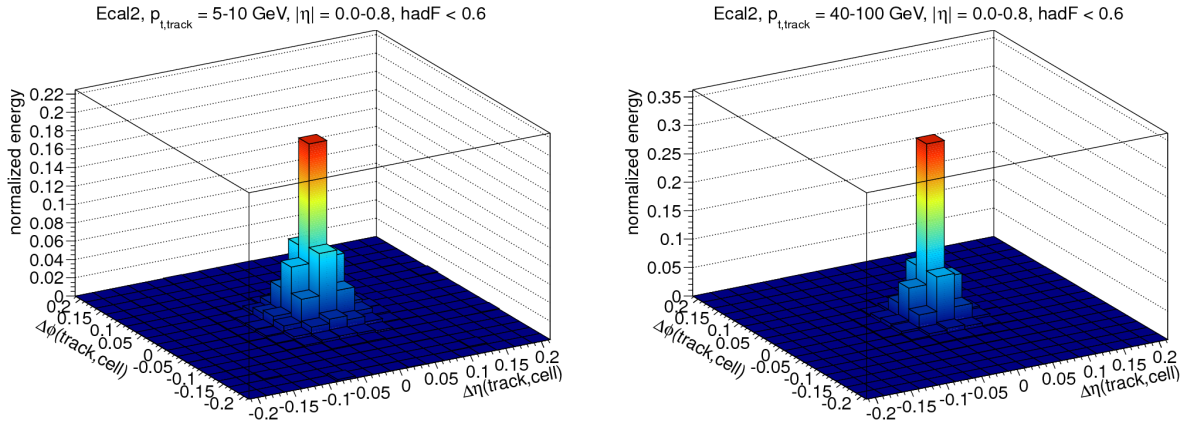

Figure 4.7: Lateral energy distribution of pion showers in Ecal2. The distributions in the central barrel and for the low hadronic fraction bin are shown for low (left) and high (right) transverse momenta. Hadronic shapes are narrower for larger transverse momenta. Both distributions are slightly wider in $\Delta\phi$-direction than in $\Delta\eta$-direction, which is an effect by the magnetic field.

Two-dimensional fits in the parameters a_i, b_i, c_i are performed to extract the lateral shower shapes in Ecal2. Examples are shown in figure 4.8. Typical values of χ^2/ndf are $1-5$, while values can be even larger for bins with high statistics (like those shown). However, as the statistical fluctuations of hadronic showers on a candidate by candidate basis are much larger than the error of the parameterization, a more precise parameterization would only slightly improve the accuracy on a candidate by candidate bases. In general, showers with larger hadronic fractions are narrower in the electromagnetic calorimeter, because they start later. Shower profiles measured in the extended barrel are wider than those measured in the central barrel, since particles in the extended barrel traverse the electromagnetic calorimeter at a shallower angle and travel a longer distance through each layer.

The precision of the energy distributions obtained for the presampler and the strip layer suffers from the large cell sizes in $\Delta\phi$[3]. As discussed, a large cell width causes an artificial widening of the lateral shapes, in this case in $\Delta\phi$. For this reason, a two-dimensional fit is not the best choice to extract the shower shapes for the presampler and Ecal1. In both layers, shower shapes are expected to be very similar in $\Delta\eta$ and $\Delta\phi$. The difference caused by the magnetic field is significantly smaller than in Ecal2, since the presampler and Ecal1 are much thinner. Therefore the lateral shapes for these layers are determined with a one-dimensional fit in $\Delta\eta$, taking advantage of the much better spatial resolution. The fit function is then extrapolated to the rest of the η-ϕ-plane by assuming radial symmetry, i.e. setting $c_i = b_i$. The lateral energy distributions in η are well described by the fit functions for the presampler and Ecal1 (figure 4.9). As the cells are very wide in ϕ-projection, in most cases all energy is deposited in one row of cells. The bin size for the ϕ-projections is half of the cell width, thus the data points only show approximately half of the energy in the central bin and most of the rest in the neighboring bins. In

[3] The cell sizes in the presampler and Ecal1 are $\delta\eta \times \delta\phi = 0.025 \times 0.1$ and $\delta\eta \times \delta\phi = 0.025/8 \times 0.1$, respectively.

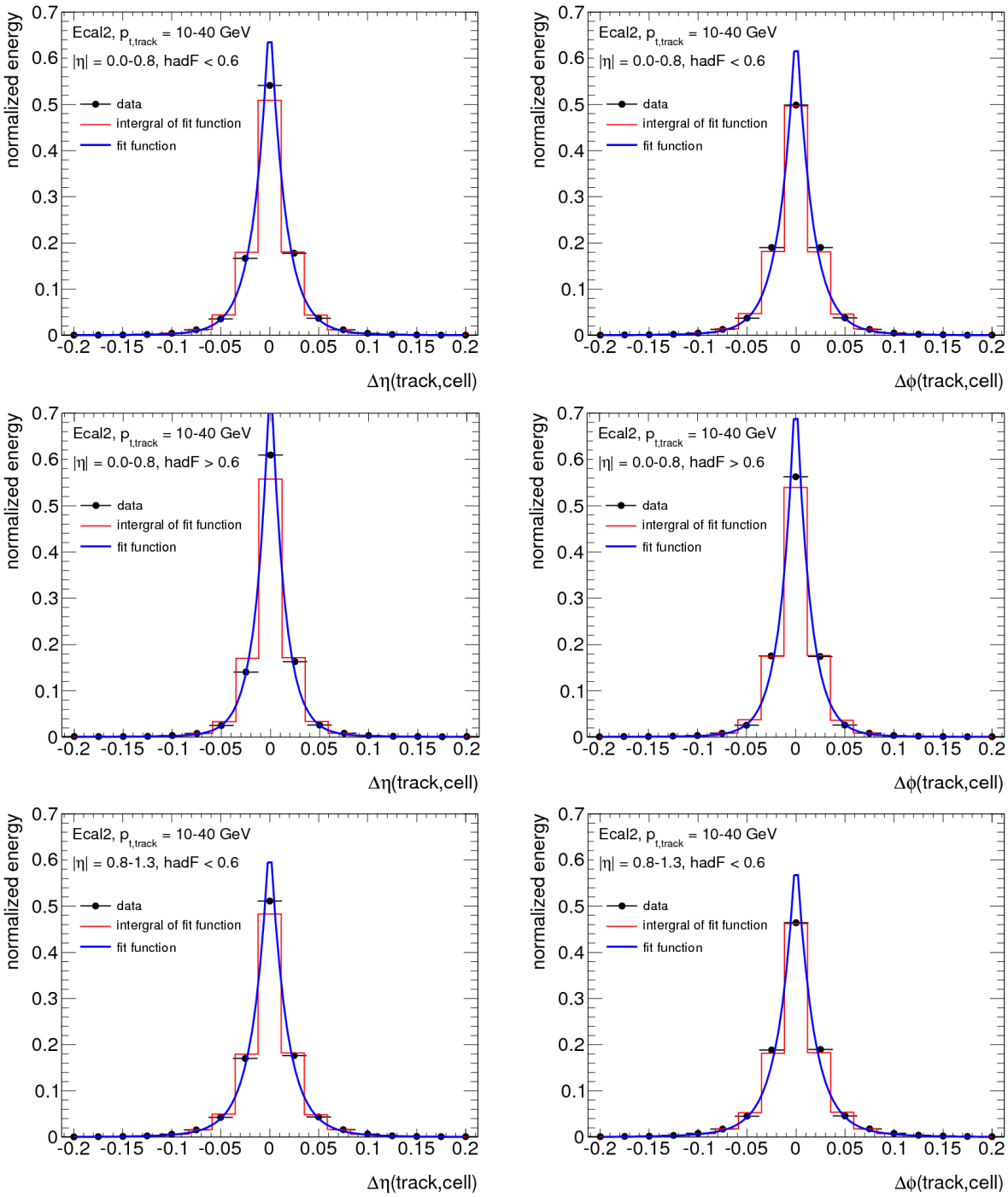

Figure 4.8: $\Delta\eta$ and $\Delta\phi$ projections of lateral hadronic shower shapes in Ecal2. The energy distribution, the fit function and the integral of the fit function are shown for the two hadF-bins and the two barrel $|\eta|$-bins in the transverse momentum range of 10 – 40 GeV.

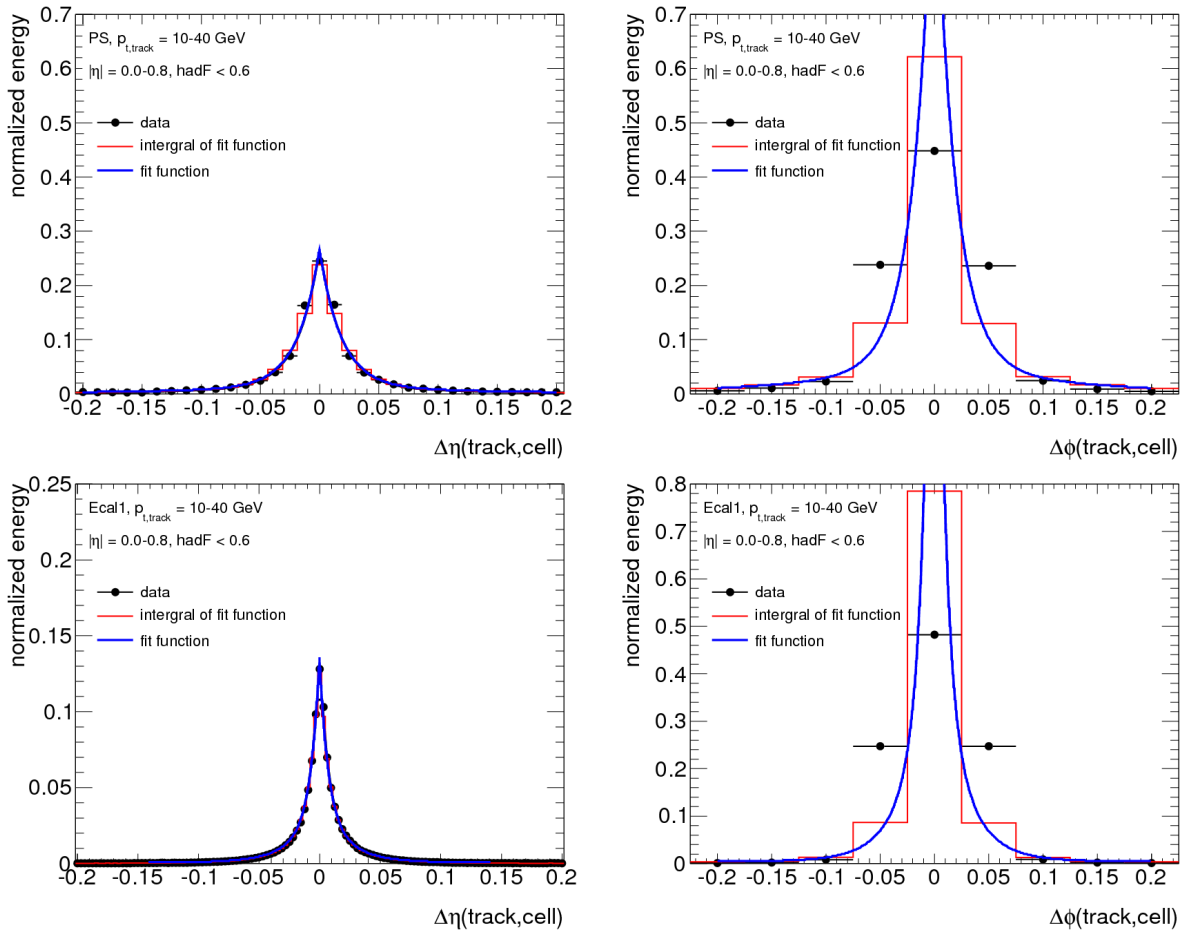

Figure 4.9: $\Delta\eta$ and $\Delta\phi$ projections of lateral hadronic shower shapes in the presampler and the strip layer. The energy distribution, the fit function and the integral of the fit function are shown for showers of hadrons with transverse momenta of 10 – 40 GeV. The fit is only performed in $\Delta\eta$. For the plots in $\Delta\phi$ the fit function is scaled by the fraction of the bin width, so it can be compared with the data points. The apparent disagreement of the fit functions and the energy distributions measured in ϕ-projection is a binning effect (cf. text).

both cases the shower shapes would be widened, if the ϕ-projections were taken into account for the fit.

4.2.4 Subtraction of hadronic energy on cell level

To calculate the amount of energy that is to be subtracted in each cell of the electromagnetic calorimeter, firstly the total amount of energy to subtract is calculated using equation 4.2. It is then distributed to the layers of the electromagnetic calorimeter according to the longitudinal weights

$$E_{\ell}^{\text{est}} \equiv w_{\ell} \cdot E_{\text{Ecal}}^{\text{est}}. \tag{4.6}$$

Finally the energy estimated in each layer is distributed to the cells by integrating the lateral hadronic shower shapes over the cell area:

$$E_{\text{cell}}^{\text{est}} \equiv w_{\ell} \cdot E_{\text{Ecal}}^{\text{est}} \int_{\text{cell area}} \left(\sum_{\text{i}=1}^{3} a_{\text{i}} \cdot \exp\left(-\sqrt{b_{\text{i}}\Delta\eta^2 + c_{\text{i}}\Delta\phi^2} \right) \right) \mathrm{d}\Delta\eta \, \mathrm{d}\Delta\phi. \tag{4.7}$$

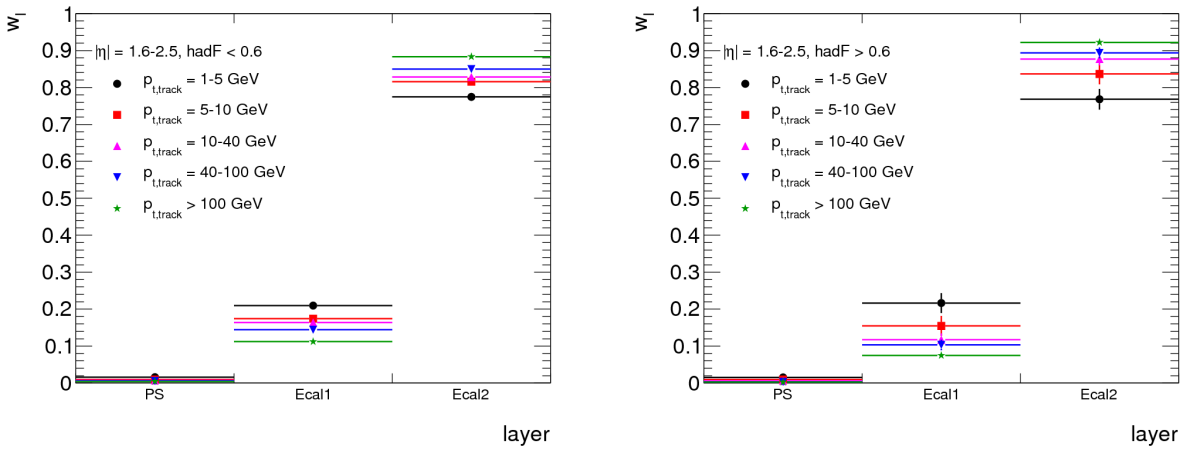

Figure 4.10: Longitudinal weights for hadronic shower subtraction in the electromagnetic end-cap calorimeter. The weights are shown the two hadronic fraction bins (left/right) and all transverse momentum bins (colors). The statistical errors on the longitudinal weights are shown. The errors are larger for the high hadronic fraction bin and for the low transverse momentum bins, because there is less total energy deposited in the electromagnetic calorimeter and thus less statistics available.

4.2.5 Preliminary extension to the electromagnetic end-cap calorimeter and the transition region

As mentioned before, the algorithm has been developed on candidates that are fully contained in the barrel part of the electromagnetic calorimeter. This section describes the preliminary extension to the end-cap and transition regions between the barrel and end-cap electromagnetic calorimeter, which enables the algorithm to run on all 1-prong candidates.

The calculation of the longitudinal weights for candidates in the end-cap region ($1.6 < |\eta| < 2.5$) is analogous to the calculation for barrel candidates. The qualitative dependence of the longitudinal weights on the binning variables is similar as in the barrel (figure 4.10). The weights for the presampler are however much smaller than in the barrel, since it stops at $|\eta| = 1.8$. Due to lack of statistics, reliable lateral shower shapes for the end-cap presampler cannot be calculated in all three-dimensional bins. As a fix the energy that was meant to be subtracted in the presampler is subtracted in Ecal1 and Ecal2 instead:

$$w_{\mathrm{PS}}^{\mathrm{fix}} \equiv 0 \qquad w_{\mathrm{Ecal1}}^{\mathrm{fix}} \equiv w_{\mathrm{Ecal1}} \frac{1}{1 - w_{\mathrm{PS}}} \qquad w_{\mathrm{Ecal2}}^{\mathrm{fix}} \equiv w_{\mathrm{Ecal2}} \frac{1}{1 - w_{\mathrm{PS}}}.$$

The calculation of the lateral shower shapes for Ecal1 and Ecal2 in the end-cap region is as described in section 4.2.3. The energy to subtract in each cell is calculated with equation 4.7 after replacing w_ℓ by w_ℓ^{fix}.

In the transition region the electromagnetic barrel and end-cap calorimeters overlap in the pseudo-rapidity regions $1.375 < |\eta| < 1.475$. Particles first pass the barrel calorimeter. As the thickness of the barrel calorimeter decreases with $|\eta|$ (figure A.1) the fraction of energy deposited in the barrel calorimeter decreases. For the subtraction procedure it must be decided how much energy to subtract in the barrel and end-cap layers, respectively. As the amount of material in the electromagnetic barrel calorimeter decreases approximately linearly with $|\eta|$, a linear interpolation factor has been introduced

in equation 4.7:

$$E_{\text{cell}}^{\text{est}} = w_{\text{int}} \cdot w_{\ell}^{(\text{fix})} \cdot E_{\text{Ecal}}^{\text{est}} \int_{\text{cell area}} \left(\sum_{\text{i}=1}^{3} a_{\text{i}} \cdot \exp\left(- \sqrt{b_{\text{i}} \Delta\eta^2 + c_{\text{i}} \Delta\phi^2} \right) \right) \mathrm{d}\Delta\eta \, \mathrm{d}\Delta\phi \tag{4.8}$$

$$\text{with} \quad w_{\text{int}} = \begin{cases} 1 - 10\,(|\eta_{\text{cell}}| - 1.375), & \text{if cell is in barrel and } |\eta| > 1.375 \\ 1 - 10\,(1.475 - |\eta_{\text{cell}}|), & \text{if cell is in end-cap and } |\eta| < 1.375 \\ 1, & \text{otherwise.} \end{cases}$$

Within the transition region the longitudinal weights and lateral shower shapes obtained for the extended barrel and the end-cap are used for barrel- and end-cap cells, respectively.

4.2.6 Clustering of the remaining energy

After removing the charged hadron subshower, the cells within the electromagnetic calorimeter are re-clustered with the ATLAS Topoclustering algorithm (section 2.5.5). The cluster threshold applied is $|E_{\text{t, cluster}}| > 500\,\text{MeV}$ (default). Only clusters with positive energy are considered as π^0 candidates, clusters with negative energy can however be used to test the subtraction method. Within the re-clustering process the so called 'CaloClusterMomentsMaker' calculates cluster moments, which are later used for the selection of neutral pion clusters. The cluster position is calculated with respect to the reconstructed tau vertex (usually the primary vertex of the event) in order to improve the spatial resolution.

4.2.7 Performance of the hadronic subshower removal

The performance of the hadronic subshower removal is tested in $\tau^{\pm} \rightarrow \text{h}^{\pm}\nu_{\tau}$ decays from the non pile up sample. This sample of single charged hadrons is statistically independent of the sample of single charged pions used to obtain the longitudinal weights and the lateral shower shapes for the subtraction. Ideally there would be no energy left after subtraction for these tau candidates. Taus whose track has a transverse momentum of less than 10 GeV must be excluded from the test, because only jets with a transverse momentum of more than 10 GeV are seeds for tau candidates. This means that for all $\tau^{\pm} \rightarrow \text{h}^{\pm}\nu_{\tau}$ decays, in which the charged hadron has a transverse momentum smaller than 10 GeV and that are considered as a tau candidate, the energy in the calorimeter is overestimated. The energy left after the subtraction is compared to the energy that has been in the electromagnetic calorimeter before the subtraction. Only energy in cells within clusters is counted, i.e. the energy in the cells in the clusters before subtraction is compared to the energy in the cells in the clusters found during re-clustering.

Figure 4.11 shows the average fraction of the energy of the charged hadrons in the different layers of the Ecal before and after subtraction. The fraction of energy in the layers is reduced to about 20–30 % in the presampler, to about 6–9 % in Ecal1 and to about −3 – 5 % in Ecal2. In total there is 1–4 % of the total energy left in the Ecal. This is possibly a clustering effect: Energy that is subtracted in cells that are not in clusters are missing in the energy balance. An additional contribution comes from particles that do not come from the tau (especially in the presampler).

Figures 4.12 – 4.14 show the averaged lateral energy distribution before and after subtraction in the different Ecal layers. In all layers there is on average some energy remaining close to the track, which indicates that the assumed lateral shapes for the subtraction are slightly too wide. The effect is most pronounced in Ecal1, where the estimation of the energy in each cell is hardest due to its fine granularity. However clusters that remain because of this inaccuracy of the lateral shower shapes are much narrower than clusters from particles and can thus be distinguished. The subtraction method works best in Ecal2. This is the most important layer, as it contains most of the energy deposited in the electromagnetic

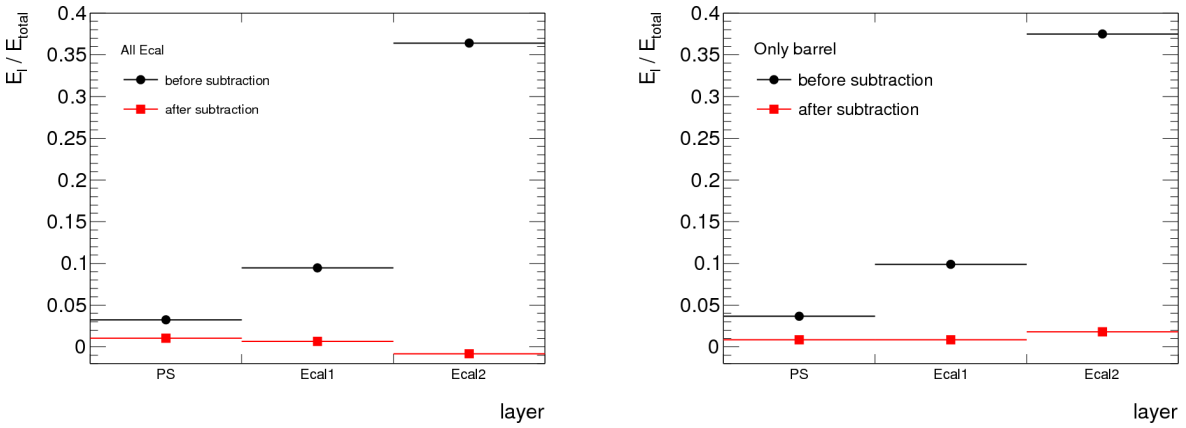

Figure 4.11: Comparison of the average energy in the layers of the electromagnetic calorimeter before and after subtraction. The energy is decided by the total energy of the charged hadrons. The comparison is shown for the candidates (left) and candidates in the barrel region (right).

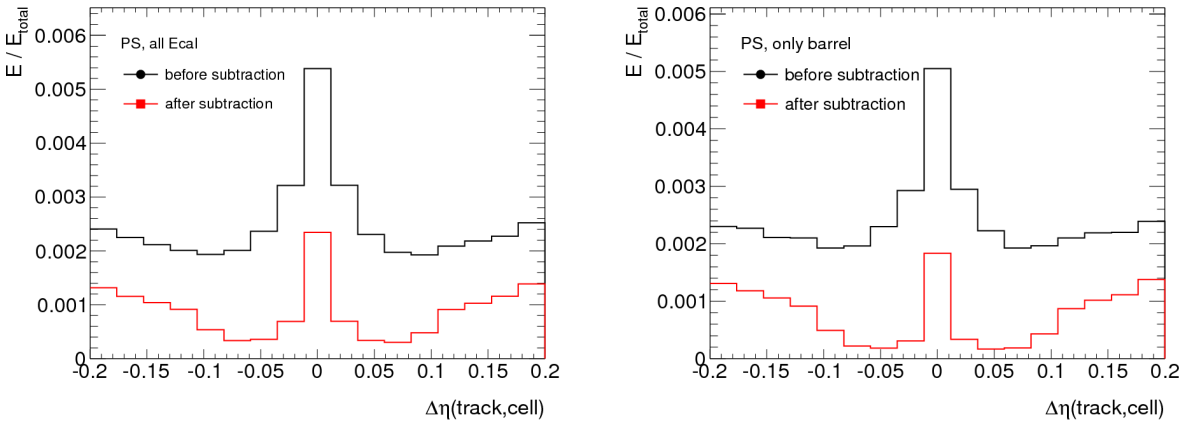

Figure 4.12: Comparison of the average lateral energy distribution in the presampler before and after subtraction. The bin width corresponds to the width of one cell. The energy is decided by the total energy of the charged hadrons. As no energy is subtracted in the end-cap presampler a larger fraction of energy is remaining in the combined Ecal (left) than in the barrel region only (right).

calorimeter. The observed problems with the parameterization of the lateral shower shapes will be further investigated and the parameterization adjusted in the future.

4.3 Identification of neutral pion clusters

The second part of the algorithm involves the identification of neutral pions from the set of clusters remaining after subtraction. The clusters can be classified as follows:

- clusters containing both photons resulting from a π^0 decay. Most neutral pions produce this kind of clusters,
- clusters caused by one of the two photons from a low-energy π^0 decay,
- clusters containing photons produced in two (or more) neutral pion decays,

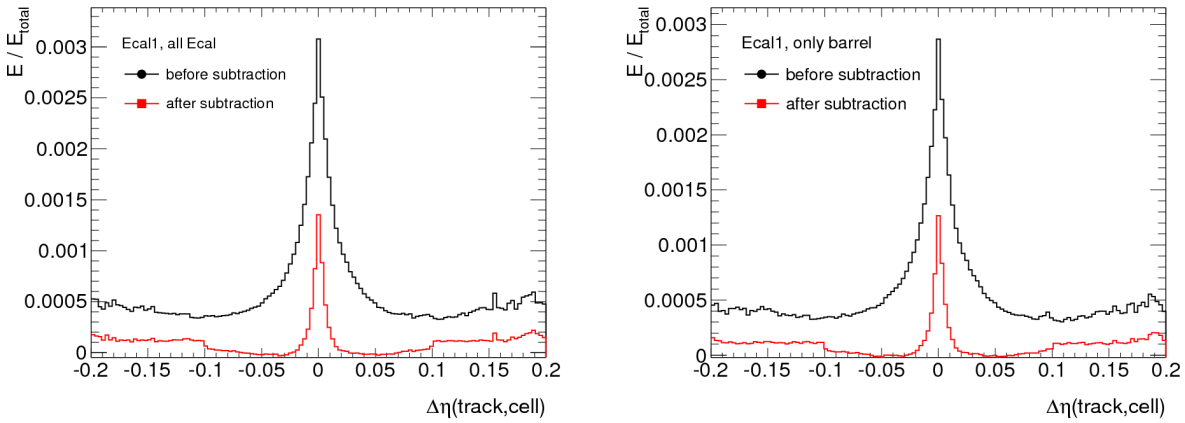

Figure 4.13: Comparison of the average lateral energy distribution in Ecal1 before and after subtraction. The bin width corresponds to the width of one cell in the Ecal1 layer of the barrel calorimeter. The energy is divided by the total energy of the charged hadrons. The comparison is shown for all candidates (left) and candidates that are contained in the barrel region (right).

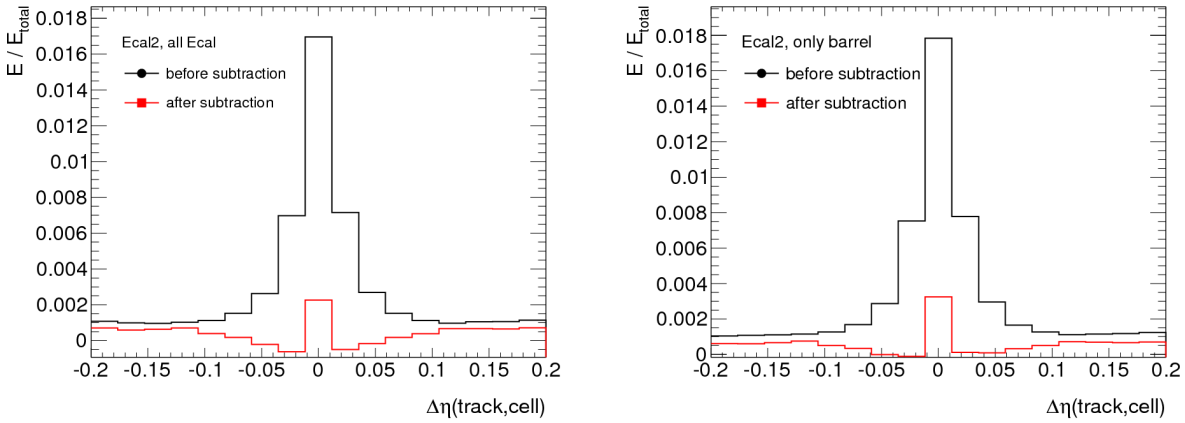

Figure 4.14: Comparison of the average lateral energy distribution in Ecal2 before and after subtraction. The bin width corresponds to the width of one cell. The energy is decided by the total energy of the charged hadrons. The comparison is shown for all candidates (left) and candidates in the barrel region (right).

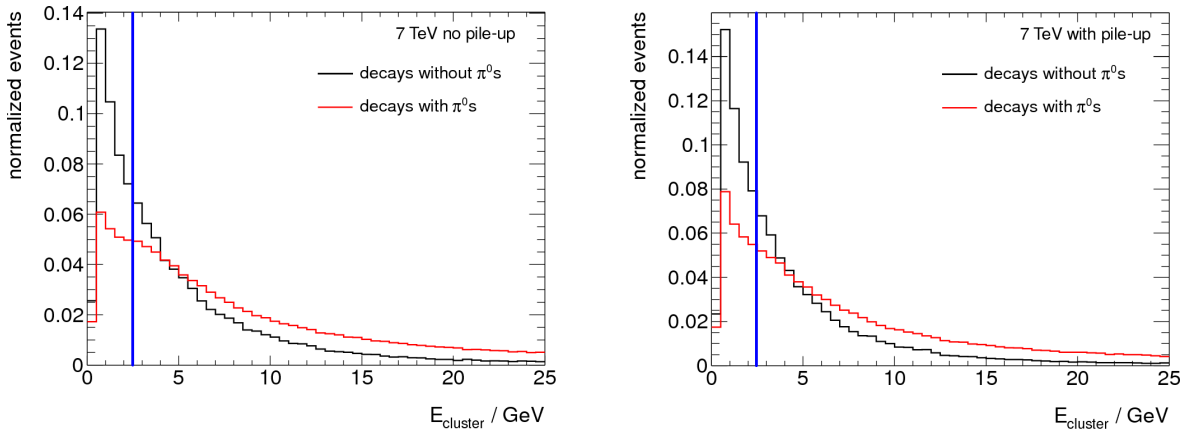

Figure 4.15: Energy distribution of clusters in decays with and without neutral pions after subtraction. The distributions are normalized to unity. In decays with no neutral pion there are only background clusters. The energy distribution of these clusters peaks at threshold, the peak is slightly more pronounced in presence of pile up (right). In decays with neutral pions there are both signal and background clusters, the signal clusters shift the energy distribution towards higher values. The blue lines indicate the preselection threshold of 2.5 GeV.

- clusters caused by remnants of imperfect energy subtraction,
- clusters caused by particles other than from the tau decay (e.g. pile up),
- clusters caused by noise.

For this study the first three types of clusters are assigned to one common signal category. Ideas on how they can be fully separated from each other in the future are presented in section 6.

4.3.1 Preselection

The energy distribution of the neutral pion candidates both in decays with and without neutral pions is shown in figure 4.15. A significant fraction of background clusters are found to have low energies. Therefore an energy threshold of 2.5 GeV is applied as a preselection criteria. The preselection not only reduces the background but also improves robustness against pile up, because most clusters caused by pile up have low energies. It has been checked that the performance of the algorithm is only weakly dependent on the exact threshold value if it is varied within a few hundred MeV. Clusters that pass the preselection are referred to as π^0 candidates. In figure 4.16 the dependence of the number of π^0 candidates with an energy above 2.5 GeV on the number of true neutral pions before and after subtraction is shown. The shower subtraction significantly reduces the number of background clusters. A correlation between the number of candidates and true π^0s is already visible. Further identification is however required as e.g. about 40 % of decays without neutral pions contain at least one neutral pion candidate.

4.3.2 Truth matching of neutral pion candidates

To obtain information that can be used for further identification, samples of real and fake neutral pion candidates are needed. They are obtained by geometrically matching neutral pion candidates to true neutral pions in the simulated samples. The matching classification as signal or background cluster proceeds as follows:

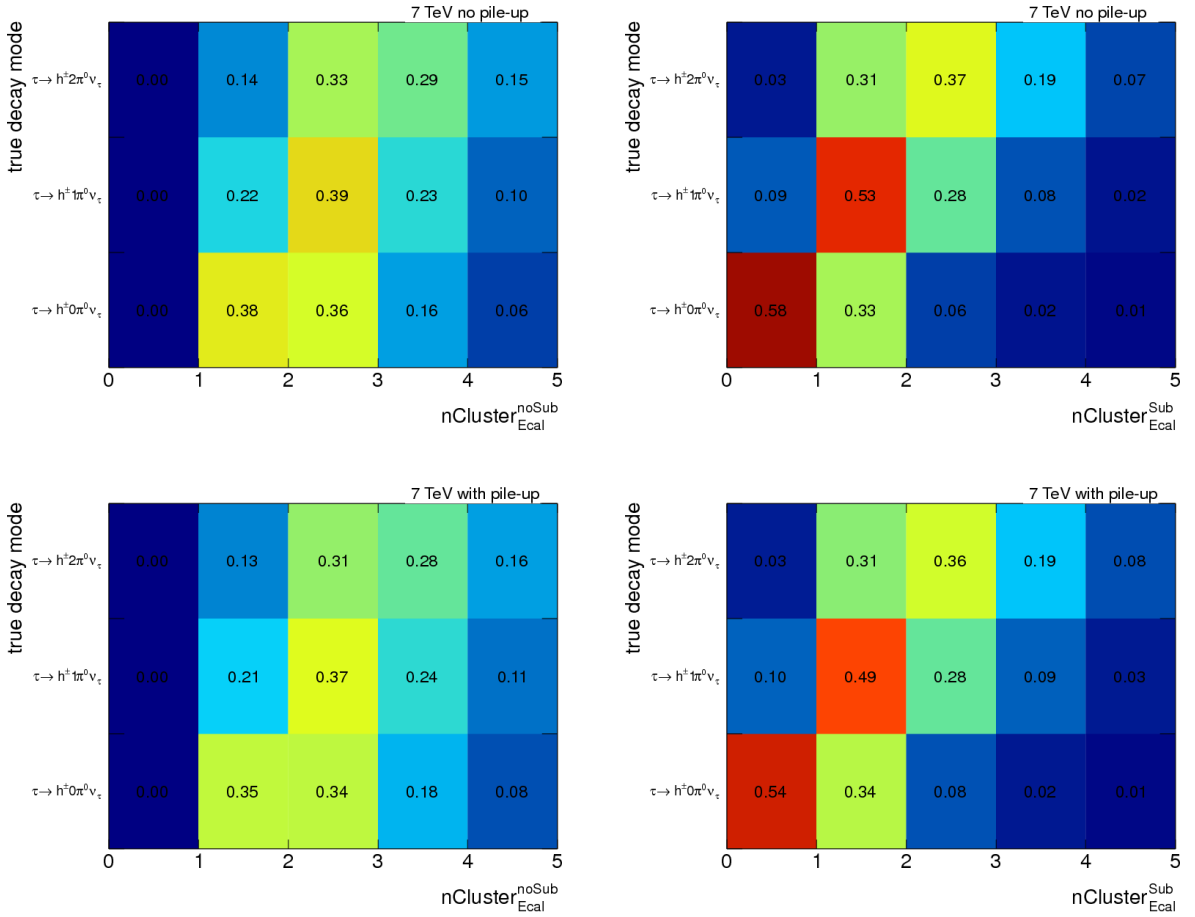

Figure 4.16: Number of neutral pion candidates (horizontal axis) vs. the number of true neutral pions (vertical axis). The entries for each decay mode are normalized to unity. On the left the number $\mathrm{nCluster}_{\mathrm{Ecal}}^{\mathrm{noSub}}$ of clusters with an energy of $> 2.5\,\mathrm{GeV}$ before subtraction is shown, on the right the number $\mathrm{nCluster}_{\mathrm{Ecal}}^{\mathrm{Sub}}$ of preselected clusters after subtraction. The difference between the non-pile up sample (top) and the 7 TeV sample with pile up (bottom) is relatively small.

Signal: The cluster closest to each true π^0 is classified as signal if $\Delta R(\text{cluster, true } \pi^0) < 0.1$,

Background: Clusters that have not been selected as signal clusters.

4.3.3 Discriminating variables

The identification of signal clusters is based on the following differences of neutral pion clusters and background clusters:

- Signal clusters have large energy densities and core fractions
- Signal clusters have more cells with positive energy than background clusters, because most signal clusters contain both photons produced in a π^0 decay. The photons hit the calorimeter at slightly different positions.
- The asymmetry of the cluster with respect to the extrapolated track position provides discrimination against remnants from a imperfect subtraction.
- Photons are not deflected by the magnetic field. Therefore the angle between the shower axis and the vector from the primary vertex to the shower center is small.
- It has been found that there are more background clusters in the end-cap and transition regions than in the barrel region, i.e. at higher pseudorapidities. Also some of the other variables are correlated to η_{cluster}. For example the granularity of Ecal1 is much smaller in the end-cap, which causes a negative correlation of η_{cluster} to the number of cells with positive energy in Ecal1.

Additional separation could be provided by kinematic variables or e.g. the invariant mass of the neutral pion candidate and the track. They are not used by this algorithm so that they can still be used for further analysis (e.g. tau identification or polarization studies). A total of twenty variables are used that are sensitive to the differences of signal and background candidates. They are listed in table 4.6 including a brief description. Hereby a cluster moment of degree n over a variable x is defined as

$$\langle x^n \rangle \equiv \frac{1}{E_{\text{norm}}} \sum_{\text{i}|E_\text{i}>0} E_\text{i} x_\text{i}^n, \qquad E_{\text{norm}} = \sum_{\text{i}|E_\text{i}>0} E_\text{i}$$

and the asymmetry with respect to the extrapolated track position is defined as

$$\text{AsymmetryWRTTrack} \equiv \left| \frac{\left(\sum_{\eta_\text{i}>\eta_\text{track}} E_\text{i} - \sum_{\eta_\text{i}<\eta_\text{track}} E_\text{i} \right) \cdot \left(\sum_{\phi_\text{i}>\phi_\text{track}} E_\text{i} - \sum_{\phi_\text{i}<\phi_\text{track}} E_\text{i} \right)}{\sum E_\text{i}} \right|,$$

using the cells within Ecal1 that have positive energy. A more detailed description of the other variables is given in [17].

The distributions of all the discriminating variables in the non pile up sample are shown in figures 4.17–4.20. For variables with symmetric distributions the absolute value of these is used. The distribution in λ_{center} has a long tail. This has turned out to be problematic for multivariate analysis, so the distribution is truncated at 1000. The linear correlation coefficients of the discriminating variables for signal clusters can be found in figure 4.21. Some of the variables are highly correlated. They have been kept so that the variables that show best agreement between simulation and data can be chosen, when the algorithm is tested with collision data.

Symbol	Description
ETA_CLUSTER	Pseudorapidity of the cluster
SECOND_R	Second moment in distance to the shower axis*
SECOND_LAMBDA	Second moment in distance to the shower center along the shower axis*
Abs_DELTA_PHI	ϕ difference of the shower axis and the vector pointing from the Reconstructed primary vertex (PW) to the shower center*
Abs_DELTA_THETA	θ difference of the shower axis and the vector pointing from the PW to the shower center*
CENTER_LAMBDA_helped	Distance of the shower center from the calorimeter front face measured along the shower axis*
LATERAL	Normalized second lateral moment*
LONGITUDINAL	Normalized second longitudinal moment*
ENG_FRAC_EM	Fraction of energy in EM calorimeter accordion* (in our case: Ecal1 and Ecal2)
ENG_FRAC_MAX	Energy fraction in the most energetic cell*
ENG_FRAC_CORE	Sum of the energy fractions in the most energetic cells per sampling*
$\log\left\langle (E/V)^2 \right\rangle$	Logarithm of the second moment in energy density*
$\frac{E_{\text{core}}}{E_{\text{Ecal1}}}$	Energy in three innermost Ecal1 cells normalized to total energy in Ecal1
AsymmetryWRTTrack	Asymmetry of energy distribution in Ecal1 with respect to the Extrapolated track position
NPosCells_EM1	Number of cells with positive energy in Ecal1
NPosCells_EM2	Number of cells with positive energy in Ecal2
$\lvert\langle\eta\rangle\rvert_{\text{Ecal1}}$	First moment in pseudorapidity in Ecal1
$\lvert\langle\eta\rangle\rvert_{\text{Ecal2}}$	First moment in pseudorapidity in Ecal2
$\left\langle\eta^2\right\rangle_{\text{Ecal1}}$	Second moment in pseudorapidity in Ecal1
$\left\langle\eta^2\right\rangle_{\text{Ecal2}}$	Second moment in pseudorapidity in Ecal2

Table 4.6: Variables used to identify neutral pion clusters. The formulas of the variables marked with a star are defined in [19].

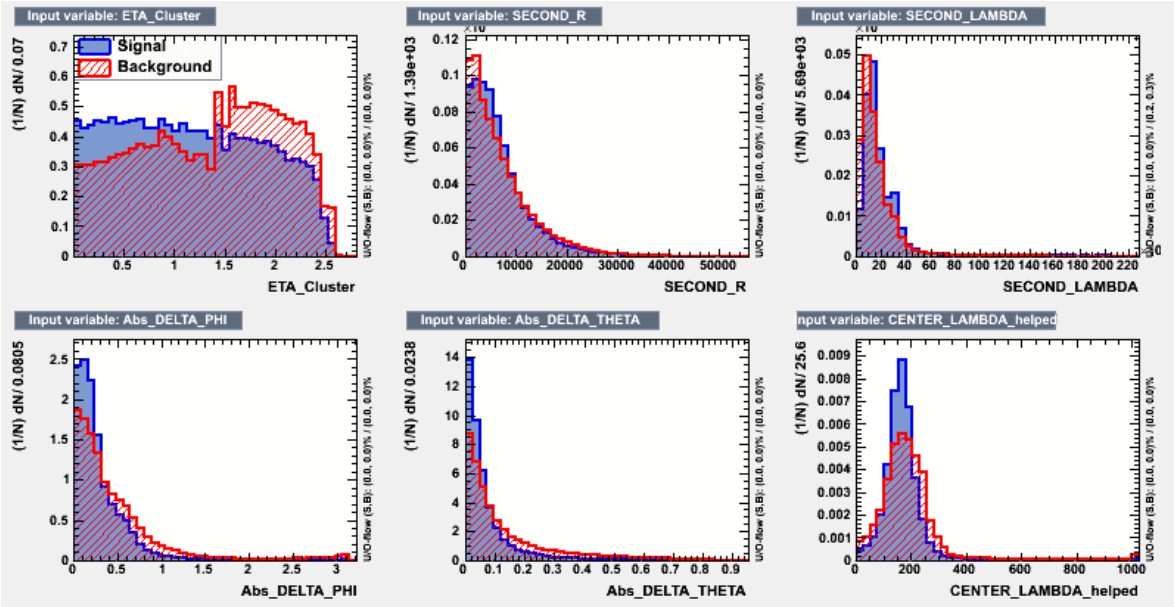

Figure 4.17: Variables used for identification of neutral pion clusters (see table 4.6 for explanation).

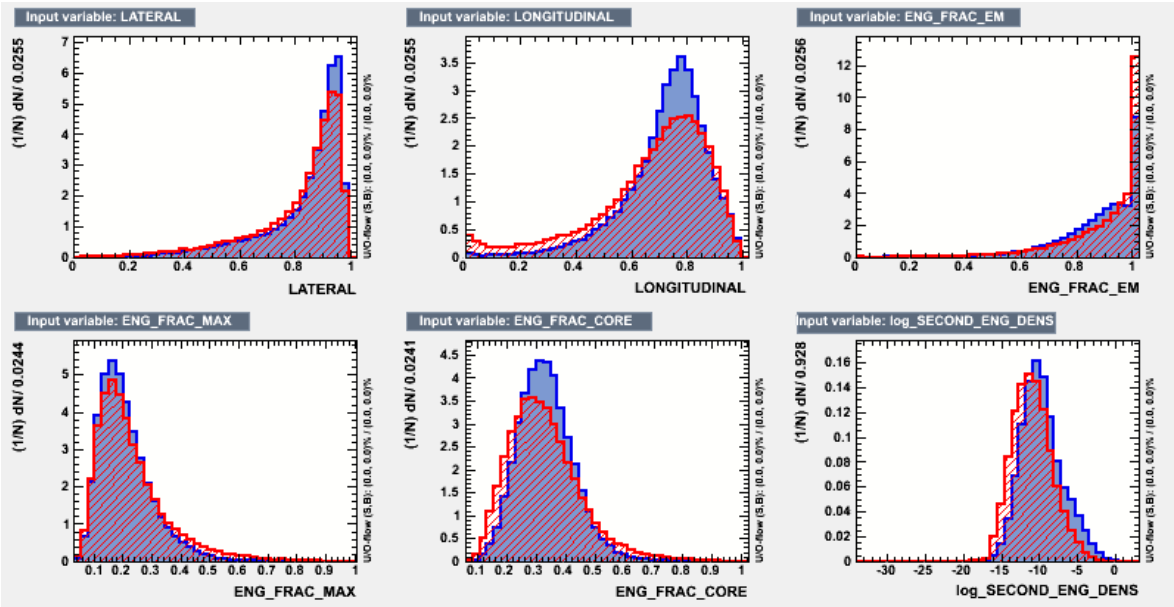

Figure 4.18: Variables used for identification of neutral pion clusters (see table 4.6 for explanation).

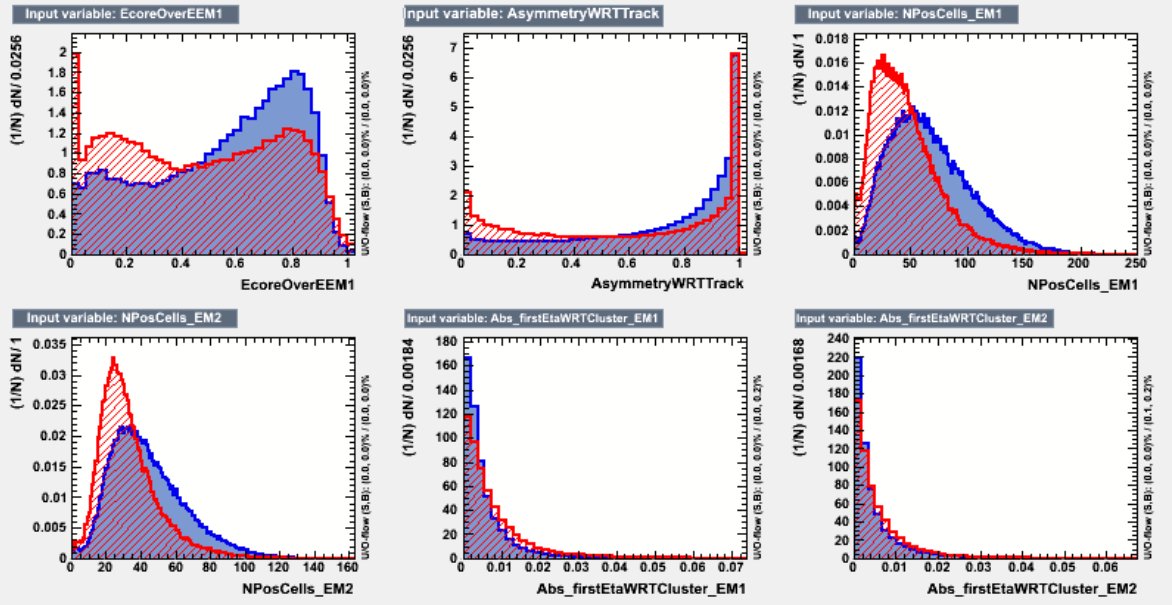

Figure 4.19: Variables used for identification of neutral pion clusters (see table 4.6 for explanation).

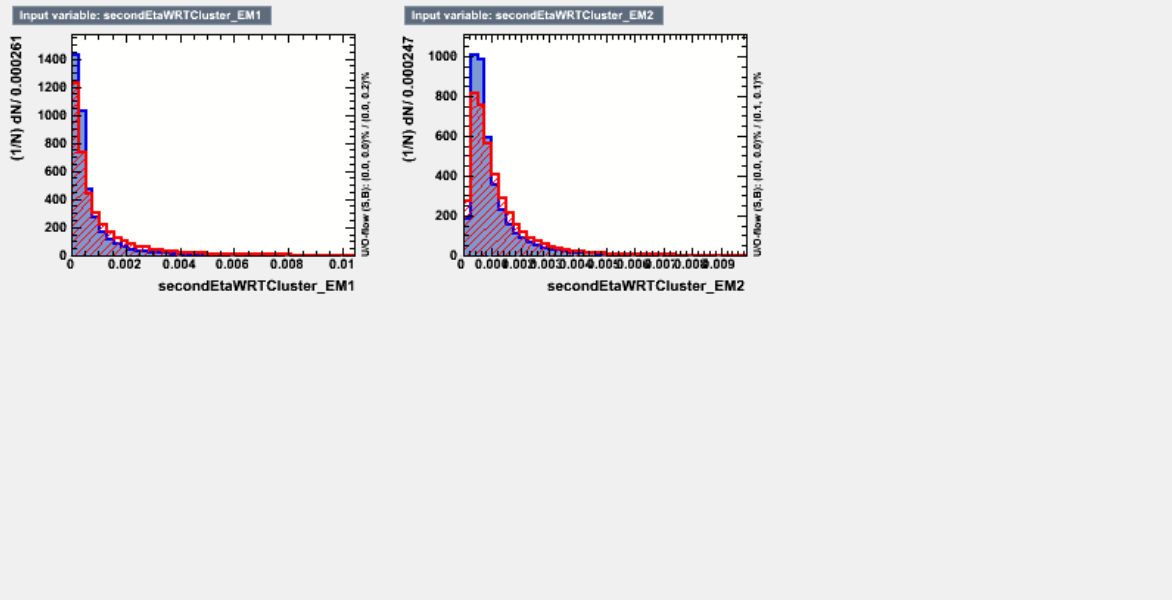

Figure 4.20: Variables used for identification of neutral pion clusters (see table 4.6 for explanation).

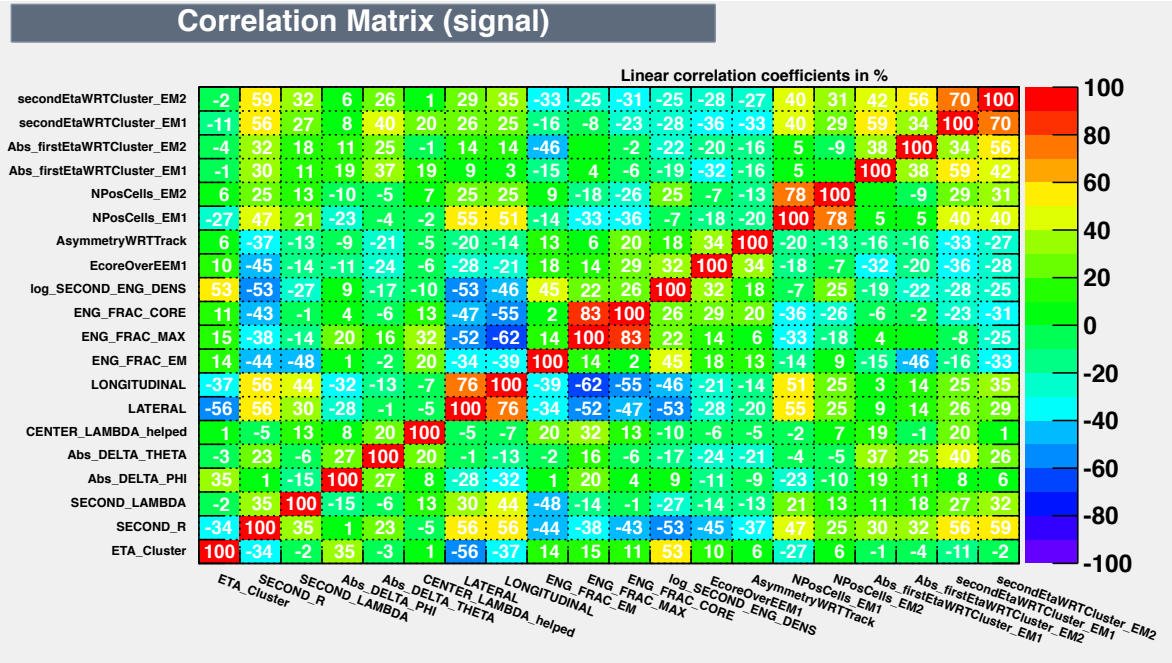

Figure 4.21: Linear correlation coefficients of the variables used for identification of neutral pion clusters.

4.3.4 Boosted Decision Trees

To get the best discrimination of neutral pion clusters and background, the discriminating variables are combined to one more powerful discriminant. For this study the Boosted Decision Tree (BDT) method has been chosen, because it shows a good performance for comparably large numbers of correlated input variables. The method is provided by the 'Toolkit for Multivariate Data Analysis with ROOT' (TMVA) [20]. It proceeds as follows: The method is trained with an input of signal and background samples. The training starts by applying a one dimensional cut on the variable that provides best discrimination of the signal- and background samples. This is subsequently repeated in both the failed and passed sub-samples using the next most powerful variable until the number of events in a certain sub-sample has reached a minimum number of objects. Objects are classified as 'signal' or 'background' dependent on whether they are in a signal or background like sub-sample. The result of this process defines one 'tree' (figure 4.22). The process is then repeated weighting wrongly classified candidates higher ('boosting them'). The procedure stops when a predefined number of trees is trained. After training, the Boosted Decision Trees can classify new objects: For each tree it is tested whether the object is in a signal or background sub-sample. A likelihood estimator is calculated for the object being signal or background. This estimator is the BDT output variable. A larger number of trees or a smaller number of objects required in each bin and therefore a larger number of subsequent cuts, obviously improves the performance of the BDTs on the training sample. At some point statistical fluctuations in the training sample begin to affect the training. This so called 'over-training' degrades the performance of the BDTs (on other samples) and must be avoided.

As above mentioned samples of signal and background clusters are required to train the BDTs. To prevent a bias of the results, the sample used for training must be excluded from the tests of the algorithm. To have more realistic results the algorithm should be tested with the samples including pile up. Due to their relatively small size, the 7 TeV sample with pile up cannot be used for training *and* testing. However, the BDTs trained on the non pile up sample can be used on the samples including pile

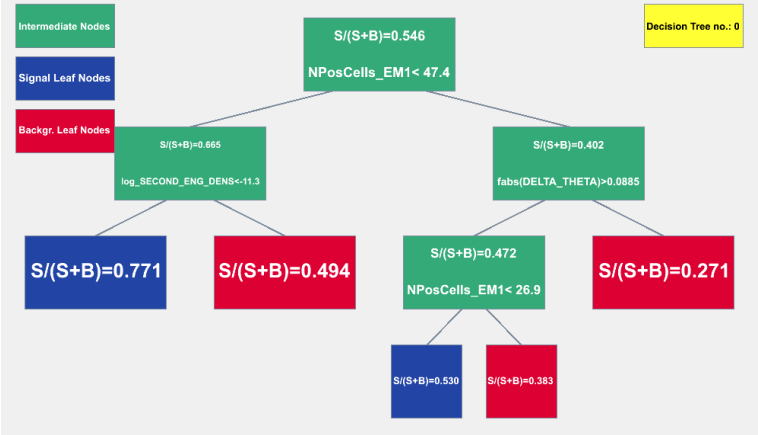

Figure 4.22: Example of a Boosted Decision Tree.

Variable	Value
Number of trees	400
Minimum number of objects in nodes	18000
Maximum depth of a tree	3

Table 4.7: Setup of the BDT method for training.

up. As a cross check another set of BDTs has been trained on the the first 250 000 taus in the 8 TeV sample and then used on the rest of the sample. The performance of the algorithm is similar for both sets of BDTs. For consistency in this thesis the BDTs trained on the non pile up sample are used for both the 7 TeV and the 8 TeV samples with pile up. Currently there is one set of BDTs used for the whole pseudorapidity range[4]. The setup of the BDT method (table 4.7) has been optimized such that the method provides the best separation power, while avoiding overtraining. The non pile up sample provides 340 000 neutral pion candidates for training, 190 000 of which are signal candidates. Fifty percent of the clusters are used for training. The BDT output distribution for the remaining candidates (test sample) and the training sample are compared to test for overtraining. The distributions show an adequate agreement within errors (figure 4.23) and no indication of overtraining is observed.

The next step is to find the cut value for the BDT output variable. For this study it is not the best choice to optimize for signal/ $\sqrt{\text{signal+background}}$, since the task is not to prove the presence of neutral pions in the sample but to provide the best results on a event-by-event basis. Therefore the cut value is optimized with respect to the counting performance. Hereby each selected cluster is counted as a reconstructed neutral pion, because most signal clusters contain both photons produced in a neutral pion decay. Efficiencies $\epsilon^{N_{\text{reco }\pi^0}}_{N_{\text{true }\pi^0}}$ are defined for which a tau decays with $N_{\text{true }\pi^0}$ true neutral pions are reconstructed with $N_{\text{reco }\pi^0}$ neutral pions. The efficiencies are defined with respect to the number of taus after the selection:

$$\epsilon^{N_{\text{reco }\pi^0}}_{N_{\text{true }\pi^0}} \equiv \frac{\text{number of taus with } N_{\text{true }\pi^0} \text{ true } \pi^0\text{s and} N_{\text{reco }\pi^0} \text{ reconstructed } \pi^0\text{s}}{\text{number of taus with } N_{\text{true }\pi^0} \text{ true } \pi^0\text{s after selection}} \tag{4.9}$$

[4] For the 7 TeV sample it has been tried to use separate BDTs for the barrel region and the rest of the detector. This however degraded the performance of the algorithm, since the number of events available is not sufficient for training. In the future this will be tried again on the 8 TeV sample, which has considerably more events.

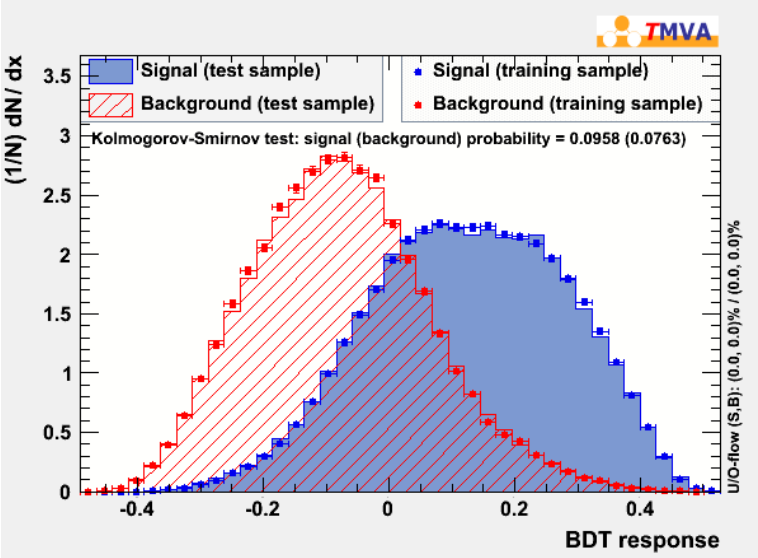

Figure 4.23: BDT output distribution. The training sample and the test sample agree adequately. This means that the BDTs are not overtrained.

As mentioned in chapter 4.1.2 reconstructed candidates with $\neq 1$ tracks or true charged hadrons have been excluded in the selection, because the algorithm currently works exclusively on 1-prong candidates. Therefore the number of true and reconstructed prongs is always one and omitted in the notation. For the optimization of the cut on the BDT output variable a figure of merit (FOM) for the counting performance must be defined. Several figures of merit can be defined and the algorithm can be optimized regarding different FOM dependent on the application for which it is used. The following FOMs are considered in this thesis:

- $\boldsymbol{N_{\text{correct}}}$: number of candidates, for which the number of neutral pions is counted correctly. This variable is maximized.
- $\sum |\boldsymbol{N_{\text{reco }\pi^0} - N_{\text{true }\pi^0}}|$: This FOM is similar to N_{correct}, however the entries, for which $N_{\text{true }\pi^0}$ and $N_{\text{reco }\pi^0}$ differ by more than one, are given a larger weight. This variable is minimized.
- $\boldsymbol{\epsilon_1^1}$, i.e. the efficiency for correctly reconstruct one π^0 in a decay. This efficiency is of special interest, as in approximately 50 % of all 1-prong decays there is exactly one neutral pion. This variable is maximized.

The cut values on the BDT output variable are separately optimized for the three FOMs by using the first 50 000 taus of the 7 TeV and the first 200 000 taus of the 8 TeV samples with pile up. The remaining taus are used to test the algorithm. The BDT cuts are hereby also separately optimized for π^0 candidates in the different detector regions. This has shown to improve the performance. In the future there will be separate BDTs for the detector regions. As most analysis use only tau leptons with $p_t > 20\,\text{GeV}$ only those are considered for the test for the algorithm and thus for the optimization of the BDT cut. The optimized setups for the different FOMs and samples are summarized in table 4.8. The optimal cut values are very similar for the three FOMs.

FOM	7 TeV sample with pile up	8 TeV sample with pile up
N_{correct}	-0.02,-0.02,-0.03,-0.01,-0.02	-0.02,-0.03,-0.01,-0.03,-0.03
$\sum \lvert N_{\text{reco } \pi^0} - N_{\text{true } \pi^0} \rvert$	-0.02,-0.02,-0.02,-0.01,-0.04	-0.02,-0.03,-0.02,-0.04,-0.03
ϵ_1^1	-0.01,-0.01,-0.02, 0.00,-0.01	0.00,-0.02,-0.01, 0.00,-0.02

Table 4.8: Cut values on BDT output variable after the optimization for the different figure of merits. The cut values are each given in the following order: central barrel ($|\eta| < 0.8$), extended barrel ($0.8 < |\eta| < 1.3$), transition region ($1.3 < \eta < 1.6$), outer end-cap ($1.6 > |\eta| > 2.0$) and inner end-cap ($|\eta| > 2.0$). A larger value corresponds to a tighter cut (see figure 4.23).

Chapter 5

Performance of the neutral pion reconstruction in Monte Carlo simulation

In this section the performance of the neutral pion reconstruction in Monte Carlo simulated events is presented. The $Z \rightarrow \tau\tau$ samples including pile up are used (cf. section 4.1.2). The 7 TeV sample is the primary sample for the test, because the reconstruction is done with a similar version of the reconstruction software as for the sample of charged pions used to optimize the algorithm. The results for the 8 TeV sample are presented to give an impression of the performance of the algorithm in a scenario with higher pile up. The first 50 000 taus in the 7 TeV sample and the first 200 000 taus in the 8 TeV sample are excluded, as they have already been used for BDT cut optimization. As most analysis only use taus with $p_t > 20$ GeV, the same selection is applied in the following. After the selection the numbers of remaining taus in the test samples are $\sim$ 62 000 from the 7 TeV sample and $\sim$ 306 000 from the 8 TeV sample. In the following each cluster that passes the BDT cuts is considered as a reconstructed neutral pion. Its 4-momentum is reconstructed as the 4-momentum of the cluster after assigning the neutral pion mass.

In the first section the counting performance of the algorithm is presented. In the following section the reconstruction of the neutral pion 4-momentum is discussed. The final section focuses on the reconstruction of the intermediate ρ and a_1 resonances.

5.1 Neutral pion counting

The neutral pion counting performance is tested with the figures of merit described in the previous section. Tables 5.1 and 5.2 show the results obtained on the test samples after optimization of the BDT cuts for the different FOMs. The accuracy of the results obtained for the 7 TeV sample suffers from the limited statistics both in the sample used to find the BDT cut values and the test sample itself. No significant differences for the differently optimized cuts can be observed, there only is a very slight trend that after optimizing for ϵ_1^1 the performance for the other FOMs is degraded. The statistical errors are much smaller for the 8 TeV sample. It can be seen that optimizing for N_{correct} or $\sum |N_{\text{reco }\pi^0} - N_{\text{true }\pi^0}|$ gives very similar results (both in tables 4.8 and 5.2). The figure of merit ϵ_1^1 prefers slightly tighter cuts, which marginally degrades the results for the other figures of merit. The pile up dependence of the counting performance can be quantified by comparing tables 5.1 and 5.2. The performance is not significantly different for the 7 TeV sample with lower pile up and the 8 TeV sample. As optimizing for the different figures of merit gives very similar results, all following results are obtained using the same optimization. The optimization for the figure of merit N_{correct}, which takes all decay modes into account, is chosen.

To obtain further information on the counting performance, so called 'efficiency matrices' are studied. They contain the efficiencies $\epsilon_{N_{\text{true }\pi^0}}^{N_{\text{reco }\pi^0}}$ defined in the previous section, i.e. the probabilities to reconstruct

FOM for optimization	$N_{\text{correct}}/N_{\text{total}}$ [%]	$\sum \lvert N_{\text{reco }\pi^0} - N_{\text{true }\pi^0}\rvert/N_{\text{total}}$ [%]	ϵ_1^1 [%]
N_{correct}	62.45 ± 0.40	41.62 ± 0.31	68.19 ± 0.59
$\sum \lvert N_{\text{reco }\pi^0} - N_{\text{true }\pi^0}\rvert$	62.45 ± 0.40	41.58 ± 0.31	68.16 ± 0.59
ϵ_1^1	62.32 ± 0.40	41.87 ± 0.31	68.22 ± 0.59

Table 5.1: Figures of merit for the counting performance in the 7 TeV sample the optimization for the different FOMs. The statistical errors are given. The same events are used.

FOM for optimization	$N_{\text{correct}}/N_{\text{total}}$ [%]	$\sum \lvert N_{\text{reco }\pi^0} - N_{\text{true }\pi^0}\rvert/N_{\text{total}}$ [%]	ϵ_1^1 [%]
N_{correct}	62.15 ± 0.14	42.08 ± 0.12	68.60 ± 0.27
$\sum \lvert N_{\text{reco }\pi^0} - N_{\text{true }\pi^0}\rvert$	62.16 ± 0.14	42.05 ± 0.12	68.52 ± 0.27
ϵ_1^1	61.99 ± 0.14	42.47 ± 0.12	68.79 ± 0.27

Table 5.2: Figures of merit for the counting performance in the 8 TeV sample after setup for the different figures of merit. The statistical errors are given. The same events are used.

$N_{\text{reco }\pi^0}$ π^0 candidates in decays with $N_{\text{true }\pi^0}$ neutral pions. The efficiency matrices obtained for the two samples can be found in tables 5.3 and 5.4. Of special interest are the diagonal entries of the matrices, which are the efficiencies to count the neutral pions correctly. The diagonal entries decrease with the number of neutral pions to count. One reason for this is that the algorithm counts two neutral pions if the two photons from a neutral pion decay create separate clusters, and that it counts only one π^0 if two neutral pions are merged. Secondly in decays with more particles in the final state the energy of each decay product is smaller. This increases the probability that π^0s are rejected by the preselection cut or are outside the $\Delta R = 0.2$ cone of the tau, in which neutral pions are reconstructed. Low energy neutral pions are also more likely to be accidentally removed with the charged hadron subshower.

As the algorithm is not yet fully optimized for the end-cap and transition regions (compare section 4.2.5) the dependence of the counting performance on the detector region is of interest. Since large event samples are required the 8 TeV sample is used. The FOMs obtained in the whole detector and the separate regions can be found in table 5.5. Tables 5.6 to 5.8 show the efficiency matrices for the whole electromagnetic calorimeter and the separate detector regions, the combined matrix for the whole electromagnetic calorimeter can be found in table 5.4. In terms of N_{correct} the performance in the barrel and end-cap regions agrees within errors, it is however reached in a different way. In the barrel region more decays with neutral pions are correctly reconstructed while in the end-cap ϵ_0^0 is larger because on average less neutral pions are reconstructed. Therefore it is also more likely that neutral pions in the end-cap are missed, which causes $\sum \lvert N_{\text{reco }\pi^0} - N_{\text{true }\pi^0}\rvert$ and ϵ_1^1 to be slightly worse than in the barrel. This difference is probably caused by correlations of some of the BDT input variables to the detector region (compare section 4.3.3) and can be reduced by using separate BDTs for the different detector region.

	$N_{\text{reco }\pi^0} = 0$	$N_{\text{reco }\pi^0} = 1$	$N_{\text{reco }\pi^0} = 2$	$N_{\text{reco }\pi^0} > 2$
$N_{\text{true }\pi^0} = 0$	81.3	16.3	2.2	0.3
$N_{\text{true }\pi^0} = 1$	16.6	68.2	13.8	1.4
$N_{\text{true }\pi^0} = 2$	6.5	52.3	35.2	6.1
$N_{\text{true }\pi^0} > 2$	3.3	40.0	43.2	13.5

Table 5.3: Efficiency matrix for the 7 TeV sample. The efficiencies are given in percent. The statistical errors are $\lesssim 0.6\,\%$.

	$N_{\text{reco }\pi^0} = 0$	$N_{\text{reco }\pi^0} = 1$	$N_{\text{reco }\pi^0} = 2$	$N_{\text{reco }\pi^0} > 2$
$N_{\text{true }\pi^0} = 0$	79.9	17.1	2.6	0.4
$N_{\text{true }\pi^0} = 1$	16.5	68.6	13.5	1.4
$N_{\text{true }\pi^0} = 2$	5.7	51.1	36.8	6.4
$N_{\text{true }\pi^0} > 2$	3.4	40.3	42.7	13.6

Table 5.4: Efficiency matrix for the 8 TeV sample. The efficiencies are given in percent. The statistical errors are $\lesssim 0.3$ %.

Detector region	$N_{\text{correct}}/N_{\text{total}}$ [%]	$\sum \lvert N_{\text{reco }\pi^0} - N_{\text{true }\pi^0}\rvert / N_{\text{total}}$ [%]	ϵ_1^1 [%]
all Ecal	62.15 ± 0.14	42.08 ± 0.12	68.60 ± 0.27
barrel	62.68 ± 0.19	41.21 ± 0.16	70.04 ± 0.36
transition region	56.58 ± 0.50	48.87 ± 0.45	61.10 ± 0.73
end-cap	62.98 ± 0.24	41.71 ± 0.25	68.81 ± 0.49

Table 5.5: Comparison of the counting performance in the whole electromagnetic calorimeter and in the separate detector regions. The cuts on the BDT output variable have been optimized for N_{correct}.

As expected the performance is worse in the transition regions. However, considering that the shower subtraction in this region is very preliminary, the performance obtained already now is promising.

5.2 Reconstruction of the neutral pion kinematics

The performance of the neutral pion 4-momentum reconstruction is tested on taus that have one true and one reconstructed neutral pion. This makes the matching of ${\pi^0}_{\text{true}}$ and ${\pi^0}_{\text{reco}}$ and therefore the interpretation of the results much easier. Figure 5.1 shows the energy reconstruction performance of the algorithm. The RMS of the distribution is about 30 % for both samples. The reconstructed energy is slightly biased towards higher values. The bias is significantly larger for low energy neutral pions as can be seen in figure 5.2. This is an indication that the bias might be either caused by the local hadron calibration, which scales up the energy of low energetic cells, or by pile up. The position reconstruction performance can be seen in figure 5.3. The RMS of the distribution is in the order of $\Delta R = 0.02$, which is comparable to the width of one cell in Ecal2 ($\Delta\eta \times \Delta\phi = 0.025 \times 0.025$). The position reconstruction improves with energy (figure 5.4). As particles in with high pseudorapidities are in general more highly boosted, the position reconstruction is better in this kinematic region.

	$N_{\text{reco }\pi^0} = 0$	$N_{\text{reco }\pi^0} = 1$	$N_{\text{reco }\pi^0} = 2$	$N_{\text{reco }\pi^0} > 2$
$N_{\text{true }\pi^0} = 0$	79.35	17.91	2.46	0.28
$N_{\text{true }\pi^0} = 1$	14.96	70.04	13.72	1.27
$N_{\text{true }\pi^0} = 2$	4.72	51.64	37.57	6.06
$N_{\text{true }\pi^0} > 2$	2.60	39.94	43.94	13.52

Table 5.6: Counting efficiency matrix for the 8 TeV sample in the barrel region. The efficiencies are given in percent. The statistical errors are $\lesssim 0.4$ %.

	$N_{\text{reco }\pi^0} = 0$	$N_{\text{reco }\pi^0} = 1$	$N_{\text{reco }\pi^0} = 2$	$N_{\text{reco }\pi^0} > 2$
$N_{\text{true }\pi^0} = 0$	74.69	20.63	3.96	0.72
$N_{\text{true }\pi^0} = 1$	18.63	61.10	18.06	2.21
$N_{\text{true }\pi^0} = 2$	7.15	50.04	34.97	7.84
$N_{\text{true }\pi^0} > 2$	4.44	40.39	44.17	11.00

Table 5.7: Counting efficiency matrix for the 8 TeV sample in the transition region. The efficiencies are given in percent. The statistical errors are $\lesssim 0.7\,\%$.

	$N_{\text{reco }\pi^0} = 0$	$N_{\text{reco }\pi^0} = 1$	$N_{\text{reco }\pi^0} = 2$	$N_{\text{reco }\pi^0} > 2$
$N_{\text{true }\pi^0} = 0$	84.61	12.97	2.03	0.39
$N_{\text{true }\pi^0} = 1$	20.43	68.81	9.77	9.88
$N_{\text{true }\pi^0} = 2$	8.37	53.82	33.14	4.66
$N_{\text{true }\pi^0} > 2$	5.69	45.47	38.85	9.99

Table 5.8: Counting efficiency matrix for the 8 TeV sample in the end-cap region. The efficiencies are given in percent. The statistical errors are $\lesssim 0.5\,\%$.

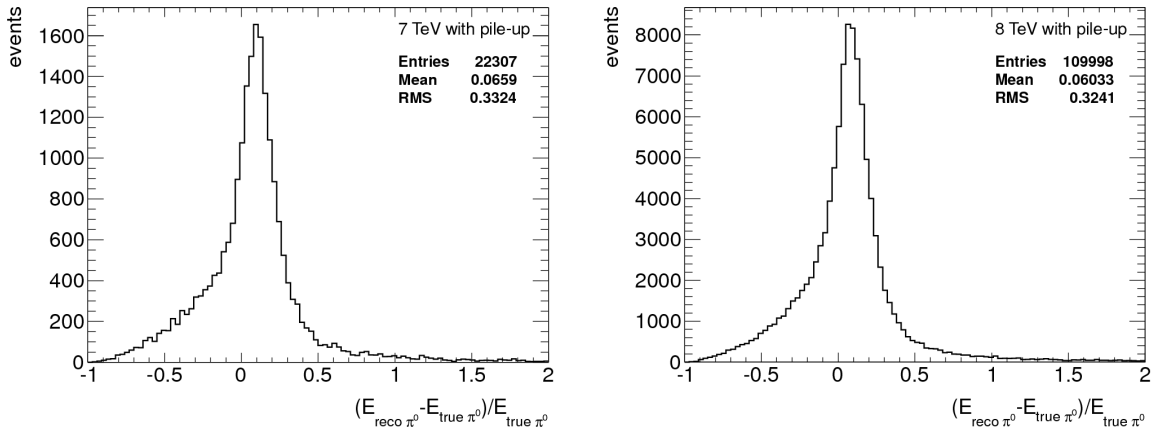

Figure 5.1: Energy reconstruction performance for the 7 TeV and 8 TeV samples. The energy is slightly biased towards higher values. The distributions are slightly asymmetric.

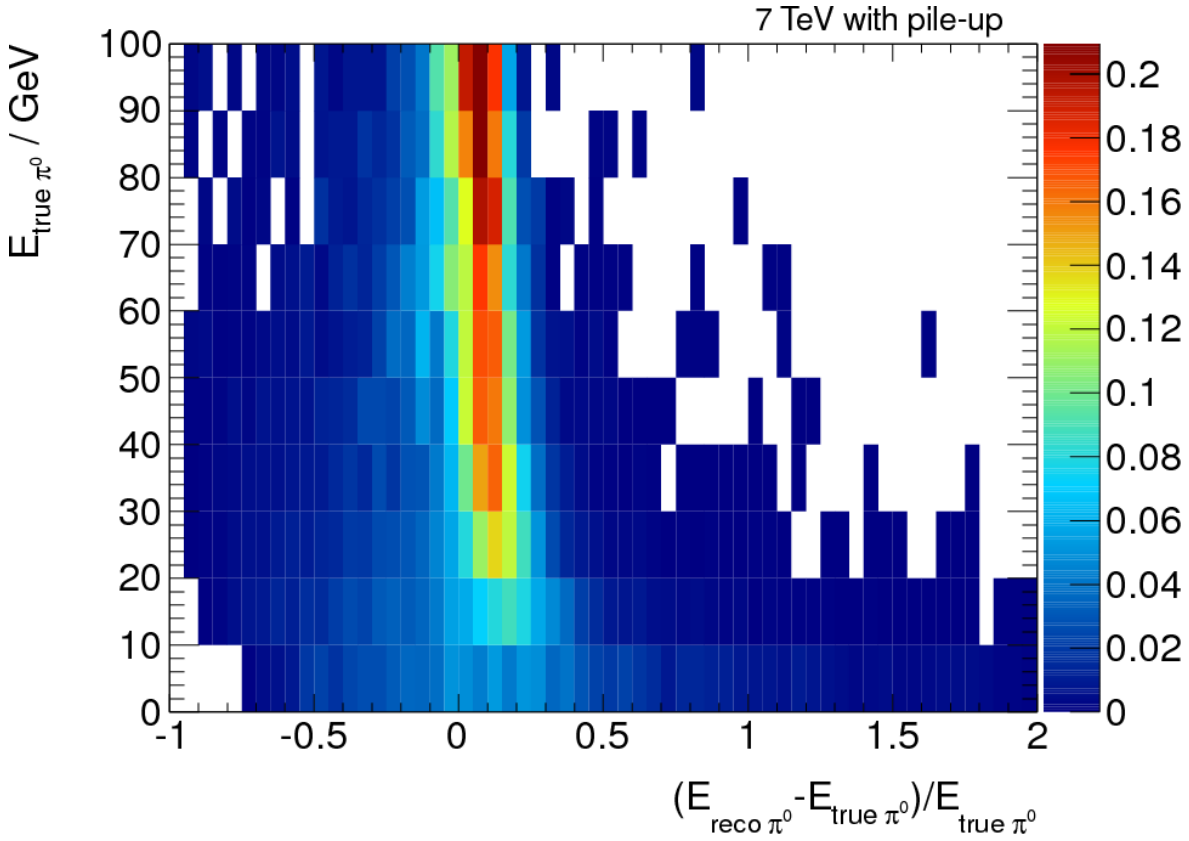

Figure 5.2: Dependence of the average energy resolution on the true neutral pion energy. The distribution in each bin of $E_{\text{true }\pi^0}$ is normalized to one. The bias of the energy reconstruction is higher for lower energies.

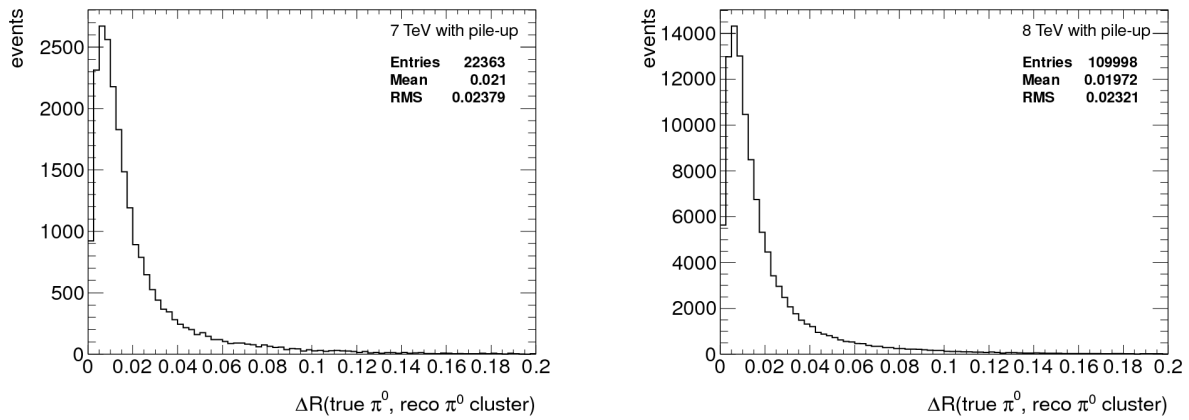

Figure 5.3: Position resolution of reconstructed neutral pions for the 7 TeV and 8 TeV samples.

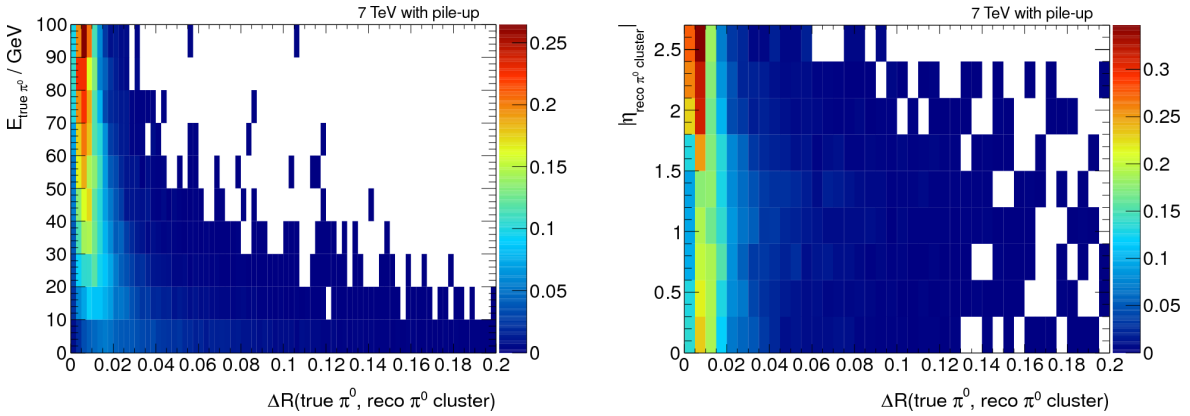

Figure 5.4: Dependence of the position reconstruction performance on the neutral pion energy and the pseudorapidity. The reconstruction of the position is better for higher energies and pseudorapidities.

Particle	mass / MeV	width / MeV
$\pi^{\pm}$	139.57018 ± 0.00035	(negligible)
$K^{\pm}$	493.677 ± 0.016	(negligible)
$\rho^{\pm}$	775.49 ± 0.34	149.1 ± 0.8
$a_1^{\pm}$	1230 ± 40	250 – 600 (generated: 160)

Table 5.9: Masses of dominant decay products in hadronic 1-prong tau decays [6].

5.3 Reconstruction of intermediate resonances

The reconstruction of the invariant mass of the visible tau decay products ('visible mass') is another test of the neutral pion reconstruction performance and could also be used for tau identification or polarization studies. The branching fractions of the dominant tau decay modes can be found in table 1.1 of section 1.2.1. The best known current values of the masses and widths of the most frequently produced particles in tau decays can be found in table 5.9. In the following the reconstructed visible mass of a tau is defined as

$$\text{reco } m_{\text{vis}\tau} = \sqrt{\left(p_{\text{track}}^{m_{\pi^\pm}} + \sum_{\text{reco } \pi^0} p_{\text{cluster}}^{m_{\pi^0}} \right)^2}, \tag{5.1}$$

where $p_{\text{track}}^{m_{\pi^\pm}}$ is the 4-momentum of the track after assigning the charged pion mass and $p_{\text{cluster}}^{m_{\pi^0}}$ is the 4-momentum of a reconstructed neutral pion. Taus with n reconstructed neutral pions are denoted as '$n\pi^0{}_{\text{reco}}$ taus' and taus with n generated neutral pions are denoted as '$n\pi^0{}_{\text{true}}$ taus'.

Figure 5.5 shows the spectrum of the generated visible mass for hadronic 1-prong decays and the spectrum of the reconstructed visible mass for the 7 TeV sample. In the true visible mass spectrum the peaks at the pion mass, the kaon mass, the ρ mass and the a_1 mass are clearly visible. In the reconstructed spectrum the peaks at the pion and rho masses are also clearly visible. A peak at the a_1 mass can be seen for $2\pi^0{}_{\text{reco}}$ taus. The peak at the kaon mass is missing in the reconstructed visible mass spectrum, because all tracks are assigned the pion mass. In approximately 95 % of the cases the reconstructed visible mass is below the tau mass. In figure 5.6 the spectra of the reconstructed visible mass for $1\pi^0{}_{\text{reco}}$ taus and $2\pi^0{}_{\text{reco}}$ taus is shown. Most $1\pi^0{}_{\text{reco}}$ taus are also $1\pi^0{}_{\text{true}}$ taus. This is however partly caused by

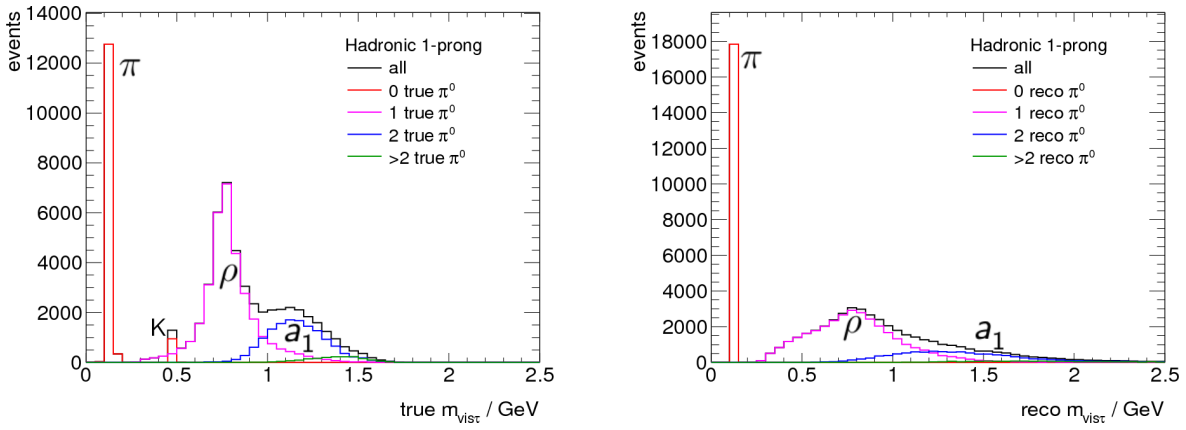

Figure 5.5: Generated (left) and reconstructed (right) visible mass spectra of hadronic 1-prong tau decays in the 7 TeV sample. In the true visible mass spectrum peaks at the pion mass, the kaon mass, the ρ mass and the a_1 mass are clearly visible. In the reconstructed visible mass spectrum there are peaks at the pion and rho mass, also an excess of events with two reconstructed neutral pions can be seen.

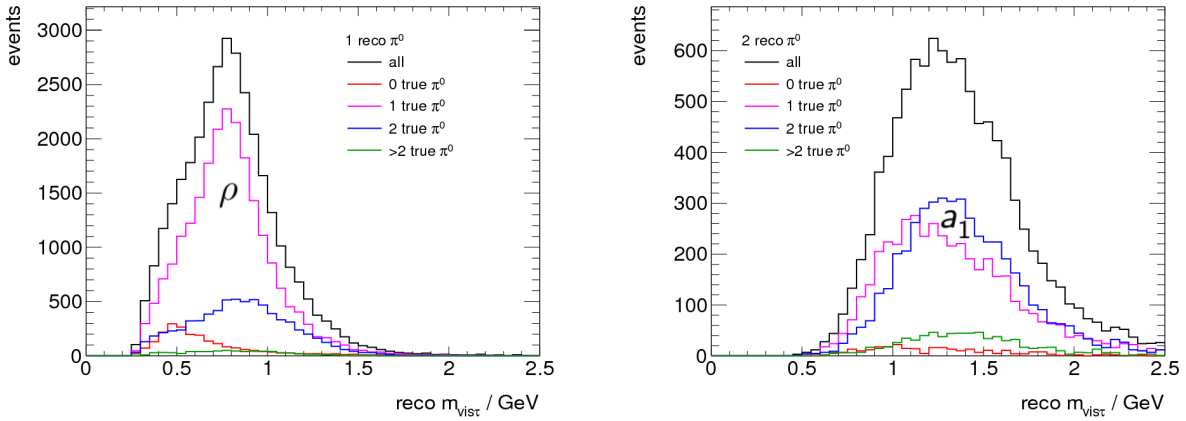

Figure 5.6: Reconstructed visible mass spectra of taus from the 7 TeV sample that are reconstructed with one (left) or two (right) neutral pions. The spectrum is split into the contributions of taus with different numbers of true neutral pions.

the branching fractions, which for 1-prong decays with one neutral pion is approximately 2.5 times as large as for decays without π^0s or with more than one neutral pion. For $0\pi^0_{\text{true}}$ taus that are reconstructed with one π^0, the reconstructed visible mass is slightly lower than for those that have been generated with one π^0. This is because most background candidates have low energy. Conversely the invariant mass is usually slightly larger for $2\pi^0_{\text{true}}$ taus that are reconstructed with one neutral pion. Probably this is due to candidates, for which the two neutral pions are merged in one cluster, which then has higher energy. Among the $2\pi^0_{\text{reco}}$ taus, those that have been generated with one or two π^0s are almost as frequent. This again is caused by the higher branching fraction of decays with one neutral pion. The reconstructed visible mass is slightly lower for $1\pi^0_{\text{true}}$ that have been reconstructed as a $2\pi^0_{\text{reco}}$ tau. Decays without true neutral pions are very rarely reconstructed with two π^0s, while decays with more than two π^0s have a very low branching fraction of approximately 1 %.

The mean and the width of the reconstructed ρ resonance peaks in the visible mass spectra of all $1\pi^0_{\text{reco}}$ taus and those that have also been generated with one neutral pion is obtained with a Gaussian fit (figure 5.7). The mean of the mass peaks is very close to the true rho mass. The reconstructed

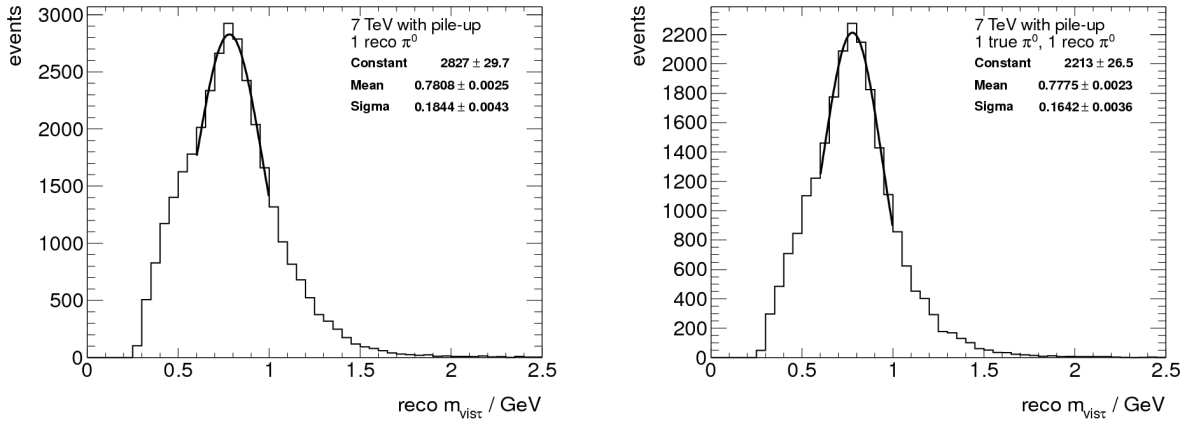

Figure 5.7: Gaussian fit to the reconstructed ρ resonance (7 TeV sample). The fit is performed for the peak in the reconstructed visible mass spectrum of all taus that are reconstructed with one neutral pion (left) and those that are generated with one neutral pion (right).

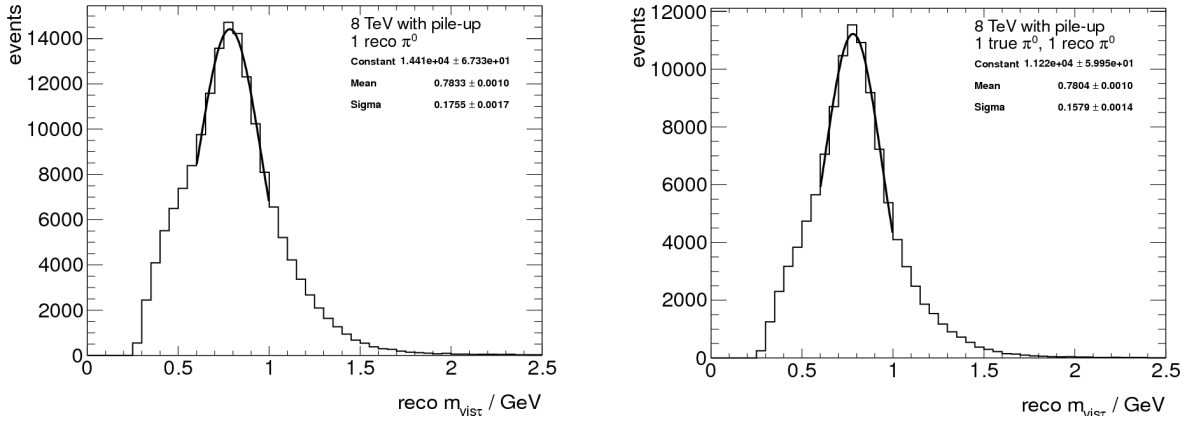

Figure 5.8: Gaussian fit to the reconstructed ρ resonance (8 TeV sample). The fit is performed for the peak in the reconstructed visible mass spectrum of all taus that are reconstructed with one neutral pion (left) and those that are generated with one neutral pion (right).

width is 5 – 10 % larger than the natural width of the ρ. It is significantly lower in the right plot in figure 5.7, because the $0\pi^0{}_{\text{true}}$ taus and $2\pi^0{}_{\text{true}}$ taus, which are reconstructed with one neutral pion, are reconstructed with slightly lower or higher visible masses (see above). The reconstruction of the rho mass peak also works for higher pile up (figure 5.8). The mean and the width of the distributions obtained in the 7 TeV and 8 TeV samples agree within errors. The reconstructed a_1 mass is slightly larger than the true mass (figures 5.9 and 5.10), possibly because the energy of low energy neutral pions is overestimated (compare figure 5.2), since π^0s that are produced in $2\pi^0{}_{\text{true}}$ decays have lower energies than those produced in $2\pi^0{}_{\text{true}}$ decays. The width of the reconstructed a_1 mass peak is approximately twice the generated width. The values obtained for the 7 TeV and 8 TeV samples agree within errors.

In conclusion the π^0 reconstruction allows for a reasonably good reconstruction of the intermediate resonances.

Finally I am briefly commenting on the comparison of the performance of the algorithm developed in this thesis ('new') with the previous version of the algorithm and the algorithm currently default in ATLAS (cf. section 3.2.1). The results for the other algorithms have been obtained with $Z \rightarrow \tau\tau$ samples without pile up and with candidates contained in the barrel region [17]. A comparison of the diagonal

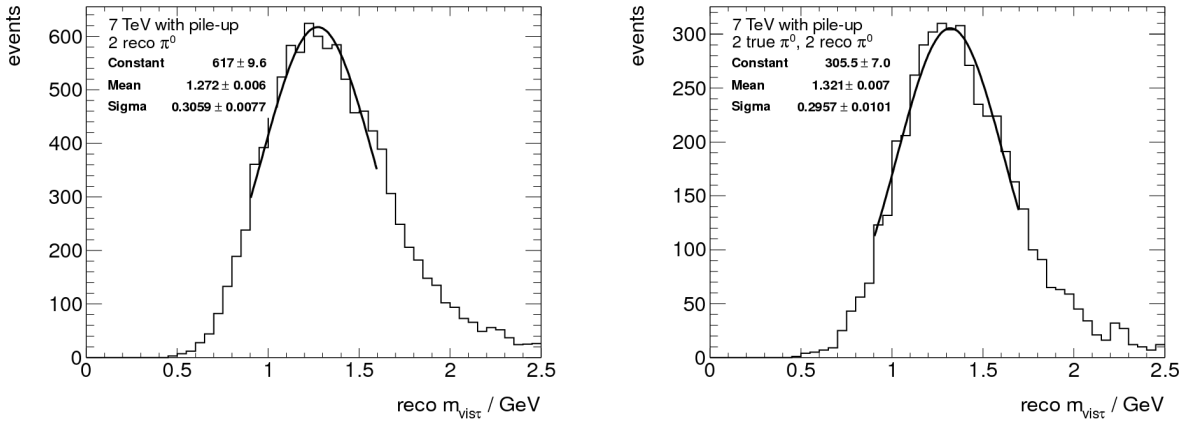

Figure 5.9: Gaussian fit to the reconstructed a_1 resonance (7 TeV sample). The fit is performed for the peak in the reconstructed visible mass spectrum of all taus that are reconstructed with two neutral pions (left) and those that are generated with two neutral pions (right).

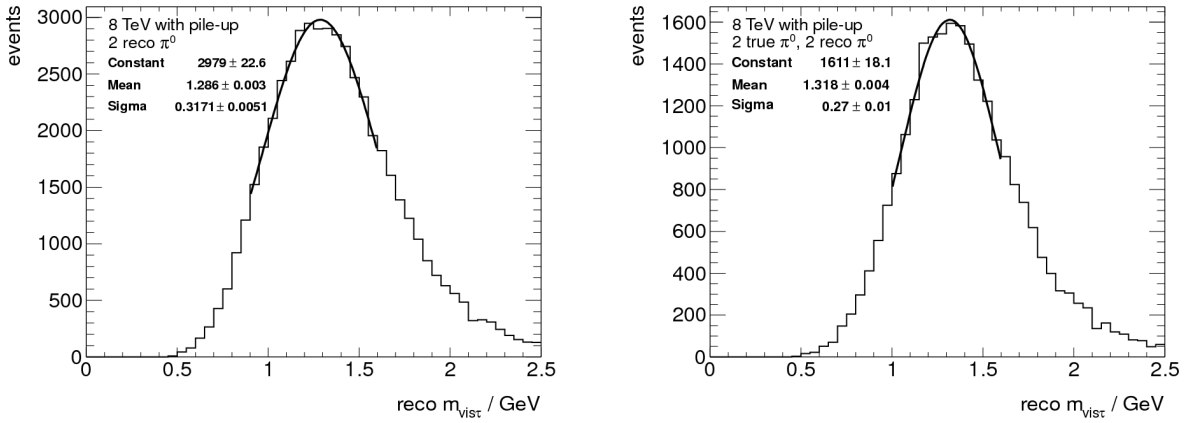

Figure 5.10: Gaussian fit to the reconstructed a_1 resonance (8 TeV sample). The fit is performed for the peak in the reconstructed visible mass spectrum of all taus that are reconstructed with two neutral pions (left) and those that are generated with two neutral pions (right).

	new algorithm	previous version	default
ϵ_0^0	81.3	77.7	66.4
ϵ_1^1	68.2	58.2	50.9
$\epsilon_2^{>1}$	41.3	41.5	52.8

Table 5.10: Comparison of diagonal elements in the counting efficiency matrix for the current default algorithm, the algorithm developed in this thesis (new) and the previous version of the algorithm developed in this thesis. For the new algorithm the results obtained in the 7 TeV sample with pile up and the whole electromagnetic calorimeter are given. The results for the other algorithms have been obtained with $Z \rightarrow \tau\tau$ samples without pile up and with candidates contained in the barrel region [17].

elements of the efficiency matrix of the three algorithms is shown in table 5.10. The efficiencies ϵ_0^0 and ϵ_1^1 obtained with the new algorithm are significantly larger than for the other algorithms. The efficiency[1] $\epsilon_2^{>1}$ is comparable for the new algorithm and the previous version and is significantly larger for the current default algorithm, which on average counts significantly more neutral pions. The reconstructed width of the invariant mass distributions is by about 10 % larger for the new algorithm than for the previous version. The reconstructed means of the distributions are now comparable with the true masses, while they were biased by about 10 % for the ρ and by about 20 % for the a_1 resonances.

[1] In [17] decays with zero, one and more than one neutral pions are being distinguished.

Chapter 6

Outlook

6.1 Plans for a comparison of the currently developed algorithms in Monte Carlo simulated samples and collision data

A comparison of the three currently actively developed algorithms in ATLAS (cf. section 3.2.1) is planned for the near future. Within this comparison the neutral pion counting performance, the reconstruction of the the neutral pion 4-momentum, the reconstruction of the combined 4-momentum of the visible decay products of the tau and the reconstruction of resonances will be studied in Monte Carlo simulated $Z \rightarrow \tau\tau$ samples. The dependence of the reconstruction performance on kinematic variables and pile up will be investigated in detail. The comparison will also include a test of the algorithms in collision data. For this, $Z \rightarrow \tau\tau$ decays, in which one of the taus decays into a muon and the other hadronically, will be selected using the so-called tag-and-probe method [16]. In addition the agreement between simulation and data of the energy remaining after the hadronic subshower subtraction will be studied in detail as well as the input variables of the BDT used to suppress misidentified candidates.

6.2 Ideas for further improvements of the algorithm

There are several ideas for possible improvements of the algorithm. In this respect a strong cooperation with the developers of PanTau [15] is planned, as there are many ideas from which both algorithms are expected to benefit. In the following section ideas to improve the hadronic shower subtraction are presented. The subsequent section focuses on improvements of the neutral pion identification.

6.2.1 Ideas to improve the hadronic subshower subtraction

The most important issues regarding the shower subtraction and concepts for improvements are summarized in the following.

- The shower subtraction is not currently implemented for multi-prong candidates. To make the algorithm available for these the energy deposited by each charged hadron in the hadronic calorimeter must be determined separately. Because it is expected that the subshowers are merged, a separation on cluster level will probably be insufficient. A possible solution has been developed at the HERA experiment [17, 21] and will be investigated for the use in ATLAS.

- As discussed in section 4.2.5 the extension of the subtraction method to the end-cap and transition regions is preliminary. An additional η bin is required for the region covered by the end-cap presampler. The amount of statistics of simulated single charged hadrons has not significantly increased, therefore the binning in other variables must probably be reduced to obtain reliable lateral shower shapes for the end-cap presampler. Hadronic shower shapes in the transition region

must be studied, especially the energy fractions in the layers of the barrel and end-cap calorimeters as a function of $|\eta|$ (longitudinal weights).

- The shower shapes for the central barrel region can be obtained using the Combined Test Beam Data, as soon as this is made available in the current reconstruction software release. The statistics of low energy charged hadrons $p_t \lesssim 20\,\text{GeV}$ in data might be sufficient to obtain the shower shapes for this kinematic region.
- One of the main difficulties of the hadronic subshower removal is the fluctuation of the energy deposited in the different layers (compare figure 4.6). The binning in the hadronic fraction reduces this problem. Due to the thickness of the Ecal2 layer, however, the hadronic fraction is hardly different for showers that start in the strip layer or at the beginning of Ecal2. A potentially much better solution would be to look for 'hits' in Ecal1. Due to the fine granularity within this layer it is very likely that the energy deposits of charged and neutral pions can be separated.
- Alternative parameterization functions for the lateral hadronic shower shapes can be investigated to improve the accuracy of the hadronic subshower removal.
- For very high energetic tracks with $p_t \gtrsim 150\,\text{GeV}$ the precision of the hadronic subshower subtraction is limited by the resolution of the track momentum. The estimation of the total energy in the electromagnetic calorimeter uses the track momentum and needs thus to be reconsidered for these candidates.
- Systematic uncertainties of the hadronic subshower subtraction need to be evaluated. The dominating contributions are expected to be caused by the shower model (as long as simulated hadrons are used to obtain the shapes) and the parametrization. To study the first contribution, samples for which the showers have been simulated with a different model can be used. The contribution of the parameterization can be estimated by varying the fit parameters within errors and using an alternative function for the parameterization.

6.2.2 Ideas to improve the identification of neutral pion clusters

In the following, ideas for improvements of the identification of neutral pion clusters are summarized.

- The current algorithm cannot identify cases, in which the two photons from a neutral pion create separate clusters or in which the showers of two neutral pions merge. They can possibly be identified by counting 'hits' in the strip layer or by the width of a shower in the calorimeter.
- Calibration hits, i.e. information on the contribution of a particle to an energy deposit in the electromagnetic calorimeter in special simulated samples, could be used to improve the classification into signal and background clusters for the BDT training.
- The calibration of the energy deposits remaining after the hadronic subshower subtraction can be changed from a local hadron calibration to a calibration for electromagnetic showers. This possibly reduces or even removes the bias of the reconstructed neutral pion energy towards higher values for low energy neutral pions (cf. 5.4).
- Tracks from converted photons into electrons could be considered for the identification of signal clusters

My plan is to continue working on the improvements for the shower subtraction and the neutral pion candidate selection after completion of this thesis.

Chapter 7

Conclusions

Tau leptons are important signatures at the LHC for the search for new physics, e.g. Supersymmetry, the study of the Higgs boson in the Standard Model as well as in models with an extended Higgs sector predicting several Higgs bosons, and Standard Model measurements studying W or Z bosons. Tau reconstruction and identification are thus of large interest in ATLAS and the necessary algorithms have been developed and further improved in the past few years. The reconstruction of the neutral pion substructure of a hadronically decaying tau is an active field of study. It can be used to distinguish between different tau decay modes, which is useful both for physics analysis, e.g. analysis that make use of the tau polarization, and to improve the performance of the tau identification algorithms.

This thesis proposes an algorithm that reconstructs neutral pions in hadronic 1-prong tau decays. It is currently being implemented in the official tau reconstruction software in ATLAS. In the first part of the algorithm the energy deposited in the electromagnetic calorimeter by the charged pion is subtracted cell by cell. The subtraction of the hadronic energy from the electromagnetic calorimeter proceeds as follows: The total energy deposited by the charged pion in the electromagnetic calorimeter is calculated from the track momentum and the energy deposited in the hadronic calorimeter. Thereafter the energy deposited by the charged pion within the layers of the electromagnetic calorimeter and then within each cell of a layer is calculated. This energy is subtracted cell by cell. After the subtraction the remaining energy depositions in the electromagnetic calorimeter are re-clustered. In more than 50 % of all decays without neutral pions no neutral pion candidate is found, while there are candidates left for more than 90 % of all taus with neutral pions. In the second part of the algorithm the selection of neutral pion candidates is done by using Boosted Decision Trees which are trained to identify neutral pion clusters by their shape in the calorimeter. The algorithm has been tested with two samples of Monte Carlo simulated $Z \rightarrow \tau\tau$ decays from 2011 and 2012 to study the pile up dependence of the performance. The results obtained with both samples agree within the percent level. The number of neutral pions can be counted correctly in approximately 80 % of $\tau^{\pm} \rightarrow h^{\pm}\nu_{\tau}$ decays, $\sim$ 70 % of $\tau^{\pm} \rightarrow h^{\pm}\pi^0\nu_{\tau}$ decays and $\sim$ 35 % of $\tau^{\pm} \rightarrow h^{\pm}\pi^0\pi^0\nu_{\tau}$ decays. The reconstruction of the neutral pion energy and direction has been studied using $\tau^{\pm} \rightarrow h^{\pm}\pi^0\nu_{\tau}$ decays, where one neutral pion has been found by the algorithm. Furthermore it has been shown that the neutral pion reconstruction algorithm allows for a reconstruction of the intermediate ρ and a_1 resonances in tau decays. A comparison of the performance with the previous version of the algorithm developed in this thesis and the current default algorithm used in ATLAS is presented.

Two further algorithms that reconstruct neutral pions in hadronic tau decays are currently being actively developed in ATLAS. A detailed comparison of the performance of the algorithms will be done in the near future. This will include tests with collision data. A strong cooperation with the developers of the other algorithms, in particular the PanTau algorithm, is planned for example to identify cases in which the two photons from a neutral pion decay create one cluster each or cases in which neutral pion showers are merged.

Appendix A

Parameters of the calorimeter system

	Coverage in $\lvert\eta\rvert$	Granularity $\delta\eta \times \delta\phi$
electromagnetic calorimeter (barrel)		
Presampler (PS)	$\lvert\eta\rvert < 1.520$	0.025×0.100
1st layer (strip layer)	$\lvert\eta\rvert < 1.400$	$0.025/8 \times 0.100$
	$1.400 < \lvert\eta\rvert < 1.475$	0.025×0.025
2nd layer	$\lvert\eta\rvert < 1.400$	0.025×0.025
	$1.400 < \lvert\eta\rvert < 1.475$	0.075×0.025
3rd layer	$\lvert\eta\rvert < 1.350$	0.050×0.025
electromagnetic calorimeter (end-cap)		
Presampler (PS)	$1.500 < \lvert\eta\rvert < 1.800$	0.025×0.100
1st layer (strip layer)	$1.375 < \lvert\eta\rvert < 1.425$	0.050×0.100
	$1.425 < \lvert\eta\rvert < 1.500$	0.025×0.100
	$1.500 < \lvert\eta\rvert < 1.800$	$0.025/8 \times 0.100$
	$1.800 < \lvert\eta\rvert < 2.000$	$0.025/6 \times 0.100$
	$2.000 < \lvert\eta\rvert < 2.400$	$0.025/4 \times 0.100$
	$2.400 < \lvert\eta\rvert < 2.500$	0.025×0.100
2nd layer	$1.375 < \lvert\eta\rvert < 1.425$	0.050×0.025
	$1.425 < \lvert\eta\rvert < 2.500$	0.025×0.025
3rd layer	$1.500 < \lvert\eta\rvert < 2.500$	0.050×0.025
Hadronic tile calorimeter (barrel)		
layer 1	$\lvert\eta\rvert < 1.000$	0.100×0.100
layer 2	$\lvert\eta\rvert < 1.000$	0.100×0.100
layer 3	$\lvert\eta\rvert < 1.000$	0.200×0.100
Hadronic tile calorimeter (extended barrel)		
layer 1	$0.800 < \lvert\eta\rvert < 1.700$	0.100×0.100
layer 2	$0.800 < \lvert\eta\rvert < 1.700$	0.100×0.100
layer 3	$0.800 < \lvert\eta\rvert < 1.700$	0.200×0.100
LAr hadronic end-cap calorimeter		
All 4 layers	$1.500 < \lvert\eta\rvert < 2.500$	0.100×0.100

Table A.1: Main parameters of the ATLAS calorimeter system in the pseudorapidity range $\lvert\eta\rvert < 2.5$ [11]. The numbers valid only in the transition region of the electromagnetic calorimeter ('crack') are given in gray.

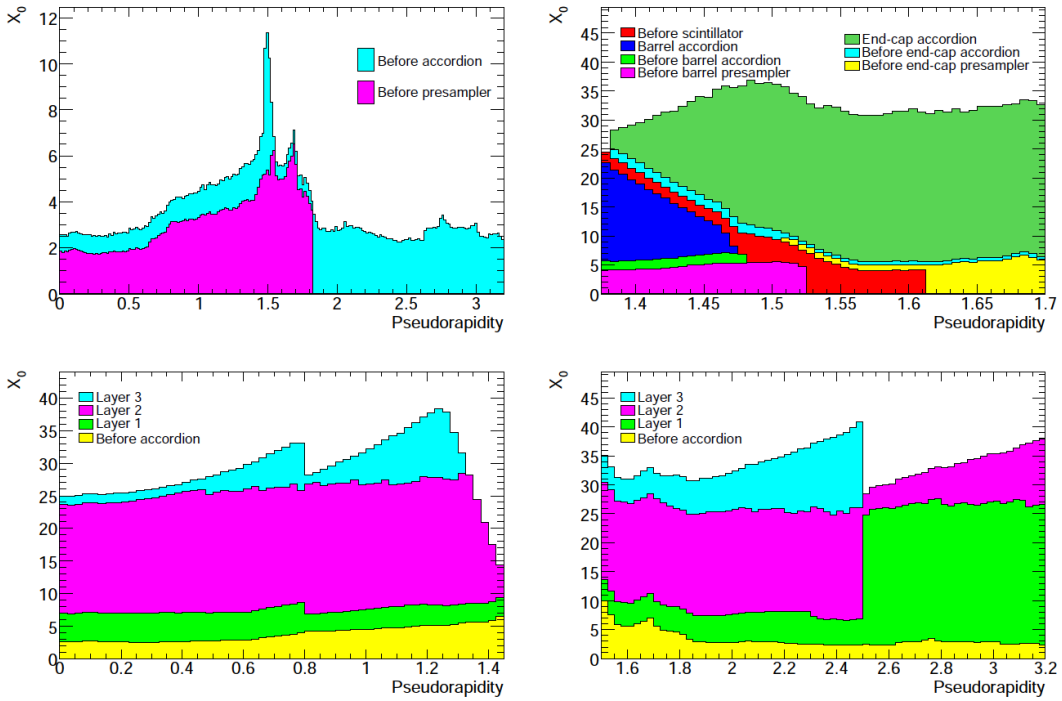

Figure A.1: Cumulative amount of material in and in front of the layers of the electromagnetic calorimeter as a function of $|\eta|$, in units of radiation lengths (X_0). The top left plot shows the amount of material before the presampler (up to $|\eta| = 1.8$) and before the electromagnetic calorimeter accordions. The top right plot shows the transition region from electromagnetic barrel to electromagnetic end-cap in more detail. The amount of material in the layers of the accordions are shown in the bottom left plot (barrel) and the bottom right plot (end-cap). In the bottom plots the change of the thickness of the lead plates at $|\eta| = 0.8$ and $|\eta| = 2.5$ can be recognized. For $|\eta| > 2.5$ there are only two layers. [11].

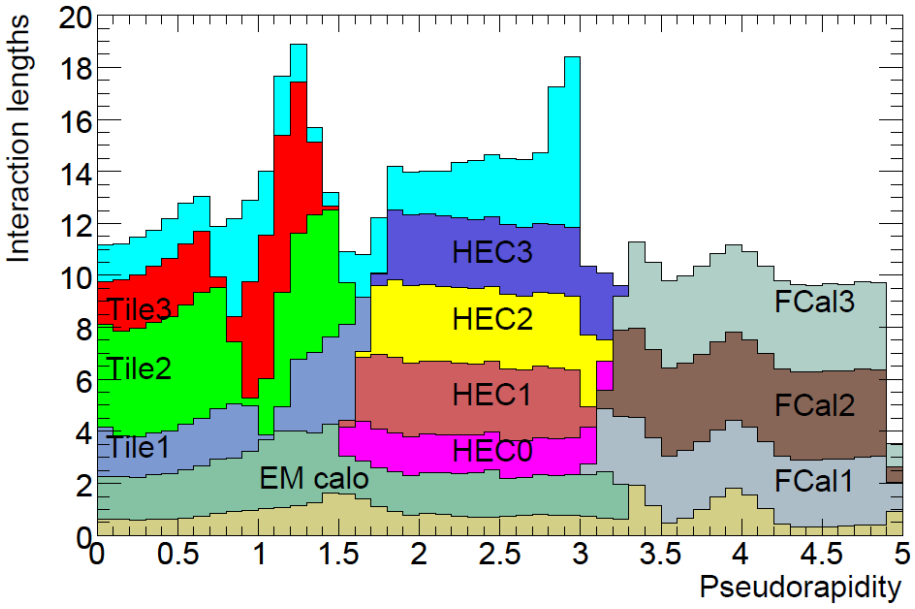

Figure A.2: Cumulative amount of material in and in front of the layers of the electromagnetic calorimeter, the tile hadronic calorimeter, the LAr hadronic calorimeter and the forward calorimeter as a function of $|\eta|$, in units of interaction lengths (λ). [11].

Bibliography

[1] The ATLAS Collaboration, 'Observation of a new particle in the search for the Standard Model Higgs boson with the ATLAS detector at the LHC', *Phys.Lett.* B716 (2012) 1–29, DOI: 10.1016/j.physletb.2012.08.020, arXiv:1207.7214 [hep-ex].

[2] CMS Collaboration, 'Observation of a new boson at a mass of 125 GeV with the CMS experiment at the LHC', *Phys.Lett.* B716 (2012) 30–61, DOI: 10.1016/j.physletb.2012.08.021, arXiv:1207.7235 [hep-ex].

[3] Wikipedia (Standard Model), wikipedia.org/wiki/Standard_Model.

[4] M. L. Perl et al., 'Evidence for Anomalous Lepton Production in e+e-Annihilation', *Physical Review Letters* 35 (1975) 1489.

[5] *The Nobel Prize in Physics 1995*, Aug. 2012, URL: Nobelprize.org.

[6] Particle Data Group, Beringer, J. et al., 'Review of Particle Physics', *Phys. Rev.* D86 (2012) 010001.

[7] A. Stahl, *Physics with Tau Leptons*, vol. 160, Springer Tracts in Modern Physics, Springer Berlin Heidelberg, 2000.

[8] L. Evans and L. Linssen, *The Super-LHC is on the starting blocks*, http://cerncourier.com/cws/article/cern/34932, July 2008, URL: http://cerncourier.com.

[9] CERN Press Release PR17.09, Nov 23, 2009, *Two circulating beams bring first collisions in the LHC*, URL: http://press.web.cern.ch/press/PressReleases/Releases2009/PR17.09E.html.

[10] L. R. Evans et al., 'LHC Machine', *JINST* 3 (2008) S08001.

[11] G. Aad et al., 'The ATLAS Experiment at the CERN Large Hadron Collider', *JINST* 3 (2008) S08003, DOI: 10.1088/1748-0221/3/08/S08003.

[12] C Roda and I Vivarelli, 'Cell Based Jet Calibration', tech. rep. ATL-PHYS-PUB-2005-019. ATL-COM-PHYS-2005-017. CERN-ATL-PHYS-PUB-2005-019, Geneva: CERN, 2005.

[13] W Braunschweig et al., 'Results from a test of a Pb-Fe liquid argon calorimeter', tech. rep. DESY-89-022, Hamburg: DESY, Feb. 1989.

[14] W. Lampl et al., 'Calorimeter clustering algorithms: Description and performance' (), ATL-LARG-PUB-2008-002.

[15] M Hodgkinson, D Tovey and R Duxfield, 'Energy Flow Reconstruction with the eflowRec Combined Reconstruction Software in Athena 15.6.9.8', tech. rep. ATL-PHYS-INT-2011-031, Geneva: CERN, 2011.

[16] ATLAS Collaboration, 'Performance of the Reconstruction and Identification of Hadronic Tau Decays with ATLAS', tech. rep. ATLAS-CONF-2011-152, Geneva: CERN, Nov. 2011.

[17] V. Scharf, 'Neutral Pion Subshower Reconstruction in Hadronic Tau Lepton Decays at the ATLAS experiment', Diploma thesis, University of Heidelberg, 2009.

[18] M. Aleksa et al., 'ATLAS Combined Testbeam: Computation and Validation of the Electronic Calibration Constants for the Electromagnetic Calorimeter',
tech. rep. ATL-LARG-PUB-2006-003. ATL-COM-LARG-2006-003, Geneva: CERN, 2006.

[19] S. Menke, *Cluster Moments*, URL: `https://twiki.cern.ch`.

[20] A. Hoecker et al., 'TMVA: Toolkit for Multivariate Data Analysis', *PoS* ACAT (2007) 040, arXiv:`physics/0703039`.

[21] C. Veelken, 'Search for Events with Isolated Leptons and Large Missing Transverse Momentum in ep Collisions at HERA', PhD thesis, University of Liverpool, Sept. 2005.

List of Figures

List of Tables

I hereby certify that the work presented here was accomplished by myself and without the use of illegitimate means or support, and that no sources and tools were used other than those cited.

Bonn, ...

Date Signature